Proceedings of the first MICCAI workshop on Image-Guidance and Multimodal Dose Planning in Radiation Therapy

Wolfgang Birkfellner, Jamie R. Mcclelland, Simon Rit, Alexander Schlaefer

Image-Guidance and Multimodal Dose Planning in Radiation Therapy

A workshop held at MICCAI 2012, Nice, France

Preface

Given its non-invasive nature, images and image computing form the basis for radiation therapy. Examples range from pre-treatment delineation of the target region to intra-treatment tracking of tissue motion and deformation. Hence, applications in radiation therapy have frequently been a driving force in the development of new image computing algorithms. The workshop 'Image-Guidance and Multimodal Dose Planning in Radiation Therapy' summarizes novel and state-of-the-art approaches reflecting different challenges in the radiation therapy workflow. First, a number of papers address specific issues in image segmentation when taking multiple modalities into account. Second, image registration is discussed, particularly in the context of organ motion. Third, the use of image data to guide the treatment, e.g., when selecting the position of beams or needles is considered. Finally, recent software toolkits are presented.

It is a privilege to hold this workshop in the context of MICCAI, and we appreciate that the organizers provide this exciting venue. We would like to thank all authors and reviewers for helping to compile a set of highly interesting papers and we also like to acknowledge the use of EasyChair (www.easychair.org) when preparing the proceedings.

August 16, 2012

Wolfgang Birkfellner
Jamie Mcclelland
Simon Rit
Alexander Schlaefer

Program Committee

Wolfgang Birkfellner	Center for Biomedical Engineering and Physics, Medical University Vienna, Austria
Jamie McClelland	Centre for Medical Image Computing, University College London, UK
Simon Rit	CREATIS, Université de Lyon and Centre Léon Bérard, France
Alexander Schlaefer	Medical Robotics, Institute for Robotics and Cognitive Systems, University of Lübeck, Germany

Additional Reviewers

C

Clarkson, Matt
D

Delmon, Vivien
Duerichen, Robert
H

Hadjar, Hamid
Hu, Yipeng
L

Létang, Jean Michel
M

Martin, James
R

Ricketts, Kate
Royle, Gary
S

Shahin, Osama
Stender, Birgit
V

Viulet, Tiberiu

Table of Contents

Investigating mediastinal lymph node stations segmentation on thoracic CT following experts guidelines

D. Sarrut[1,2], L. Claude[2], S. Rit[1,2], R. Pinho[1,2], G. Pitson[3], R. Lynch[3]

(1) Université de Lyon, CREATIS; CNRS UMR5220; Inserm U1044 ; France
(2) Department of Radiation Oncology, Centre Léon Bérard, Lyon, France
(3) Department of Radiation Oncology, Andrew Love Cancer Centre, Barwon Health, Geelong, Australia.

Abstract. In radiation therapy, accurate delineation of mediastinal lymph node stations on thoracic CT is essential for both prognostication and treatment delivery. We propose an original approach based purely on geometrical considerations, without using grey levels, that follow the reference guidelines and attempt to replicate the delineation undertaken manually by the experts. The proposed method is a greedy process based on fuzzy relative position constraints. It progressively refines an initial region towards the target by using a set of predefined anatomical structures. Experiments were conducted with two CT images that were manually segmented by experts. Average Dice Similarly Coefficient between segmented and references stations was close to 77%. This fast method (30 sec) could potentially assist the expert, for example in detecting situations where the guidelines are not strictly followed. To our knowledge, this is the first time such an approach has been proposed for this problem.

1 Introduction

Mediastinal and hilar lymph node involvement often occurs in lung cancer. A reference definition of lymph node station anatomy was recently updated by the IASLC Lung Cancer Staging Project. Such a definition is intended to be an internationally agreed framework that would allow precise and uniform determination of lymph node status by centres around the globe. This new map [13] contains important changes to the previously used Mountain-Dresler [11] and Naruke maps [12].

In radiation therapy, lymph node stations are sometimes included in the target volume, but there is currently no consensus on whether to electively irradiate uninvolved mediastinal nodal regions [4,6]. However, the accurate delineation of node regions on thoracic CT is essential for both prognostication and treatment delivery. In 2005, Chapet et al [2] published an atlas from the University of Michigan which defined the mediastinal nodal stations for lung cancer on CT images. This atlas has been superseded by the new IASLC lymph node. Lynch et al [9] have recently published a CT atlas, based on the new IASLC lymph node map.

The descriptors for the nodal map are based on anatomical structures within the mediastinum. The mediastinal nodal stations are numbered from their superior to inferior (SI) location, starting with the supraclavicular stations 1R and 1L (R for Right and L for Left), superior mediastinal : 2R, 2L, 3A, 3P, 4R, 4L (A for Anterior, P for Posterior), aortic: 5 and 6, inferior mediastinal : 7-9, hilar, lobar and (sub)segmental : 10-14 (figure 1). Each station is described according to the surrounding anatomical structures, such as aorta, carina, trachea, various vessels, etc. The limits and boundaries between the stations are indicated. Some geometrical constructions are defined to assist in delineating some nodal stations : for example, the boundary between 2R and 2L is defined by a vertical line passing tangentially along the left lateral tracheal border.

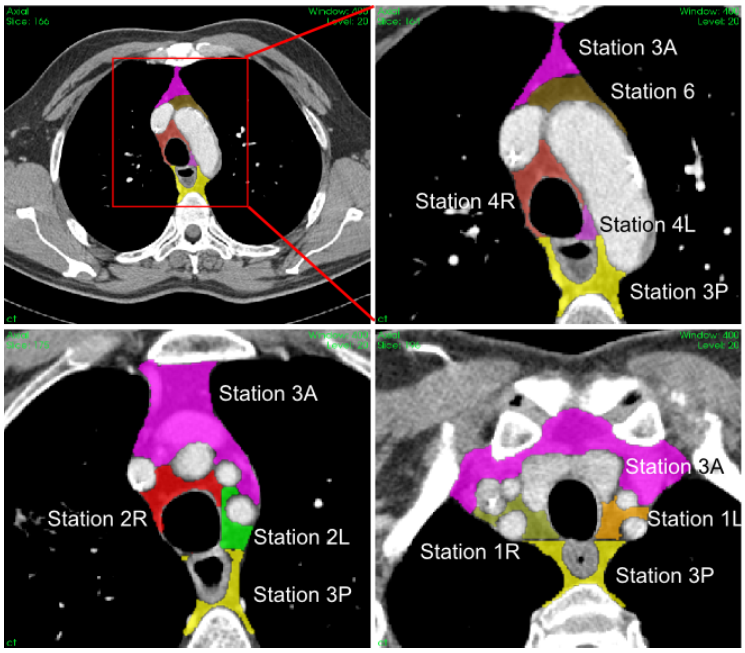

Fig. 1. Examples of mediastinal stations delineated on a thoracic CT.

The delineation of nodal stations is performed manually, on an intravenous (IV) contrasted thoracic CT, on a slice by slice basis. The guidelines make use of natural orientations, referring to AP, SI and LR axis. Manual delineation of all the normal anatomical structures and lymph node stations within the mediastinum is a time consuming process. The inter-patient anatomical variability and the inter-experts variability are high [7].

Several articles have described segmentation methods for nodal delineation, e.g. [5,10], but not for stations. Lu et al. [8] described a method to determine

cuboid (parallelepiped) regions that encompass stations. Other works proposed head and neck lymph node station segmentation for radiation therapy planning. Commowick et al. [3] proposed an atlas-based method that used deformable image registration to deform reference lymph station contours against current patient image. Good results were obtained but due to the high variability of the stations and the presence of low-contrast regions, this process can be further improved.

To our knowledge, no published work has been designed for the automated delineation of mediastinal lymph node stations. We propose an original approach, different from atlas-based and grey-level-based segmentation methods, based purely on geometrical considerations that follow the reference guidelines and attempt to replicate the delineation of nodal stations undertaken manually by the experts.

2 Method

Principles. We investigated the feasibility of segmenting the stations by following their geometrical description in the guidelines [13,9], e.g. their relative positions to surrounding anatomical structures. We tried to reproduce this description and thus made no use of the grey levels of the CT image. The proposed process was the same for all stations. It started from an initial 3D binary image S, called the support. Then, a greedy and subtraction based process was applied: at each step i some pixels were removed from the current support S_i according to anatomical and geometrical constraints. The result formed the new current support S_{i+1}; no pixels were added from step to step. After all the constraints had been applied, the last support $S_{i=last}$ was the resulting station. Geometrical constraints were defined according to identified anatomical structures that were considered to be available in the form of 3D binary images.

Relative Position (RP) constraints. We define an RP operator that considered the current support S, an object A, an angular relationship α (such as "at left of A") and a threshold t. The operator removed from S all pixels that did not fulfill the orientation relation α according to a tolerance threshold t. Following the framework of [1], the orientation relation was determined by a fuzzy map $\mu_{\alpha,A}(x)$, with $x \in S$ a pixel position, that gives at x the degree of validity of the relation. We chose the same functions to that in [1] : the fuzzy value at a given point x was a linear function $\mu_{\alpha,A}(x) = max\left(0, 1 - \frac{2\beta_{min}(x)}{\pi}\right)$ of the minimal value $\beta_{min}(x) = min_{y \in A}\beta(x,y)$ among all the angles between the considered direction $\overrightarrow{d_\alpha}$ and each point y in the object $\beta(x,y) = \arccos\frac{\overrightarrow{yx}.\overrightarrow{d_\alpha}}{||\overrightarrow{yx}||}$ and $\beta(x,x) = 0$. The fuzzy landscape was computed with the proposed fast propagation algorithm, in two passes with a neighborhood of radius 2. Once the fuzzy map was obtained, the threshold t was used to create a binary image $RP_S(A,\alpha,t)$ in which the pixel value 1 indicated at which pixel position the relationship was acceptable. If a RP contained "Not to", $1 - \mu_{\alpha,A}(x)$ was considered instead. The last step

performed the boolean intersection between this binary image and the support: $S_{i+1} = S_i \cap RP_S(A, \alpha, t)$. RP can be used in 3D (with two angles $\alpha = (\alpha_1, \alpha_2)$) or in 2D, slice by slice. We used 3D or 2D approaches according to what was indicated in the guidelines.

As we wanted to stay as close as possible to the human readable description used in the guidelines, we consider natural orientations such as "Left to" or "Not Anterior to". This lead to 12 different orientations, combined or not with the "Not To" operator. For example, if the nodal station was indicated to be "at Left to the Aorta", all of the pixels that were not to the left of the Aorta were removed. To further illustrate this point, if the nodal station was "Not Anterior to the Brachiocephalic Vein", the voxels that were anterior to this structure were discarded from the current support. Figure 2 illustrates this process.

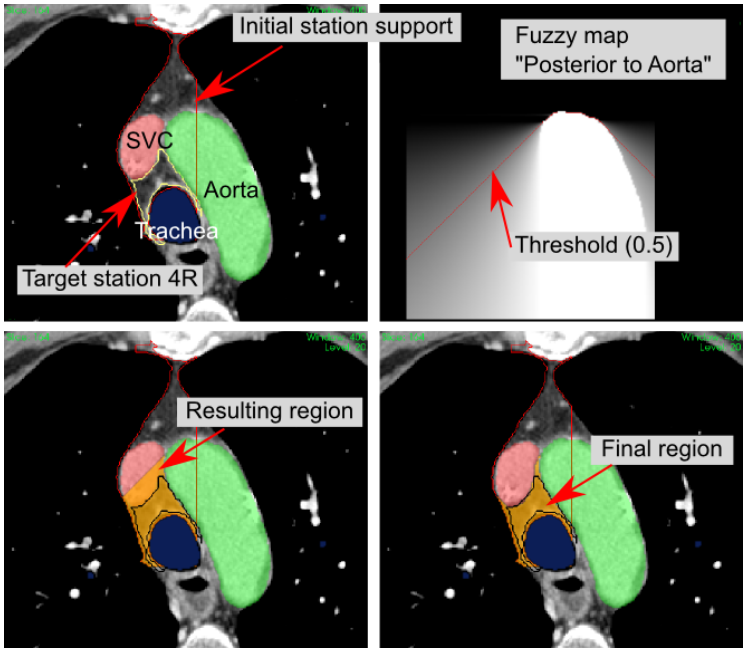

Fig. 2. Illustration of one RP operation. Initial support S_i of station 4R is shown in red contour top/left. RP is "Posterior to Aorta". The corresponding fuzzy map is shown top/right, with the threshold $t = 0.5$. Next resulting support S_{i+1} is bottom/left. Final station after other RP is bottom/right. In all images, the reference contour of target station 4R is drawn in yellow and black.

When considering several successive RP operations, fuzzy maps could be merged and a single threshold value could be used. However, we decided not to combine fuzzy maps but rather consider successive operations, like in the

guidelines. It requires one threshold by operation, but allows a better control and potential visual feedback to the user. Moreover, as the support size decreased after each RP operation, it decreased the computation time because the fuzzy maps should only be computed on the current support S_i.

Geometrical constraints. In the guidelines, in addition to the RP constraints, other geometrical descriptions were also given, such as *"The boundary between stations 2R and 2L is defined by a vertical line passing tangentially along the left lateral tracheal border"*. We translated this description into algorithms that will not be described here. Table 1 describes the anatomical structures used in the process. Some of them were obtained automatically according to methods already available by our team. The others have been delineated manually by the experts. It should be noted that the majority of structures do not need to be delineated entirely on all slices because they are only used as references within selected regions. The accuracy in the segmentation is also not a critical point because only some parts of the structures are used. For example only the anterior part of the vertebral body is use required to be delineated accurately whereas the posterior aspect can be demarcated roughly.

Initial mediastinum and stations supports. The first step consists of determining the initial support S_0 for all stations. This is done by determining a common mediastinal support automatically computed by considering areas to the left of the right lung and to the right of the left lung with the RP operator. Then we determined cuboid regions corresponding to LR, AP and SI limits of each stations, similarly to [8]. Stations were then segmented starting from superior (1R 1L), to inferior (S6), in the guidelines order. Each station description contains around 4 to 8 RP operators and geometrical limits. The different threshold values, t, were manually defined. The total process was composed of about 130 different operations (including RP).

3 Experiments and results

We tested the approach with the delineated atlases of two patients, performed by radiation oncologists in a consensus framework [9], with the new IASLC stations definition [13]. CT were acquired with IV contrast with a resolution of $0.66 \times 0.66 \times 1.5$ mm. Each atlas contains the delineation of stations (1R, 1L, 2R, 2L, 3A, 3P, 4R, 4L, 5, 6) and the anatomical structures. Delineations for other patients are in progress. We used the Dice Similarity Coefficient $DSC(A, B) = \frac{2A \cap Bt}{A+B}$ to quantify the overlap between two 3D structures A and B. We depict in table 2 the evolution of DSC between the reference station and 1) the initial whole mediastinal region S_0, 2) the initial station's parallelepiped supports S_1 and 3) the final result S_{final}.

Globally, we observed an overlap greater than 70%. There was an exception for stations 1L, p1: in that specific case we observed that the reference delineation proposed by the expert did not perfectly follow the guidelines. On some slices

	S1R	S1L	S2R	S2L	S3A	S3P	S4R	S4L	S5	S6
Bony structures										
Rib Cage					X					
Sternum	X	X	X	X	X					
CricoidCartilag (P)	X	X								
ClavicleRight	X									
ClavicleLeft		X								
FirstRibRight	X									
FirstRibLeft		X								
Artery & Veins										
Aorta			X	X		X	X	X		X
AorticArch								X	X	X
AscendingAorta					X				X	
DescendingAorta									X	
VertebralArtery	X	X				X				
SubclavianArteryRight	X		X	X	X	X				
SubclavianArteryLeft		X	X	X	X	X				
CommonCarotidArteryLeft			X	X	X					
CommonCarotidArteryRight			X	X	X					
LeftPulmonaryArtery								X	X	
MainPulmonaryArtery									X	
BrachioCephalicArtery			X	X	X					
BrachioCephalicVein			X	X			X			X
AzygousVein						X	X			
SVC (Superior Vena Cava)					X		X			X
LowerBorderAzygousVein							X			
Others										
ScaleneMuscleAnt		X								
Esophagus						X				
Trachea	X	X			X		X	X		
Thyroid	X	X	X	X		X				

Table 1. List of anatomical structures used by station. Cricoid cartilage is marked with a P, because only a point corresponding to the inferior limit of this structure is needed, not the entire contour. In addition to these structures, the patient contour, and the right and left lungs are also used.

(4 slices for 1L), posterior borders of the stations should be delimited with the most anterior point in the right and left lung. This was not the case in the expert contour, but well described by the proposed algorithm. After correction of the reference delineation for 1R and 1L, DSC rose to greater than 80%. We decided to keep this situation in order to illustrate the interest in trying to strictly follow guidelines.

4 Discussion and conclusion

The results, although limited, show that interesting segmentation can be obtained, with a mean overlap almost equal to 77%. The proposed methodology has the advantage of following guidelines in a natural way and is fast because it only considers binary images with decreasing support sizes from step to step : about 30 sec using a conventional workstation (2.6 Gz). One limitation is the need to have one threshold value for each RP (but the same for all patients). These parameters do not appear to be very sensitive due to the limited dataset

Stations	p1			p2		
	Med.	Init.	Final	Med.	Init.	Final
Station 1R	28.2%	42.1%	73.0%	24.1%	37.3%	70.4%
Station 1L	35.8%	50.1%	67.3%	27.9%	44.4%	70.3%
Station 2R	27.1%	43.3%	75.0%	25.8%	42.7%	75.8%
Station 2L	24.1%	35.6%	74.0%	25.8%	40.3%	70.5%
Station 3A	42.8%	48.6%	85.3%	33.5%	39.4%	79.8%
Station 3P	29.1%	52.2%	80.0%	33.6%	63.1%	79.2%
Station 4R	28.6%	50.0%	86.1%	30.6%	56.1%	83.1%
Station 4L	13.0%	20.1%	73.5%	9.1%	26.8%	74.0%
Station 5	20.7%	29.1%	84.5%	44.6%	63.6%	77.4%
Station 6	16.0%	22.8%	84.9%	17.8%	23.3%	73.5%

Table 2. For each station, Dice Similarity Coefficients between reference station and mediastinal support S_0 ("Med."), cuboid initial support S_1 ("Init"), and final result S_{final} ("Final").

but may become more accurate if the dataset was larger. Another limitation is that the guidelines are sometimes hard to translate into algorithmic operators. However, this could be view as an advantage because the proposed method could potentially point out ambiguities or gaps in the guidelines. If there was demonstrated uncertainty in the guidelines, this could be investigated. A further limitation of this method is the requirement to have several anatomical structures delineated prior to segmentation. However, we argue that such structures are only needed in part and segmentation could be performed automatically with conventional methods, for example with atlas or region-growing. The description of the exact part of all structures that should be delineated is also an important work that can help experts.

Our aim with this technique is not to fully replace manual delineation, but rather provide tools that can help delineations and potentially improve consistency. Several applications can be imagined. First, the resulting automated regions can be proposed to the expert as a starting point to the manual process. It is still to be determined if this could result in efficiency gains. A second application could be to compare manual delineations with the automated one in order to assist the experts in following all the guidelines. If a database of cases were available, differences between manually versus automated segmented regions could reveal potential ambiguities or deficiencies of the descriptions in the guidelines. Segmented stations could also be useful for node segmentation, to automatically label found nodes.

Regarding the proposed method, we only considered orientation relations (RP), but other topological or distance relations could be used. If a larger dataset was available, threshold values could be learnt from the delineations performed by the experts, instead of being manually defined. Future works will study such a learning approach.

We investigated here an automated method that follows the expert's guidelines for delineating mediastinal nodes stations on CT images. To our knowledge, this is the first time such an approach has been proposed for this problem. The

preliminary results are promising and will hopefully lead to further developments with a larger dataset.

References

1. Bloch, I.: Fuzzy relative position between objects in image processing: a morphological approach. IEEE Transactions on Pattern Analysis and Machine Intelligence 21(7), 657–664 (1999)
2. Chapet, O., Kong, F.M., Quint, L.E., Chang, A.C., Ten Haken, R.K., Eisbruch, A., Hayman, J.A.: CT-based definition of thoracic lymph node stations: an atlas from the University of Michigan. International Journal of Radiation Oncology, Biology, Physics 63(1), 170–8 (2005)
3. Commowick, O., Gregoire, V., Malandain, G.: Atlas-based delineation of lymph node levels in head and neck computed tomography images. Radiotherapy and oncology : journal of the European Society for Therapeutic Radiology and Oncology 87(2), 281–9 (2008)
4. Fernandes, A.T., Shen, J., Finlay, J., Mitra, N., Evans, T., Stevenson, J., Langer, C., Lin, L., Hahn, S., Glatstein, E., Rengan, R.: Elective nodal irradiation (ENI) vs. involved field radiotherapy (IFRT) for locally advanced non-small cell lung cancer (NSCLC): A comparative analysis of toxicities and clinical outcomes. Radiotherapy and oncology : journal of the European Society for Therapeutic Radiology and Oncology 95(2), 178–84 (2010)
5. Feuerstein, M., Deguchi, D., Kitasaka, T., Iwano, S., Imaizumi, K., Hasegawa, Y., Suenaga, Y., Mori, K.: Automatic mediastinal lymph node detection in chest CT. Proceedings of SPIE pp. 72600V–72600V–11 (2009)
6. Kelsey, C.R., Marks, L.B., Glatstein, E.: Elective nodal irradiation for locally advanced non-small-cell lung cancer: it's called cancer for a reason. International journal of radiation oncology, biology, physics 73(5), 1291–2 (2009)
7. Kepka, L., Bujko, K., Garmol, D., Palucki, J., Zolciak-Siwinska, A., Guzel-Szczepiorkowska, Z., Pietrzak, L., Komosinska, K., Sprawka, A., Garbaczewska, A.: Delineation variation of lymph node stations for treatment planning in lung cancer radiotherapy. Radiotherapy and Oncology 85(3), 450–5 (2007)
8. Lu, K., Higgins, W.E.: Semi-automatic central-chest lymph-node definition from 3D MDCT images. In: Karssemeijer, N., Summers, R.M. (eds.) SPIE Medical Imaging 2010: Computer-Aided Diagnosis. vol. 7624 (2010)
9. Lynch, R., Claude, L., Pitson, G., Sarrut, D.: CT Atlas for the New International Lymph Node Map: A Radiation Oncologists Perspective. Practical Radiation Oncology to appear (2012)
10. Maleike, D., Fabel, M., Tetzlaff, R., Tengg-kobligk, H.V.: Lymph node segmentation on CT images by a shape model guided deformable surface method. In: SPIE Medical Imaging (2008)
11. Mountain, C.F., Dresler, C.M.: Regional Lymph Node Classification for Lung Cancer Staging. Chest 111(6), 1718–1723 (1997)
12. Naruke, T., Suemasu, K., Ishikawa, S.: Lymph node mapping and curability at various levels of metastasis in resected lung cancer. J. Thorac. Cardiovasc. Surg. 76(6), 832–839 (1978)
13. Rusch, V.W., Asamura, H., Watanabe, H., Giroux, D.J., Rami-Porta, R., Goldstraw, P., Others: The IASLC lung cancer staging project: a proposal for a new international lymph node map in the forthcoming seventh edition of the TNM classification for lung cancer. Journal of Thoracic Oncology 4(5), 568 (2009)

Glioblastoma growth modeling for radiotherapy target delineation

Jan Unkelbach[1], Bjoern H. Menze[2], Ali R. Motamedi[1], Florian Dittmann[1], Ender Konukoglu[3], Nicholas Ayache[4], and Helen A. Shih[1]

[1] Massachusetts General Hospital, 30 Fruit Street, Boston, MA 02114, USA
[2] Computer Vision Laboratory, ETH Zürich, Switzerland
[3] Microsoft Research, Cambridge, UK
[4] Asclepios Project, INRIA Sophia Antipolis, France

Abstract. Radiotherapy treatment planning requires a localization of the tumor within the patient. This is challenging to accomplish for microscopic infiltrative spread of disease that is not visible on current imaging modalities. Prime examples for infiltrative tumors are gliomas. With the help of mathematical models, common growth characteristics of gliomas, which are known from histopathological studies, can be incorporated in radiotherapy target delineation. This requires an imaging based personalization of the model to the individual patient. We demonstrate use cases of the Fisher-Kolmogorov glioma growth model in radiotherapy planning of a clinical case. We further analyze the crucial input parameters to the model, in particular, the need for reliable segmentation of anatomical boundaries such as the falx cerebri and the tentorium cerebelli.

Keywords: glioblastoma, radiotherapy planning, target delineation, tumor modeling

1 Introduction

Glioma differ from many solid tumors in the sense that they grow infiltratively. Instead of forming a solid tumor mass with a defined boundary, glioma cells infiltrate the adjacent brain parenchyma. It is well known that tumor cells can be found several centimeters beyond the tumor mass that is visible MRI. Currently, radiotherapy planning is mostly based on the enhancing tumor mass visible on post contrast T1 weighted imaging, as well as the peritumoral edema region visible on T2 weighted images. To account for the infiltrative growth, a 2-3 centimeter wide margin is added to the visible tumor mass to form the clinical target volume (CTV), which is irradiated to a homogeneous dose of 60 Gray. The current treatment planning procedure can potentially be improved by accounting for anisotropic growth patterns of gliomas that are currently not or not consistently incorporated in target delineation. The spatial growth of glioma is influenced by three factors:

1. Anatomical boundaries: The dura, including its extensions falx cerebri and tentorium ceribelli, represents a boundary for migrating tumor cells. Also, except for rare cases of CSF seeding, gliomas do not infiltrate the ventricles.

2. Tumor cells infiltrate gray matter much less than white matter.
3. Tumor cells seem to migrate primarily along white matter fiber tracts.

These macroscopic growth characteristics are partly known from histopathological analysis after autopsy or resection. In parts, these growth patterns are also observed from MR imaging. A comprehensive review can be found in [1].

Incorporating these growth patterns in radiotherapy target volume delineation requires a combination of both mathematical tumor growth modeling and analysis of clinical imaging data. In this work, we use a phenomenological model of tumor growth based on the Fisher-Kolmogorov equation [2–4]. The patient's MRI imaging data is used to personalize the model for application in treatment planning [5–8]. The tumor growth model yields a spatial distribution of infiltrating tumor cells in the brain. This can be used in radiotherapy planning by defining the target volume as an isoline of the tumor cell density [9, 10]. For an application of the model in clinical practice, additional challenges need to be addressed. This includes a characterization of the situations in which the model based target volumes lead to differences compared to manually drawn target volumes. In addition, a sensitivity analysis is needed. The crucial inputs to the model need to be understood and the implications of uncertainty in model inputs and parameters need to be investigated.

In section 2, we briefly summarize the underlying tumor growth model. In section 3 we discuss brain segmentation which turns out to be the most crucial model input. In section 4 we present results and illustrate the use of the model for target delineation. The impact of model parameter choices is discussed.

2 Tumor growth model

2.1 Parameterization of tumor infiltration

It is assumed that two processes describe tumor growth: local proliferation of tumor cells and diffusion of cells into neighboring brain tissue. Mathematically, this is formalized via the Fisher-Kolmogorov equation, a partial differential equation of reaction-diffusion type for the tumor cell density $c(\boldsymbol{r}, t)$ as a function of location $\boldsymbol{r}$ and time t:

$$\frac{\partial}{\partial t} c(\boldsymbol{r}, t) = \nabla \cdot \left(D(\boldsymbol{r}) \nabla c(\boldsymbol{r}, t) \right) + \rho c(\boldsymbol{r}, t) \left(1 - c(\boldsymbol{r}, t) \right) \tag{1}$$

where ρ is the proliferation rate which is assumed to be spatially constant, and $D(\boldsymbol{r})$ is the 3×3 diffusion tensor which depends on location $\boldsymbol{r}$. The first term on the right hand side of equation 1 is the diffusion term that models tumor cell migration into neighboring tissue. The second term is a logistic growth term that describes tumor cell proliferation. In this paper, the diffusion tensor is constructed as

$$D(\boldsymbol{r}) = \begin{cases} D_w \cdot I & \boldsymbol{r} \in \text{white matter} \\ D_g \cdot I & \boldsymbol{r} \in \text{gray matter} \end{cases} \tag{2}$$

where I is the 3×3 identity matrix, and D_g and D_w are scaling coefficients for gray and white matter, respectively. At the boundary of brain tissue consisting of white and gray matter we impose no-flux boundary conditions. In summary, the three growth characteristics described in the introduction are reflected in the model as follows:

1. **Anatomical boundaries:** Are handled through no-flux boundary conditions at the boundary to CSF. It is assumed that infiltrating tumor cells are restricted to white and gray matter and do not infiltrate the ventricles or penetrate the dura.
2. **Reduced gray matter infiltration:** Is described via a larger diffusion coefficient in white matter versus gray matter ($D_w/D_g > 1$).
3. **Preferential spread along white matter fiber tracts:** Can be described via an anisotropic diffusion tensor D. Within white matter, the identity matrix I in equation 2 is replaced by a tensor proportional to the water diffusion tensor that is reconstructed from diffusion tensor MR imaging (DTI) [11, 12]. This is however not considered in this paper.

In this paper, we utilize the model to infer the tumor cell density at the time of diagnostic imaging. A naive integration of the model equation 1 is problematic because the initial condition that corresponds to the current tumor appearance on MRI is unknown. We therefore apply a method previously published in [9] that is based on the traveling wave approximation[5].

2.2 Image based model personalization

In order to apply this model for target delineation, the model equation (1) has to be personalized to the individual patient. This process involves two steps: first, a segmentation of the brain, and second, the choice of model parameters.

Segmentation A segmentation of the brain into the three classes white matter, gray matter, and cerebrospinal fluid (CSF) [6] is required in order to solve the model equation based on the individual patient geometry. The brain segmentation is obtained from the structural MR images, including T1, T2, FLAIR and T1 post contrast. Figure 3 shows an example patient discussed in this paper. Figure 3a shows the coronal T1 weighted post contrast image, revealing a contrast enhancing glioblastoma in the right parietal lobe next to the falx. Also the tentorium cerebelli, representing a boundary for migrating tumor cells, is clearly visible. Figure 3b shows the peritumoral edema visible in the axial FLAIR image. The brain segmentation is shown in 3c. The segmentation methods are discussed in more detail in section 3.

[5] For details see [9]. For the results shown in this paper, it is assumed that the boundary of the enhancing tumor mass on the T1 post contrast image corresponds to a tumor cell density of 70%.

[6] Here, we refer to all tissue that is neither white nor gray matter as CSF, ever though more classes for non-brain tissue can be used in the segmentation.

Model parameters In addition, model parameters need to be determined. For this work, the main model parameter is the ratio D_w/D_g of the diffusion coefficients in white and gray matter[7]. Ideally, model parameters are also estimated for an individual patient. For the parameter D_w/D_g this is difficult to accomplish. Hints on reduced gray matter infiltration mainly comes from histopathological analysis [1], which is not available for an individual patient. To a limited degree, the shape of the edematous region visible on the FLAIR image contains information about the microscopic spread of tumor cells. However, the edema is only a surrogate for infiltrative disease. In many cases, the edema region is mostly confined to white matter. It is, however, unclear to what extent this can be seen as evidence for reduced tumor cell infiltration in gray matter, as this may be due to other physiological reasons [1]. In summary, it is commonly believed that $D_w/D_g \gg 1$, but quantification remains difficult. It is therefore important to discuss the implications of parameter uncertainty for radiotherapy target delineation (as addressed in section 4).

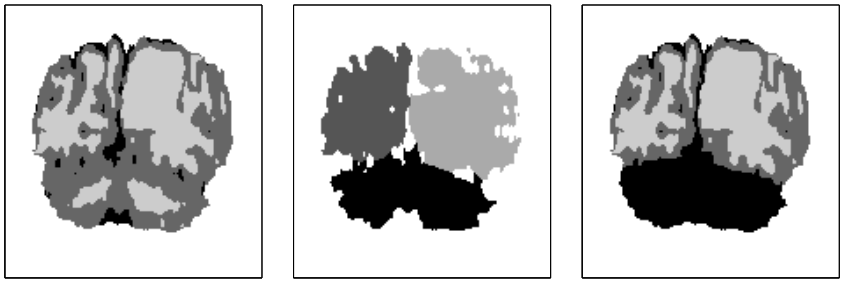

(a) (b) (c)

Fig. 1. (a) EM based brain segmentation into white matter (light gray), gray matter (dark gray), and CSF (black). (b) Segmentation of the cerebral hemispheres and the cerebellum. (c) final segmentation after using the hemisphere segmentation in (b) to remove the cerebellum and separate the hemispheres.

3 Brain segmentation

Modeling the spatial growth of the tumor requires a segmentation of gray matter, white matter, CSF, and non-brain tissue. The normal brain segmentation is primarily based on an Expectation-Maximization (EM) algorithm [13]. The basic component of an EM brain segmentation algorithm can be thought of as

[7] The proliferation rate ρ influences the velocity of tumor growth and how fast the cell density drops with distance from the core [8, 9]. It has however minimal influence on the shape of the tumor, i.e. the spatial shape of the isolines of the tumor cell density (which is the only relevant property in this work).

a gaussian mixture model of the image data. It is assumed that each of white matter, gray matter, and CSF has a characteristic mean image intensity. The actual pixel intensities in the image are assumed to be gaussian distributed around the mean. For segmentation, the class mean values and the class affiliations for every pixel are estimated by maximizing the data likelihood using EM. To favor smooth segmentation boundaries, the basic gaussian mixture model can be augmented by a markov random field regularization term. Here, we adapt out previously published EM based segmentation algorithm, which simultaneously estimates the normal brain segmentation as well as the tumor segmentation on the available sequences [13].

The EM based segmentation algorithm is almost entirely based on gray value information in the image and does not incorporate anatomical information. It yields adequate results for the discrimination of white matter and gray matter. However, it often fails to reliably segment certain anatomical boundaries. This applies in particular to the tentorium cerebelli, an extension of the dura that separates the cerebellum from the cerebral hemispheres. The membrane is thin and consists of only one or two image pixels. In addition, the EM based segmentation may insufficiently separate the cerebral hemispheres through a layer of CSF. This may in particular occur if a tumor mass close to the falx pushes against the membrane. This is illustrated in figure 1, which shows results of the brain segmentation on the coronal slice shown in figure 3a. Figure 1a shows the EM based segmentation. Typically, gray matter and white matter are sufficiently differentiated. However, the algorithm fails to separate the two hemispheres near the tumor mass, and fails to identify the tentorium cerebelli. For a reliable application of the tumor growth model for target delineation, the result of the EM based segmentation has to be enhanced via anatomical information.

Here, we adapt the adaptive disconnection algorithm published by Zhao [14], a method to segment the cerebellum as well as the two cerebral hemispheres. A result of the adaptive disconnection algorithm is shown in figure 1b. This anatomical information is used to amend the EM based segmentation. First, the cerebellum is removed. This is motivated by the fact that supratentorial gliomas almost never infiltrate the cerebellum. In addition, a two pixel thick layer in between the two hemispheres is identified. These pixels are marked as CSF in the final brain segmentation if those pixels were gray matter in the original EM based segmentation. White matter pixels in the EM segmentation are unchanged in order to leave the corpus callosum in tact, which connects the two hemispheres via white matter fiber tracts. The corrected segmentation is shown in figure 1c.

4 Model based target delineation

4.1 Spatial distribution of tumor cells

Figure 2 shows the simulated tumor cell density for three different values of the parameter D_w/D_g on the axial slice shown in figure 3b. For $D_w/D_g = 1$ (figure 2a), the anisotropy in tumor growth is only dependent on anatomical boundaries. In the example shown here, the tumor growth model can be used

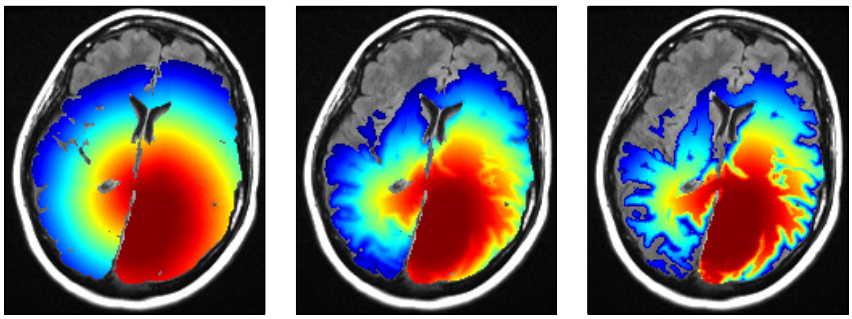

(a) $D_w/D_g = 1$ (b) $D_w/D_g = 10$ (c) $D_w/D_g = 100$

Fig. 2. Simulated tumor cell density on a logarithmic scale for three different values of the parameter D_w/D_g.

to consistently model the complex anatomical conditions created by the falx (representing a boundary) and the corpus callosum (representing a route for tumor cells to spread to the contralateral hemisphere). This is difficult to take into account for in manual target delineation. For $D_w/D_g = 100$ (figure 2c), the tumor cell density follows closely the white matter structure, which can be seen from the comparison to the segmentation in figure 3c. For $D_w/D_g = 10$ (figure 2b) an intermediate result is obtained.

4.2 Target volume definition

For radiotherapy planning, the tumor growth model is used to define the target volume as an isoline of the tumor cell density. This is illustrated in figures 3a and 3b. Shown are the model derived target volumes for the tumor cell densities in figure 2. The contours correspond to the same isoline of the tumor cell density. This isoline was chosen based on the tumor cell density for $D_w/D_g = 1$ such that the size of the model derived target volume matches the size of the manually drawn target volume that was used in the clinically applied treatment plan.

It is apparent that the target volumes for different values of the parameter D_w/D_g are not substantially different, even though the simulated tumor cell densities in figure 2 appear very distinct. The reason for that is the limited thickness of the cortex, i.e. gray matter represents a layer on top of the white matter structure that is only a few millimeters thick. Therefore, reduced infiltration of gray matter has limited influence in the global shape of the target volume. It mainly leads to local changes around the sulci. For large D_w/D_g values, a thin layer of gray matter surrounding the sulci is excluded from the target volume. However, for this patient, this has little impact on radiotherapy planning, because such small volumes cannot be spared from with available irradiation techniques.

Reduced gray matter infiltration may lead to more substantial changes in the target volumes near large accumulations of gray matter. This is, for example, the

case for tumors located closer to the lateral sulcus (Sylvian fissure). In that case, large areas of gray matter are excluded from the target volume for $D_w/D_g = 100$ (results not shown).

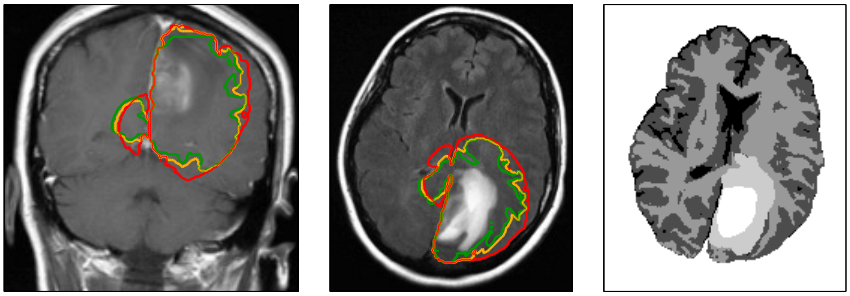

(a) (b) (c)

Fig. 3. Radiographic appearance of a glioblastoma: (a) coronal T1 weighted post contrast image, (b) axial FLAIR image. The three contours show the model derived target volumes discussed in section 4 (red, $D_w/D_g = 1$; yellow, $D_w/D_g = 10$; green, $D_w/D_g = 100$). Figure (c) shows the brain segmentation into CSF, gray matter, white matter, edema, and enhancing core (from black to white).

5 Conclusion

Gliomas show complex spatial growth patterns, which are influenced by anatomical boundaries and the distribution of white and gray matter. These growth characteristics can be formalized using a reaction-diffusion equation. A brain segmentation based on MRI images is used to personalize the tumor growth model. In our work, we aim at bringing this tumor growth model to an application in radiotherapy target delineation. In the first stage, the model can be used to consistently incorporate anatomical boundaries into target delineation. This is in particular useful for tumors located close to the falx and the corpus callosum. This approach only requires a reliable segmentation of the brain. In this paper, this has been achieved via a hybrid approach where an EM based brain segmentation is enhanced by a segmentation of the cerebral hemisphere and the cerebellum. In the next stage, reduced gray matter infiltration can be incorporated. For most parts of the target volume, this has little impact on radiotherapy planning because the cortical thickness is only a few millimeters. However, in regions of major sulci with large accumulations of gray matter, the model can suggest regions where the target volume can be trimmed.

References

1. S. W. Coons. Anatomy and growth patters of diffuse gliomas. In M. S. Berger and C. B. Wilson, editors, *The gliomas*, pages pp 210–225, Philadelphia, PA, USA, 1999. W.B. Saunders Company.
2. Murray J.D. *Mathematical Biology II: Spatial Models and Biomedical Applications*. Springer, 2002.
3. H. L. P. Harpold, E. C. Alvord, and K.R. Swanson. The evolution of mathematical modeling of glioma proliferation and invasion. *J. Neuropathology Exp Neurol*, 66(1):1–9, 2007.
4. E. Mandonnet, J. Pallud, O. Clatz, L. Taillandier, E. Konukoglu, H. Duffau, and L. Capelle. Computational modeling of the WHO grade II glioma dynamics: principles and applications to management paradigm. *Neurosurg Rev*, 31(3):263–269, Jul 2008.
5. E.D. Angelini, O. Clatz, E. Mandonnet, E. Konukoglu, L. Capelle, and H. Duffau. Glioma dynamics and computational models: a review of segmentation, registration, and in silico growth algorithms and their clinical applications. *Current Medical Imaging Reviews*, 3(4):262–276, 2007.
6. N. C. Atuegwu, J. C. Gore, and T. E. Yankeelov. The integration of quantitative multi-modality imaging data into mathematical models of tumors. *Phys Med Biol*, 55(9):2429–2449, May 2010.
7. Bjoern H. Menze, Koen Van Leemput, Antti Honkela, Ender Konukoglu, Marc-Andr Weber, Nicholas Ayache, and Polina Golland. A generative approach for image-based modeling of tumor growth. *Inf Process Med Imaging*, 22:735–747, 2011.
8. Ender Konukoglu, Olivier Clatz, Bjoern H. Menze, Bram Stieltjes, Marc-Andr Weber, Emmanuel Mandonnet, Herve Delingette, and Nicholas Ayache. Image guided personalization of reaction-diffusion type tumor growth models using modified anisotropic eikonal equations. *IEEE Trans. Med. Imaging*, 29(1):77–95, 2010.
9. Ender Konukoglu, Olivier Clatz, Pierre-Yves Bondiau, Herve Delingette, and Nicholas Ayache. Extrapolating glioma invasion margin in brain magnetic resonance images: Suggesting new irradiation margins. *Medical Image Analysis*, 14:111–125, 2010.
10. D. Cobzas, P. Mosayebi, A. Murtha, and M. Jagersand. Tumor invasion margin on a riemannian space of brain fibers. In *LNCS 5762 Proc. MICCAI Part 2*, pages pp 531–39, Heidelberg, Germany, 2009. Springer.
11. O. Clatz, M. Sermesant, P. Y. Bondiau, H. Delingette, S. K. Warfield, G. Malandain, and N. Ayache. Realistic simulation of the 3-D growth of brain tumors in MR images coupling diffusion with biomechanical deformation. *IEEE Trans Med Imaging*, 24(10):1334–1346, Oct 2005.
12. Sad Jbabdi, Emmanuel Mandonnet, Hugues Duffau, Laurent Capelle, Kristin Rae Swanson, Mlanie Plgrini-Issac, Rmy Guillevin, and Habib Benali. Simulation of anisotropic growth of low-grade gliomas using diffusion tensor imaging. *Magnetic Resonance in Medicine*, 54(3):616–624, 2005.
13. B. Menze, K. Van Leemput, D. Lashkari, M. Weber, N. Ayache, and P. Golland. A generative model for brain tumor segmentation in multi-modal images. In *Proc MICCAI*, Heidelberg, 2010. Springer.
14. Lu Zhao, Ulla Ruotsalainen, Jussi Hirvonen, Jarmo Hietala, and Jussi Tohka. Automatic cerebral and cerebellar hemisphere segmentation in 3d mri: Adaptive disconnection algorithm. *Medical Image Analysis*, 14(3):360–372, 2010.

Segmentation and characterization of tumors in 18F-FDG PET-CT for outcome prediction in cervical cancer radio-chemotherapy

Geoffrey Roman-Jimenez[1,2], Julie Leseur[2,3], Anne Devillers[1,2,3], Juan David Ospina[1,2], Guillaume Louvel[2,3], Pascal Haigron[1,2], Antoine Simon[1,2], Renaud de Crevoisier[1,2,3], and Oscar Acosta[1,2]

[1] INSERM, U 1099, Rennes, F-35000, France
[2] Université de Rennes 1, LTSI, F-35000, France
Geoffrey.Roman-Jimenez@univ.rennes1.fr
[3] Département de Radiothérapie, Centre Eugène Marquis, Rennes, F-35000, France

Abstract. Cervical cancer is one of the most common cancer to affect women worldwide. Despite the efficiency of radiotherapy treatment, some patients present recurrency. Early unfavorable outcomes prediction could help oncologist to adapt the treatment. Several studies suggest that tumor characteristics visible with ^{18}F-FDG PET imaging before and during the treatment could be used to predict post-treatment recurrency. We present a framework for segmentation and characterization of metabolic tumor activity aimed at exploring the predictive value of pre-treatment and per-treatment ^{18}F-FDG PET images. Thirty-five patients with locally advanced cervix cancer treated by chemoradiotherapy were considered in our study. For each patient, a coregistered PET/CT scan was acquired before and during the treatment and was segmented and characterized with our semi-automated framework. A segmentation process was applied on the baseline acquisition in order to find the metabolic tumor region (MTR). This MTR was propagated to the follow-up acquisition using a rigid registration step. For every patient, 40 features from the two MTRs were extracted to characterize the tumor changes between the two observation points. We identified explanatory characteristics by exploring the threshold which minimizes the p-value computed from the Kaplan-Meier free-disease survival curves. Seven features were identified as potentially correlated with cancer recurrency (p-value<0.05). Results suggest that our method can compute early meaningful features that are related with tumor recurrence.

Keywords:PET/CT, cervical cancer, radiotherapy, tumor recurrence prediction, image characterization

1 Introduction

Nowadays, cervical cancer is the third most common cancer and the fourth cause of cancer death in females worlwide with 529,800 cases diagnosed and 275,000 cancer deaths in 2008 [1]. The standard treatment of locally advanced cervical cancer is based on chemoradiotherapy and brachytherapy, inducing a risk of acute and late irreversible toxicity[2]. Because recurrence in cervical cancer significantly increase the risk of death [3], prediction of such events is crucial. Medical imaging can provide different

markers not only to plan the therapy but also to help oncologist to adapt the incourse treatment thereby increasing the chance of patients survival. During the last decade, severals studies have shown that coregistered PET/CT improve the diagnostic accuracy in several cancers [4][5]. As opposed to anatomic imaging such as CT or MRI, PET provides metabolic information of the tumor. Since metabolic changes of the tumor precede the morphologic modifications, PET-based studies could provide early prediction outcomes. Several studies have demonstrated that metabolic tumor changes occuring between PET scans allow to quantitatively assess tumor response [6][7]. Further, some studies have shown the predictive value of the informations extracted in PET [8][9].

In this study, we present a semi-automated framework for segmentation and characterization of metabolic tumor activity in cervical cancer from pre and per-treatment PET/CT acquisitions. We demonstrate the utility of our framework in predicting recurrency on a cohort of 35 patients treated for locally advanced cervix cancer. In the proposed framework the pre-treatment PET/CT fused information is exploited to first isolate the tumoral region from the rest of the image, then several characteristics are extracted from the PET at two time points during the treatment to find features that may explain recurrency. The identification of the recurrency correlated features was performed using Kaplan-Meier survival curves and the log-rank test.

2 Materials & Methods

2.1 Data and Clinical Protocol

Thirty-five patients (median age 52.44 years [32.15 - 84.62]) with locally advanced cervix cancer treated at the Centre Eugene Marquis (CEM), Rennes, France, were considered. The patients were treated with external beam radiation therapy (EBRT) with concurrent chemotherapy (CDDPcc) followed by brachytherapy (BT). With median follow-up of 29.21 months [7.44 - 52.64], eight patients developed tumor recurrence and three patients died. As shown in Fig. 1, each patient underwent three ^{18}F-FDG PET/CT scans performed with a DISCOVER ST scanner each observing the same time between injection and acquisition. In our study, we will only consider the pre and per-treatment acquisitions. The two pre-treatment images are denoted PET1 and CT1. At 40 Gy of the EBRT, the acquisitions were denoted PET2 and CT2. In order to have the images comparables, each PET image was converted into standardized uptake value (SUV) which is a standardized decay-corrected value of ^{18}F-FDG activity per unit volume of body weigth (MBq/kg)[11].

2.2 Segmentation & Characterization of the metabolic tumor region

The framework of the proposed method is illustrated in Fig. 2. The first step aims to isolate the tumoral area in PET1, avoiding the bladder hyperfixation. Because the tumor uptake in PET2 is less visible in responder patients due to the treatment, a rigid registration is carried out to map the region found in PET1 on PET2 thereby accessing to the same tumoral region. In step three, the two regions found in the previous stages are used to characterize the tumor before and during the treatment through features computation.

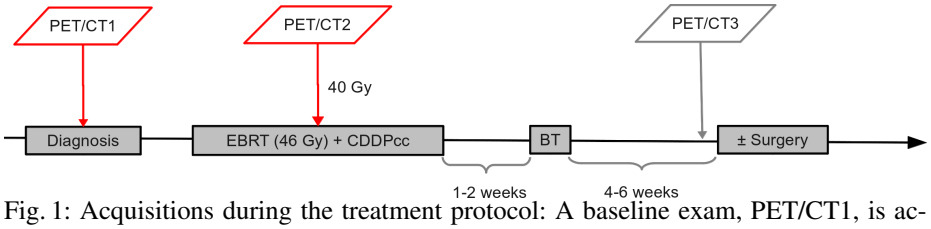

Fig. 1: Acquisitions during the treatment protocol: A baseline exam, PET/CT1, is acquired before the treatment. A second acquisition, PET/CT2, is performed at 40 Gy of the chemoradiotherapy. The last acquisition, PET/CT3, is performed 4-6 weeks after the brachytherapy

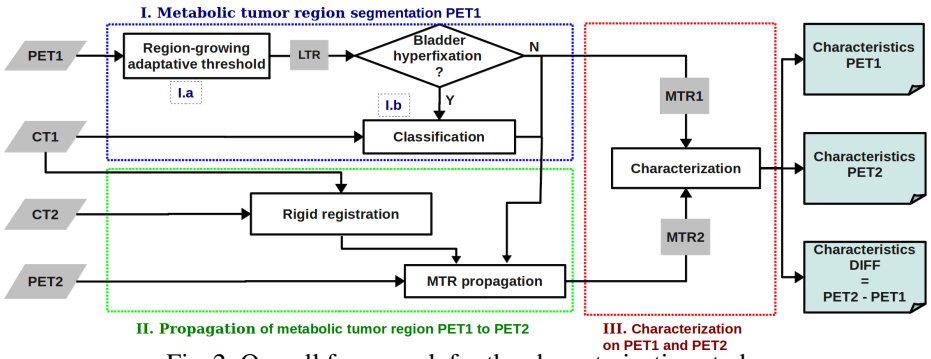

Fig. 2: Overall framework for the characterization study.

I. Metabolic tumor region segmentation in PET1: The metabolic tumor region (MTR) is denoted as the region where the acquired ^{18}F-FDG uptake corresponds to the tumor activity. The purpose of this step is to determine the metabolic tumor region in PET1 (MTR1). We considered here that the ^{18}F-FDG hyperfixation of the tumor before the treatment is topologically compact (one connected object). In that case, a region-growing threshold allows to select the voxels belonging to the MTR1. Region-growing was used to limited the inclusion of adjacent intense structures, such as the bladder, lymph nodes, and bowel [20].

I.a - *Region-growing adaptative threshold (RGAT)*: Let's denote likely tumoral region (LTR) the region wherein the ^{18}F-FDG hyperfixation is high enough to be considered as tumor metabolism. In order to extract the LTR, an adaptative threshold as the one proposed by Daisne [10] was implemented. This method aimed to adapt the threshold needed to segment the LTR according to the signal-to-background (S/B) measured in the image. The relationship between S/B and the threshold required was set up through a physical phantom study. Thus, because of the compactness hypothesis, the threshold was applied using a region-growing in order to keep a compact LTR.

I.b - *Fusion and gaussian mixture based classification (FGMC)*: Due to natural filling and emptying of the bladder, ^{18}F-FDG can be fixed in an extremely variable way leading to part of the bladder having intensities comparable to tumoral metabolism. It was necessary to visually determine if voxels in the bladder were selected in the LTR. In such case, a second step of classification was required to separate bladder and tumor. Firstly, the CT images were downsampled to the PET resolution so that each voxel in

PET correspond to only one voxel in CT. A voxel seed was selected as being likely within the tumor. From each voxel selected in the LTR, three features were considered: the standard uptake value on PET (SUV), the Hounsfield unity value on CT (HU) and a tumor membership probability (TMP). The group of voxels in LTR was thus denoted as $X = \{x_i | i \in I\}$. With x_i, a three feature vector $[SUV\ HU\ TMP]$ at the voxel i and I, the 3D coordinates in the image. We computed the TMP as:

$$TMP(x_i) = 1 - \frac{d(x_i, s)}{\max\limits_i d(x_i, s)}, \tag{1}$$

where $d(x_i, s)$ is the Euclidean distance of the voxel x_i from the seed s, and $\max\limits_i d(x_i, s)$ denote the Euclidean distance of the furthest voxel in the LTR from the seed. It was assumed that the further the voxel is from the reference the lower is the probability to belong to the tumor. SUV and HU were normalized between 0 and 1. The three normalized features were then projected in the tri-parametric space represented in Fig. 3. Voxels belonging to the tumor were identified by fitting a gaussian mixture model (GMM). In general terms, the GMM expresses that the distribution of points in this tri-parametric space is a sum of gaussian functions. Two clusters were considered: a cluster T representing voxels in the MTR and a cluster B for voxels in the bladder(eq 2).

$$g(x_i, \Theta) = p_T.f_T(x_i, \mu_T, \Sigma_T) + p_B.f_B(x_i, \mu_B, \Sigma_B), \tag{2}$$

where g denotes the mixture density of each LTR-voxel x_i. The constants p_T and p_B are the mixing proportions of the two gaussian distributions f_T and f_B respectively characterized by the means μ_T and μ_B and variance matrix Σ_T and Σ_B. Θ represents the model parameters of the gaussians mix $\Theta = [p_T, p_B, \mu_T, \mu_B, \Sigma_T, \Sigma_B]$ need to be estimated.

An expectation-maximization algorithm (EM) was used to calculate the maximum likehood estimates of Θ. Given these estimates, each voxel was assigned a label stating if it belongs to the cluster T or B. Fig. 3 gives an example of clustering in the classification space.

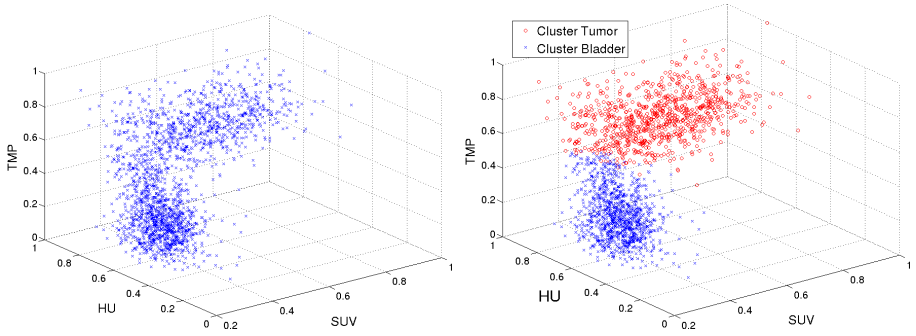

Fig. 3: Fusion and gaussian mixture based classification. (left) Tri-parametric classification space : SUV value, Hounsfield value and Tumor Membership Probability. (right) resulting EM estimation.

The largest connected component in the cluster "Tumor" was selected to be the MTR. Fig. 4 summarizes an example of metabolic tumor region segmentation in the pre-treatment PET.

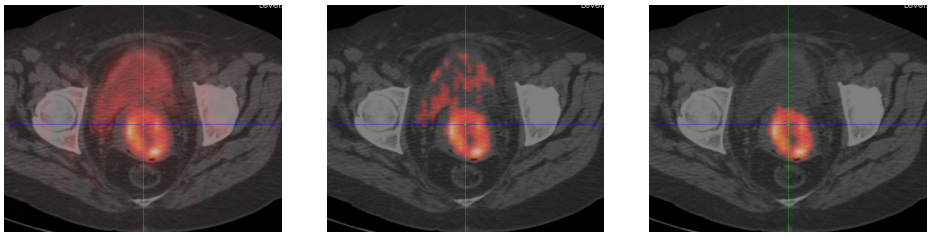

Fig. 4: Example of metabolic tumor region segmentation in PET1. (left) PET/CT1 with a high bladder uptake. (middle) LTR after RGAT. (right) MTR1 after the FGMC.

II. MTR1 to MTR2 registration: This step aims to propagate the MTR extracted in the PET1 to PET2. The propagated MTR was denoted MTR2. Since PET are coregistered with CT, these CT images were used to determine the transformation between PET images. A two-step registration using a block-matching algorithm [12] was adopted. Firstly, CT1 to CT2 were registered in order to match the whole body. Secondly, a rigid registration was applied locally to align the cervix. In practice, this is obtained by registering a VOI around the cervix. Note that local rigid registration was assumed because of the restricted VOI considered. This allows to keep the same shape between MTR in PET1 and PET2 and thus keep the same tumor area.

III. Characterization: Fourteen features were extracted from the two PET MTR to characterize patient's tumor before and during the treatment. In addition to SUVmax, metabolic tumor volume (MTV) and total lesion glycolysis (TLG) often reported in literature [13][14][8], we explored intensity and texture features[15][16]. The features are summarized in tables 1 and 2.

Note that, in PET1, the total activity by voxel volume (TAVV), is equivalent to the total lesion glycolysis (TLG) calculated as $SUV_{mean} \times MTV$ when MTV is well defined. Since we estimated the MTR2 by registration, the TAVV can not be denoted as TLG because MTV in PET2 is roughly delineated. However, for a good responder, it was expected that if the activity outside the true MTV was neglected, the TAVV will give a good approximation of the TLG.

Texture features, originally proposed by Haralick[18], are based on the co-occurence matrix Φ, reflecting spatial grey-level dependencies. The intensity range into the MTR was quantified with 16 bins. The texture features calculated shown in Tab. 2 were computed for every direction covering the 26-connected neighborhood and were averaged to keep a restricted number of characteristics. Finally, to characterize the changes between PET1 and PET2, the difference (DIFF) was calculated between features evaluated in MTR1 and MTR2.

2.3 Tumor recurrence prediction

A total of 40 features were extracted from 35 patients. Fourteen features were extracted from PET1, 13 features from PET2 and 13 from DIFF. The Kaplan-Meier method was

Features	Formula	Definition
SUVmax	$max(X)$	Maximal uptake in the MTR
SUVpeak	$\frac{1}{K}\sum_{k}^{K} x_k, k \in max_{neighbor}$	SUVmax averaged by its 26 neighbors
SUVmean	$\mu = \mathbb{E}[X]$	Average of SUV in the MTR
SUVvariance	$\Sigma = \mathbb{E}[(X-\mu)^2]$	Variance of SUV in the MTR
SUVskewness	$\gamma_1 = \mathbb{E}\left[\left(\frac{X-\mu}{\Sigma}\right)^3\right]$	Asymmetry measure of the MTR activity distribution
SUVkurtosis	$\gamma_2 = \mathbb{E}\left[\left(\frac{X-\mu}{\Sigma}\right)^4\right]$	Peakedness measure of the MTR activity distribution
MTV	$Volume_{voxel} \times Nb_{Voxel}$	Metabolic Tumor Volume of the MTR
TAVV	$Volume_{voxel} \times \sum_{n}^{N} x_n$	Total Activity by Voxel Volume of the MTR

Table 1: Evaluated intensity features

Features	Formula
Energy	$\sum_{i,j} \Phi(i,j)^2$
Entropy	$\sum_{i,j} \Phi(i,j) \times log_2(\Phi(i,j))$
Inertia	$\sum_{i,j} (i-j)^2 \times \Phi(i,j)$
InverseDifferentMoment (IDM)	$\sum_{i,j} (i-j)^2 \times \Phi(i,j)$
Cluster Shade	$\sum_{i,j} (i+j-\mu_j-\mu_i)^3 \times \Phi(i,j)$
Cluster Prominence	$\sum_{i,j} (i-\mu_i+j-\mu_j)^4 \times \Phi(i,j)$

Table 2: evaluated texture features

used to evaluate the disease-free survival curves of the group splitted by a threshold. The feature assessment was perfomed following this method: for each feature, a threshold was found in order to minimize the p-value of the log-rank test from the comparison of the two survival curves generated when splitting the group using this threshold. The level of significance for the log-rank test was fixed to p-value<0.05.

3 Results

3.1 FGMC evaluation

Among the 35 PET1 segmented in step I.a, 12 visually presented high bladder uptake and were clustered in step I.b. In order to evaluate the deletion of bladder voxels performed by the FGMC, we used expert manual cervix and bladder CT-segmentation available for six patients. After I.b, the number of voxels remained in the cervix mask was considered as true positive (TP) whereas false positive (FP) was the number of those in the bladder mask. For the six clusterization evaluated, the averaged results

were 0.80 ± 0.17 sensitivity, 0.97 ± 0.08 specificity and 0.85 ± 0.11 accuracy. We can observe a lower sensitivity due to the worst patient which presented a classification with 0.53 sensitivity, 1.00 specificity and 0.63 accuracy. In this case, the patient presented a small tumor and as the number of voxels in the cervix mask in LTR was limited, any suppressed voxel during the FGMC had an important impact on the resulting sensitivity.

3.2 Explanatory features identification

Tab. 3 summarizes the significant features extracted in step III. Results show that the explanatory features found are mainly based on SUV intensity. The four characteristics found from PET1 might suggest that tumor recurrence could be predicted before the treatment. Moreover, the TAVV evolution between the two exams(DIFF) might be a recurrency correlated feature that could be used by oncologists to adapt the ongoing treatment. An example of a Kaplan-Meier curve with the TAVV feature in PET1 and DIFF is diplayed in Fig. 5.

exam	feature	p-value	threshold
PET1	SUVmax	0.0335	10.52
	SUVpeak	0.0478	7.27
	SUVmean	0.0335	6.30
	TAVV or TLG	0.0114	155.62
PET2	SUVmax	0.0307	6.26
	IDM	0.0419	0.16
DIFF (PET1-PET2)	TAVV	0.0171	-266.15

Table 3: Assessed features by the Kaplan-Meier method with p-value<0.05 and the corresponding threshold.

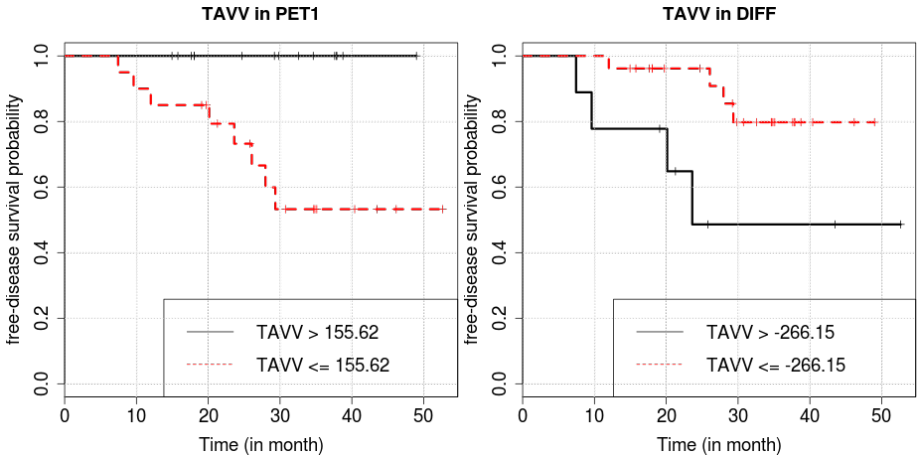

Fig. 5: Example of feature evaluation with Kaplan-Meier method. (left) TAVV in PET1 (p-value=0.0114). (right) TAVV in DIFF (p-value=0.0171).

4 Discussion & Conclusion

In this study, we presented a whole framework to characterize cervical cancer tumor from ^{18}F-FDG PET imaging and to predict its response to radiotherapy. One of the challenges was to isolate the tumor region from the bladder in PET1. With the use of CT information, we proposed a semi-automated method to segment and characterize PET imaging based on a RGAT followed by a FGMC approach. Since metabolic informations can be hidden in lower uptake than the applied threshold, an intensity-based segmentation can lead to an underestimation of the true LTR extracted. Also, an adaptative threshold suffers from poor reproducibility[19] and a more evolved segmentation method could enhance this. The FGMC has demonstrated the ability to classifying voxels between tumor and bladder with good specificity, sensitivity and accuracy (respectively 0.80, 0.97 and 0.85). Nonetheless, for one given patient, we visually decided if the classification step was necessary. An integration of the FGMC into the segmentation step is in progress in order to reduce user dependency. The characterization step was perfomed by evaluating intensity and texture features on MTR1 and MTR2. Also, we characterized the tumor changes by computing the difference between the features in MTR1 and MTR2. In future work, shape metrics could be extracted to describe the tumor thereby providing complimentary information. We identified seven features that might be correlated with cervical cancer recurrency by assessing free-disease survival curves. This is an exploratory study so, in future work, the predictive capabilities of the found thresholds will be assessed through a larger cohort of patients.

References

1. Jemal *et al.*, Global cancer statistics. CA: A Cancer Journal for Clinicians **61** (2011) 69–90
2. Kirwan *et al.*, A systematic review of acute and late toxicity of concomitant chemoradiation for cervical cancer. Radiother Oncol **68** (2003) 217–226
3. Sommers *et al.*, Outcome of recurrent cervical carcinoma following definitive irradiation. Gynecologic Oncology **35** (1989) 150 – 155
4. Bar-Shalom *et al.*, Clinical performance of pet/ct in evaluation of cancer: additional value for diagnostic imaging and patient management. J Nucl Med **44** (2003) 1200–1209
5. Dhingra *et al.*, Impact of fdg-pet and -pet/ct imaging in the clinical decision-making of ovarian carcinoma: an evidence-based approach. Womens Health (Lond Engl) **8** (2012) 191–203
6. Necib *et al.*, Detection and characterization of tumor changes in 18f-fdg pet patient monitoring using parametric imaging. J Nucl Med **52** (2011) 354–361
7. David *et al.*, Multi-observation pet image analysis for patient follow-up quantitation and therapy assessment. Phys Med Biol **56** (2011) 5771–5788
8. Leseur *et al.*, Metabolic monitoring by 18f-fdg pet during radio-chemotherapy for locally advanced cervical cancer: Predicting outcome. International Journal of Radiation Oncology*Biology*Physics **81** (2011) S47–S48 53rd Annual Meeting ASTRO's.
9. Chung *et al.*, Clinical impact of integrated pet/ct on the management of suspected cervical cancer recurrence. Gynecol Oncol **104** (2007) 529–534
10. Daisne *et al.*, Tri-dimensional automatic segmentation of pet volumes based on measured source-to-background ratios: influence of reconstruction algorithms. Radiother Oncol **69** (2003) 247–250
11. Strauss *et al.*, The applications of pet in clinical oncology. J Nucl Med **32** (1991) 623–48; discussion 649–50

12. Ourselin *et al.*, Reconstructing a 3d structure from serial histological sections. Image and Vision Computing **19** (2001) 25 – 31
13. Wahl *et al.*, From recist to percist: Evolving considerations for pet response criteria in solid tumors. J Nucl Med **50 Suppl 1** (2009) 122S–150S
14. Hatt *et al.*, Impact of partial-volume effect correction on the predictive and prognostic value of baseline 18f-fdg pet images in esophageal cancer. J Nucl Med **53** (2012) 12–20
15. Yu *et al.*, Coregistered fdg pet/ct-based textural characterization of head and neck cancer for radiation treatment planning. IEEE Trans Med Imaging **28** (2009) 374–383
16. Naqa *et al.*, Chaudhari, S., Yang, D., Schmitt, M., Laforest, R., Thorstad, W., Deasy, J.O.: Exploring feature-based approaches in pet images for predicting cancer treatment outcomes. Pattern Recognit **42** (2009) 1162–1171
17. Hatt *et al.*, Baseline ^{18}f-fdg pet image-derived parameters for therapy response prediction in oesophageal cancer. Eur J Nucl Med Mol Imaging **38** (2011) 1595–1606
18. Haralick *et al.*, Textural features for image classification. **3** (1973) 610–621
19. Hatt *et al.*, metabolically active volumes automatic delineation methodologies in pet imaging: review and perspectives. Cancer Radiother **16** (2012) 70–81; quiz 82, 84
20. Miller *et al.*, Measurement of tumor volume by pet to evaluate prognosis in patients with advanced cervical cancer treated by radiation therapy. International Journal of Radiation Oncology*Biology*Physics **53** (2002) 353 – 359

Segmentation of pelvic structures from planning CT based on a statistical shape model with a multiscale edge detector and geometrical likelihood measures

Fabio Martinez[1,2,4], Oscar Acosta[1,2], Gaël Dréan[1,2], Antoine Simon[1,2], Pascal Haigron[1,2], Renaud de Crevoisier[1,2,3], and Eduardo Romero[4]

[1] INSERM, U 1099, Rennes, F-35000, France
[2] Université de Rennes 1, LTSI, F-35000, France
{Oscar.Acosta, Gael.Drean, Antoine.Simon, Pascal.Haigron}@univ-rennes1.fr
[3] Département de Radiothérapie, Centre Eugène Marquis, Rennes, F-35000, France
r.de-crevoisier@rennes.unicancer.fr
[4] CIM&Lab, Universidad Nacional de Colombia, Bogota, Colombia
{edromero, fmartinezc}@unal.edu.co

Abstract. Accurate segmentation of the prostate and the organs at risk in CT images is a crucial step in prostate cancer radiotherapy planning. Because of the poor soft tissue CT contrast (prostate, bladder), an appropriate segmentation is challenging, even when this is manually performed by an expert. This paper introduces a Bayesian automatic segmentation method for prostate, rectum and bladder in planning CT. Firstly, a prior shape space for the organs is built with PCA decomposition from a population of manually delineated CT images. Then, for a given CT to be segmented, the most similar shape is selected by the associated probability which is set by a likelihood function. Finally, the local shape is deformed to adjust the particular local edges of each organ such that the most likely segmentation is produced. Experiments with real data from 30 patients treated for prostate cancer radiotherapy were performed under a leave-one out cross validation scheme. Results show that the method produces reliable segmentations (Averaged Dice = 0.91 for prostate, 0.94 for bladder, 0.89 for Rectum) and outperforms the best majority-vote multi-atlas based approach.

1 Introduction

Prostate cancer (PC) is one of the most commonly diagnosed male cancer, with 190.000 new cases diagnosed in USA in 2010 (American Cancer Society) and 71.000 new cases in France in 2011 (INCa 2011). Radiation therapy is a commonly prescribed treatment for PC which has proven to be efficient for tumor control [1]. Modern prostate cancer radiotherapy involves an extensive use of X-ray imaging modalities: a computed tomography (CT) acquisition in the treatment planning and daily cone beam CT (CBCT) in image-guided radiotherapy procedures (IGRT). During the planning, CT images are manually processed to segment not only the clinical target (prostate and seminal vesicles) but also the neighboring organs at risks (OARs), namely the bladder, rectum, etc. These segmentations are crucial inputs for the treatment planning in order to compute the parameters for the accelerators following dose constraints to the target and OARs, and, considering IGRT, for the patient setup correction. Moreover, these segmentations

are up the most importance for other applications like the cumulated dose computation or toxicity studies on population [3].

Nowadays, the segmentations are manually carried out by medical experts. They are very time consuming and are prone to errors due to intra- and inter-experts variability. Thus, the need for automatic segmentation methods appears crucial for IGRT development. However, several difficulties arise and hamper automatic segmentation methods. The poor contrast appearing in similar soft tissues, has limited application of classical intensity-based methods, while the very high intra- and inter-individual variability has led model-based methods to fail. Some examples of previous methods to segment pelvic structures include deformable models [5,6]. Atlas-based segmentations [7] have also been used, but they have mainly been tested for segmenting CT scans in other applications such as head and neck [8] and cardiac aortic CT [9]. In atlas based approaches, precomputed segmentations in a template space are mapped to an individual CT using non-rigid registration. Although atlas-based approaches may provide prior structural information, the inter-individual variability and registration errors can mislead these methods. Multi-atlas approaches can partly overcome some of these difficulties by selecting the most similar atlases among a large database but the definition of a proper similarity measure between the available atlases and the query individual has still to be addressed [10].

We propose in this paper a method to segment pelvic structures from CT scans to be used in planning prostate cancer radiotherapy. The main contribution of this work is the adaptation of a Bayesian statistical framework to match a prior 3D shape model, built from a population, with the given CT through multi-scale edge observations. Regions of Interest (RoI's) are automatically extracted per slice to remove CT artifacts and compute the multiscale edge descriptor. The likelihood function is based on a geometrical shape characterization of edges using invariant Hu moments, allowing the selection of the most likely prior 3D shape to the multi-scale detected edges. In a final step, the obtained shape is locally warped to fit to the edges, yielding a 3D regular and compact organ segmentation. We compared our method with majority-vote multi-atlas strategies in a leave-one-out cross validation scheme.

2 Materials and Methods

The overall method is summarized in Figure 1. Let $\widehat{S_o}$, the estimated organ shape (prostate, bladder or rectum), computed as the most likely shape that maximizes the maximum a posteriori (MAP), following a Bayesian framework

$$\widehat{S_o} = \max_{\widehat{S_o}} \arg[P(\widehat{S_o}|S_{o_1}^{pca}, S_{o_2}^{pca}, \ldots, S_{o_N}^{pca})]$$

where $\{S_{o_1}^{pca}, S_{o_2}^{pca}, \ldots, S_{o_N}^{pca}\}$ is a collection of shapes (shape space) of the organ o precomputed with a Principal component analysis (PCA). The likelihood function aims to match the most similar shape to the borders extracted from a region of interest (RoI) automatically selected around the organ o. In order to remove CT artifacts, a pre-processing procedure is applied over the RoI. Afterward, a local deformation function is introduced to modify the most probable estimated shapes $\widehat{S_o}$, according to the local changes extracted from a multiscale edge descriptor. Each step is described in the following sections.

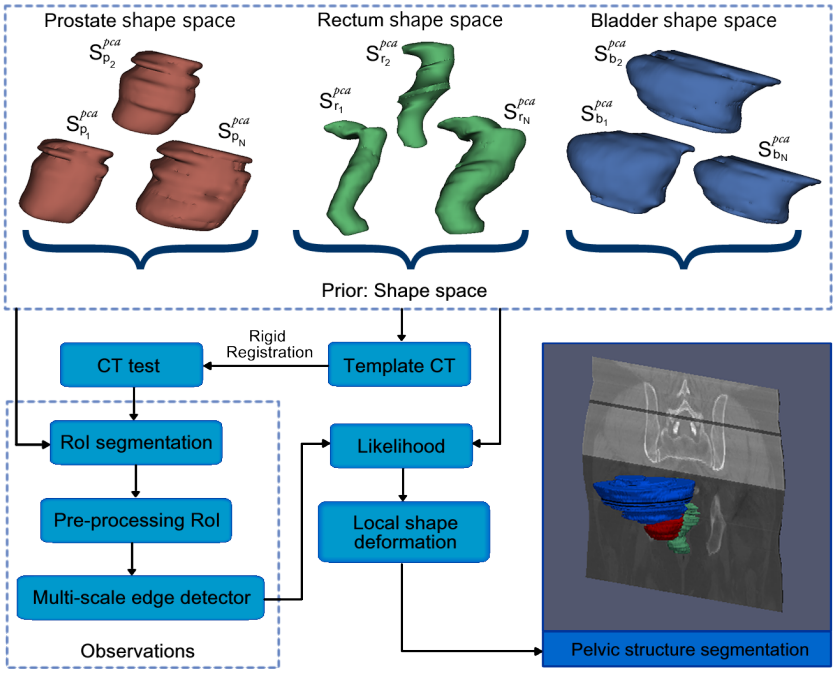

Fig. 1. Proposed method for 3D segmentation. First, a shape space organs is built (PCA). The template is rigidly registered to the CT to be segmented followed by an automatic extraction of RoIs for preprocessing and multi-scale edge detection. A likelihood function matches the most similar PCA shape with the detected edges to finally being locally adjusted.

2.1 Learning an organ shape model: the prior

A statistical shape organ model for segmentation is built from a collection of training samples as described in [11]. Here, a dimensionality reduction was firstly accomplished by applying the PCA method [12] to a population of manually delineated organs encoding interindividual shape variability [13]. From this PCA was computed the collection of shapes $\{S^{pca}_{o_1}, S^{pca}_{o_2}, \ldots, S^{pca}_{o_N}\}$, for each considered organ. Each shape contour is the parametric curve defined by the coordinates of the points lying on the contour. The first step consisted then in computing the first two moments of the probability distribution, i.e. the mean shape vector $\bar{s} \in R^{3M}$ and the covariance matrix $\rho \in R^{3Mx3M}$, as $\bar{s} = \frac{1}{N}\sum_{i=1}^{n} s_i$ and $\rho = \frac{1}{N-1}\sum_{i=1}^{n}(s_i - \bar{s})(s_i - \bar{s})^T$ where the vector $(s_i - \bar{s})$ describes the organ deviation w.r.t. the mean shape. The covariance matrix captures the organ variability. A conventional spectral analysis allows diagonalization of this covariance matrix that determines the directional gains or *eigenmodes*. Each eigenmode defines a 3D vector field of correlated organ inter patient-variability displacements. Thus, prostate and OAR samples are generated by deforming the mean shape by a weighted sum of the L dominating eigenmodes as:

$$S_{o_l}^{pca} = \bar{s} + \sum_{l=1}^{L} c_l q_l$$

where the coefficients of c_l follow a Gaussian distribution with the corresponding eigenvalues q_l as variances. This methodology was independently used for each organ, obtaining a family of shape models that are related with a template CT global coordinates. Examples of the different shapes obtained for each organ are shown in Figure 1.

2.2 RoI pre-processing

For a given CT, it is firstly rigidly registered with the template CT of the training database using a "block matching" method [14]. Over CT test is then defined a set of RoIs with size $\{\bar{S}_o \pm \xi\}$ associated to each organ, being $\bar{S}_o$ the average shape and ξ a tolerance value. An theoretical ideal $RoI_o(x, y)$ should contain the foreground organ of interest and a uniform background distribution, a particular configuration herein modeled as a mixture of Gaussians $\psi(i) = \sum_{k=1,2} w_k N(i|\mu_k, \sigma_k^2)$, where the two principal distributions represent the foreground and background, weighted by w_k. Because very often the selected RoIs contain other structures near the organs, difficulting a proper edge extraction of the organ and therefore biasing the statistical approximation, a more appropriate representation is found by filtering out RoI with an adapted non local mean. Thus, pixels i that may represent artifacts $\{i < \max_{k=1,2}(2\sigma_k) < i\}$ are replaced by a weighted average of a neighborhood with foreground/background information, thereby, satisfying a "non local property": weights depend on the pixel similarity in the image space, $\varrho(x, y) = e^{\frac{-d(x,y)}{h^2}}$. The basic idea is to replace the pixels that represent artifacts by the nearest "foreground/background" pixel that represent the neighborhood. $d(x, y) = \sum_{i \in \phi(o)} \left\| RoI_o(x, y) - N_{k1,k2}(\mu, \sigma^2) \right\|$, where $\phi(o)$ is a neighborhood of x an h is a decay parameter.

2.3 Multi-scale CT edge detector: the observations

To build a set of robust observations to be used within the likelihood function a multiscale description of RoI data was implemented. For doing so, each $RoI_o(x, y)$ was convolved several times with a gaussian kernel and first partial derivatives were calculated at the different resolution scales as:

$$S_o^{edge}(x, y; \sigma) = \sum_i RoI_o(x, y) * \frac{\partial G_{\sigma_i}}{\partial_x \partial_y}$$

where G_{σ_i} is the 2D Gaussian function with standard deviation σ_i. The Gaussian kernel is the unique kernel with an equivalent scale-space representation (linearity and shift-invariance in both frequency and space). Afterward, a non-maximum suppression is applied, aiming to detect points at which the gradient magnitude takes a maximum value in the gradient direction over all the scales [15]. This multi-scale edge detection allows a compact description of the most relevant information which is usually preserved through multiple scales (*the universal law of scale invariance*) [16].

2.4 Computing the likelihood

A likelihood function $P(\widehat{S}_{o_j}^{pca}|S_o^{edge})$ determines the best geometrical match between the samples shapes $\widehat{S}_{o_j}^{pca}$ obtained from the learned model and each multi scale edge descriptor S_o^{edge}. For doing so, every shape from the shape space and the edges in each RoI are characterized by a set of features based on the Hu moments [2], thereby achieving an invariant shape representation. Thus the likelihood function measures the shape similarity through an Euclidean metric among the computed features, written as:

$$P(S_{o_i}^{PCA}|S_{o_i}^{edge}) = \min_{S_{o_j}^{pca}} \left\{ \sum_{h_u(i=1...7)} \frac{||m_i^{S_o^{edge}} - m_i^{S_{o_j}^{pca}}||}{m_i^{S_o^{edge}}} \right\}$$

where $m_i^{S_o^{edge}} = sign(h_i^{S_o^{edge}}) \cdot \log|h_i^{S_o^{edge}}|$, and $m_i^{S_{o_j}^{pca}} = sign(h_i^{S_{o_j}^{pca}}) \cdot \log|h_i^{S_{o_j}^{pca}}|$ are the computed features for the edges and the PCA learned shapes respectively and $h_i^{S^{edge}}$, $h_i^{S_j^{pca}}$ are the Hu moments. Then, the likelihood function should yield a maximal probability when a sample learned shape closely match the observations, i.e., the multiscale edge descriptor.

2.5 Local Shape Deformation

A local deformation function was here introduced to improve the local correspondence of the shape sample selected by the PCA model with respect to near shape edges detected and allows to regularize the segmentation surface obtained. For doing this, the nearest borders that may correspond to the edges of the multiscale descriptor or the borders points of the shape sagittal estimation. Then the edges were warped toward the nearest border, controlling the deformation by a λ term, which works as a belief indicator warping the shape either to the border descriptor or to the PCA shape selected.

$$So_i(x,y) = \lambda \widehat{S}_{o_i}^{pca}(x,y) + (1-\lambda)(\min_{S_o}(\|\widehat{S}_{o_i}^{pca} - \{S_{o_i}^{edge}, \widehat{S}_{o_{i\pm1}}^{pca}\}\|))$$

This local deformation allows to preserve a compact representation of the shape given by the λ term and the nearest edge criterion. In this work, the best performance was obtained with a $\lambda = 0.6$

3 Evaluation and Results

We carried out a study on 30 prostate cancer patients, treated with external radiotherapy. Each individual underwent a planning CT. All acquired CT were 2 mm thickness slice with a 512x512x1 mm-pixels resolution in the axial plan. For each individual, the organs were manually delineated by the same expert, following the standard clinical protocol in prostate cancer radiotherapy. The expert contoured the clinical targets - namely the prostate and the seminal vesicles - and the organs at risk (OAR): the bladder and the rectum. In this study, only the CT and the delineated prostate, bladder and rectum were considered.

We aimed to compare individual's radiologist segmentations (ground truth) with the obtained by the proposed approach and those obtained with multi-atlas vote methods, on a set of 30 individuals, following a leave-one-out cross validation scheme. The

multi-atlas vote methods, used to evaluate the performance of the proposed approach, may be summarized in three main step. Firstly, the atlases rigidly registered using a "block matching" strategy were ranked according to the normalized cross-correlation (NCC) [14]. Secondly, the organs delineations were propagated into the individual's space, using a non-rigid registration, either the free-form deformation (FFD) [17], or the demons algorithm [18]. Eventually, the majority vote decision rule was applied to obtained a single segmentation for each considered organs.

Figure 2 illustrates a typical pelvic structures segmentation obtained by our approach (red contour) and the the radiologist reference represented by the green contour. These results shows the effectiveness obtained by our approach to closely adjust each organ structure. Likewise, it is shown a good local variability shape which preserve a compact representation, which means that, there are no strong spikes around the contour shapes.

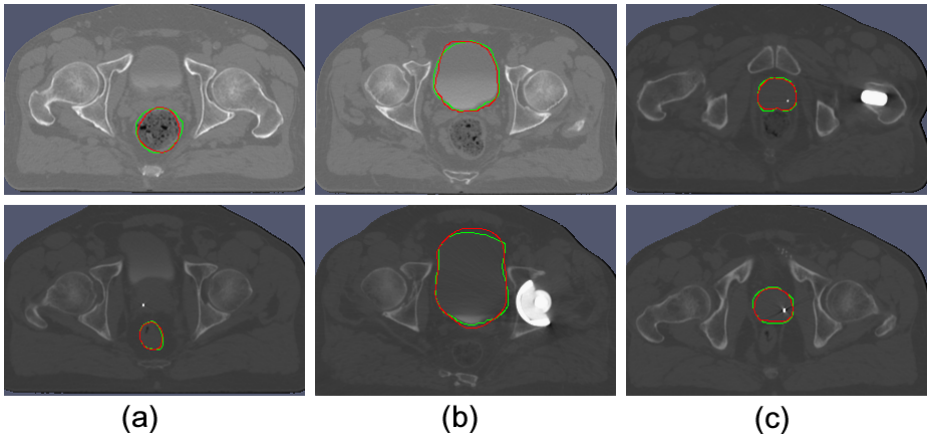

Fig. 2. Axial segmentation examples of pelvic structures ((a) rectum, (b) bladder and (c) prostate). The delineation obtained by our approach (red) and the expert reference (green).

A quantitative comparison was performed between the individual's organ delineations (prostate, bladder, rectum) and the computed segmentation using two different measures: a dice score (DSC) and the Hausdorff distance.

The DSC is an overlapping similarity measure defined as $DSC(A,B) = \frac{2|A \cap B|}{|A|+|B|}$, where $|\cdot|$ indicates the number of voxels of the considered A (gold standard) and B (method evaluated) volumes. We carried out an exploratory analysis of DSC obtained with the different segmentation strategies. Figure 3 illustrates the results comparing our approach with the atlas based methods. Results suggest that our method provide more accurate segmentations (t-test,$p<0.001$ for the prostate and the rectum) with an average score of 0.91 for prostate, 0.94 for bladder, 0.89 for Rectum

A second quantitative comparison was performed by computing the Hausdorff Distance. This metric identifies the segmentation voxel that is farthest from any voxel of the ground truth. Table 1 summarizes the performance obtained by the evaluated ap-

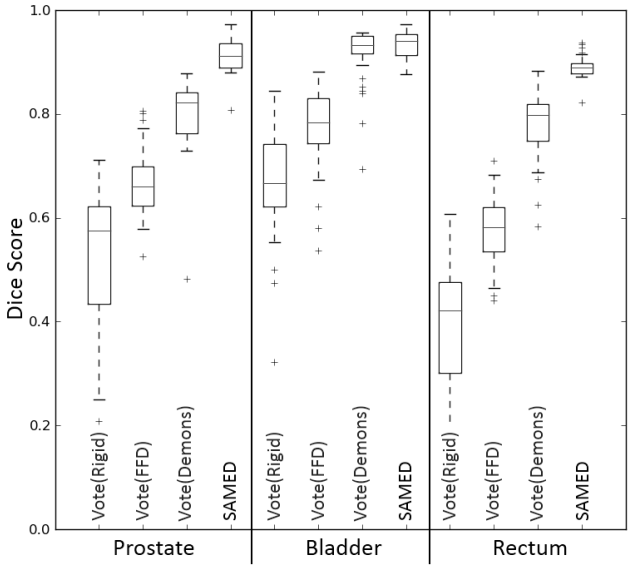

Fig. 3. Dice scores comparison for vote vs proposed approach (SAMED)

Table 1. The Hausdorff distances obtained with the multi-atlas majority-vote method using rigid, FFD or a demons registration and with the proposed approach (SAMED)

	Hausdorff Distance (mm)		
	Prostate	Bladder	Rectum
Vote(Rigid)	16.61±5.6	102.02±26	66.87±10.3
Vote(FFD)	14.27±4.2	78.63±20.1	65.22±6.1
Vote(Demons)	9.33±3.2	79.42±18.2	61.44±5.8
SAMED	5.98±2.2	19.09±3.1	7.52±2.3

proaches. The results shows that our approach obtain compact shape segmentations, with average distances of 5.98 for the prostate, 19.09 for the bladder and 7.52 for the rectum. The large distance of the multi-atlas based methods may be attributed to isolated voxels labeled as organ structure.

4 Conclusions

The proposed method introduces a new methodology to segment pelvic structures in CT scans used in prostate cancer radiotherapy. The Bayesian method combines a deformable prostate model, learned by examples, and a geometrical likelihood strategy that maps this model into a particular CT image, adequately described by a multiscale edge detector. The results summarized in this paper pointed out that our segmentation technique segment the prostate and rectum shape suitably in relation to radiologists' reference. This approach also may be extended to other structures over CT images. Future work includes validation with a large data set.

Acknowledgements

This work is partially supported by Rennes Metropole through a mobility scholarship, the project ANR TIGRE and the Universidad Nacional de Colombia Ph.D scholarship.

References

1. D'Amico, *et al*: Biochemical outcome after radical prostatectomy, external beam radiation therapy, or interstitial radiation therapy for clinically localized prostate cancer. AMA **280** (1998)
2. D. Zhang: Review of shape representation and description techniques. Pattern Recognition, 37(1):1-19, 2004.
3. Heemsbergen, W.D., *et al*: Urinary obstruction in prostate cancer patients from the dutch trial (68 gy vs. 78 gy): Relationships with local dose, acute effects, and baseline characteristics. Int J Radiat Oncol Biol Phys (2010)
4. Acosta, O.,*et al*: Atlas based segmentation and mapping of organs at risk from planning CT for the development of voxel-wise predictive models of toxicity in prostate radiotherapy. In:Prostate Cancer Imaging. International Workshop in MICCAI 2010. LNCS 6367. 42–51. (2010)
5. Costa, M.J., *et al*: Automatic segmentation of bladder and prostate using coupled 3D deformable models. Med Image Comput Comput Assist Interv **10** (2007) 252–260
6. D. Bystrov, *et al*: Simultaneous fully automatic segmentation of male pelvic risk structures. In: Estro. European society for Radioherapy and oncology. (2012)
7. Rohlfing, *et al*: Multi-classifier framework for atlas-based image segmentation. Computer Vision and Pattern Recognition, IEEE Computer Society Conference on **1** (2004) 255–260
8. Han, X., Hoogeman, *et al*: Atlas-based auto-segmentation of head and neck CT images. (2008) 434–441
9. Isgum, I., *et al*: Multi-atlas-based segmentation with local decision fusion - application to cardiac and aortic segmentation in CT scans. IEEE Transactions on Medical Imaging **28** (2009) 1000–1010
10. Acosta, O., *et al*: Evaluation of multi-atlas-based segmentation of ct scans in prostate cancer radiotherapy. IEEE ISBI. (2011) 1966 –1969
11. Heimann, T., Meinzer, H.P.: Statistical shape models for 3d medical image segmentation: A review. Medical Image Analysis **13** (2009) 543 – 563
12. Sohn, M., *et al*: Modelling individual geometric variation based on dominant eigenmodes of organ deformation: implementation and evaluation. Physics in Medicine and Biology **50** (2005) 5893
13. Lorenz, C.,*et al*: Generation of Point-Based 3D Statistical Shape Models for Anatomical Objects. CVIU **77** (2000) 175–191
14. Ourselin, S., *et al*: Reconstructing a 3D structure from serial histological sections. Image and Vision Computing **19** (2001) 25 – 31
15. Lindeberg, T.: Feature detection with automatic scale selection. Int. J. Comput. Vision **30** (1998) 79–116
16. Ter Haar Romeny,*et al*: Scale space: Its natural operators and differential invariants. In Colchester.: Information Processing in Medical Imaging. Springer Berlin / Heidelberg (1991) 239–255
17. Rueckert, D., *et al*: Nonrigid registration using free-form deformations: Application to breast mr images. IEEE Transactions on Medical Imaging **18** (1999) 712–721
18. Thirion, J.P.: Image matching as a diffusion process: an analogy with maxwell's demons. Medical Image Analysis **2** (1998) 243 – 260

VMAT inverse planning including DTI tractography fiber bundles as organs at risk: a feasibility study

Peroni M.[1,*], Patete P.[1], Ghielmetti F.[2,3],Casolino D.[1], Ongania E.[4], Casolino D.S.[4], Fariselli L.[3], Baroni G.[1,5]

[1]Department of Bioengineering, Politecnico di Milano, Milano, Italy
[2]Health Department and [3]Radiotherapy Unit Fondazione IRCCS Istituto Neurologico C. Besta, Milano, Italy
[4]Elekta AB, Stockholm, Sweden
[4]BioengineeringUnit, Centro Nazionale di Adroterapia Oncologica, Pavia, Italy

Abstract. The use of DTI tractography in radiosurgery and hypofractionated radiotherapy is still limited to visual inspection before planning to avoid tracts direct involvement. We propose to use the envelope of tractography fiber bundles as organs at risk, whose average dose shall be optimized during inverse planning. We show the benefit in terms of dose reduction, distribution homogeneity and target coverage in a feasibility study onto two glioma patients. The average dose at arcuate, corticospinal tract and corpus callosus was reduced respectively by 29%, 18% and 20% for patient 1 and 21%, 19% and 42% for patient 2. These promising preliminary results suggest that fiber bundles may be considered and preserved efficiently in radiation therapy treatment planning, allowing a potential increase of the total dose delivered to the target. The promising results prompt at integration also for benign and malignant small lesions treatment, where functional preservation is further critical.

Keywords: DTI, tractography, inverse planning, glioma

1 Introduction

Besides traditional anatomical Magnetic Resonance Imaging (MRI) sequences, functional MRI and Diffusion Tensor Imaging (DTI) offer a great potential to explore more complex functional and microscopic organization in the brain. DTI in particular allows the in-vivo visualization of the axonal organization of the white matter, exploiting the diffusion properties of water molecules [1-3]. Parameters like mean diffusivity and Fractional Anisotropy (FA) are commonly used as quantitative tools for differentiating the highly organized white matter from gray matter, as well as normal from pathological tissues [1,2] and for non-invasive pre-operative evaluation of tumor grade [4].

Based on the analysis of FA maps, water diffusion can be processed to reconstruct three-dimensional curves representing subcortical fiber tracts. This procedure, called

tractography, is based on mathematical algorithms that can be coarsely classified into deterministic and probabilistic approaches. Deterministic tractography methods rely on the assumption that, within a voxel, the orientation of the fibers is determined by the orientation of the main eigenvalue of the diffusion tensor [1,2,5]. This leads to anatomical reconstruction of the major white matter fibers, but its reliability is limited by image noise, distortions and fiber crossing [6]. To overcome deterministic approach limitations, probabilistic approaches have been proposed, in which a level of confidence is associated to each trajectory, starting from a set of seed points [1].

The largest field, where tractography is applied, is radiosurgery, in which a high radiation dose is delivered to the pathological tissue in one single treatment session. Koga et al [7] recently reported the outcomes of a prospective study on arteriovenous malformations in the brain in which DTI tractography was directly integrated into the Gamma-knife treatment planning workstation, with the long term goal of reducing radiation induced secondarisms and damages at cognitive areas, such as optic radiation, arcuate fasciculus and pyramidal and corticospinal tract. In [8-10], the authors estimated that the total dose tolerable by corticospinal tract is 2000cGy in a single Gamma-Knife radiosurgery session, while this value is reduced to 800cGy for the temporal fibers of arcuate fasciculus. The risk of steady sensory-motion decline is even higher if the selected treatment is radiotherapy and appears to be directly correlated with the field dimension. A preliminary study about the use of DTI in high-grade gliomas, conducted by Jena et al. [11], demonstrates the potentiality of using tractography in the personalization of treatment volumes according to tumor growth and infiltration grade. A major issue in all tractography works is represented by quantitative validation, since a real ground truth can be derived only from post-mortem histological slices. Anyway, some attempts have been made towards the objective evaluation of the tracts [12].

In the presented work, our goal is to use DTI deterministic tractography to define critical fiber bundles as organs at risk (OAR) in the inverse plan optimization of a Volumetric Modulated Arc Therapy (VMAT). We implemented a proof of concept study on two grade III glioma patients treated at the Fondazione IRCCS IstitutoNeurologico C. Besta (Milan, Italy) and demonstrated the feasibility of treatment arcs optimization in terms of total and mean dose at OARs, target coverage and homogeneity of dose distribution.

2 Materials and Methods

2.1 Dataset

Our retrospective study involves two grade III glioma patients (GS, m, 36 y, anaplastic oligoastrocytoma; SK, f, 38 y, anaplastic astrocytoma) who underwent anatomical MRI sequences (T1) for gross tumor volume (GTV) outline (with gadolinium contrast injection), DTI study for the surgical planning for tumor resection, and afterwards CT scan for the radiotherapy treatment planning and dose calculations. MRI sequences were acquired using a 1.5T SIEMENS Avanto scanner (SIEMENS HEALTHCARE, Erlangen, Germany). The MRI sequences were a morphological mprage T1 weighted

with resolution of 1x1x1mm, a DTI with 12 gradient directions EPI (echo Planar Imaging). DTI acquisition parameters were as follows: TE=92ms, TR=8.6s, voxel size =1x1x2 mm, 64 slices and b-value = 1000 s/mm^2. CT volumes were acquired using a Philips Brilliance scanner (Philips Healthcare, Eindhoven, the Netherlands) with 56 slices and a resolution of 0.9x0.9x3mm. Total planned dose for these patients was 5400 cGy, delivered in 200 cGy per fraction. For the purpose of this study, we simulated a VMAT hypofractionated treatment, for a total of 3000 cGy in 5 fractions.

2.2 Image pre-processing

For patient 1, DTI acquisition was performed 8 times, after which a mean volume was generated to enhance Signal to Noise Ratio (SNR). For patient 2, SNR was instead augmented by means of joint Rician filtering of each single diffusion direction.
Due to the different resolutions and reference frames of the acquired datasets, these were registered taking as reference the CT scan, as this is the core dataset for radiation therapy treatment planning and dose calculation. The registration of the DTI images on the CT was obtained by means of a three steps process. First of all the DTI gradients were registered on the *b=0* DTI volume (i.e. the images acquired with minimal diffusion weighting), to compensate for residual eddy currents and head motion. The obtained dataset was aligned to the corresponding anatomical MRI by means of an affine registration method based on normalized mutual information, using Slicer3D [13] routines. At the same time, we estimated the rigid transformation between anatomical MRI and CT, which we also applied to the aligned DTI volume.

2.3 Tractography algorithm

The corpus callosus, the corticospinal tract and the arcuate fasciculus ipsilateral to the neoplastic lesion were reconstructed using Slicer3D [13]. The chosen algorithm relies on a least-squares estimation of the diffusion tensor and on deterministic tracing of the fibers. The streamline path-integral deterministic algorithm at the basis of Slicer3D implementation was firstly described in [5] and solves the Frenet's equations using Runge-Kutta's numerical approximation.
To reconstruct the tracts of interest, we used a single ROI approach [14,15] based on existing anatomic knowledge about fiber bundles. This involved the help of expert neuro-radiologist and required the superimposition of T1 MRI and DTI tensor, whose dimensionality was reduced to a 3D volume condensing its information using a color map encoding for first eigenvector direction. The corpus callosus ROI was defined by contouring the fiber bundle on three sagittal slices into the hemisphere ipsilateral to the lesion. The corticospinal tract ROI seeding volumes were localized in three slices on the coronal view, where we contoured from the cerebral peduncle up to precentral gyrus. Arcuate fasciculus fibers originate in prefrontal and premotor gyri (part of the Broca's area) and project posteriorly to Wernicke's area, arching around the insula and putamen to run antero-inferiorly toward the temporal lobe. Arcuate ROI was individuated by successive approximation in axial and sagittal views at Wernicke's area level.

We used FA equal to 0.15 as stopping criteria for the estimation and 0.7°/mm as curvature escape condition, in an attempt of allowing a better estimation of fibers with large curvatures. We rejected fibers shorter than 10 mm and used voxel space for all calculations.

2.4 Post-processing and integration of tracts in the inverse treatment planning

The integration of reconstructed fibers in a radiation therapy treatment plan required the generation of appropriate 3D structures saved following the DICOM RT protocol. We designed and implemented a dedicated Qt- and VTK-based application, called fiberSlicer, to create the fiber bundles structure from the curves generated by Slicer3D and to extract their envelope contours, in order to create the required structures.
First of all, fiberSlicer approximates the single fiber with a tube of radius 0.75 times the CT pixel and central axis defined by the curve that identifies the fiber. The rendered bundle is cut according to each CT slice plane and the extracted object is triangulated using 2D Delaunay algorithm. The external contour on the cutting plane is than extracted and saved in DICOM RT format. The envelope contours may be saved separately or added to a previous DICOM RT file, to be easily imported by commercial workstations.
For the purpose of this preliminary study, we chose a commercial version of Elekta ERGO++(Elekta AB, Stockholm, Sweden), which supports Arc Modulation Optimization Algorithm (AMOA) inverse planning for VMAT treatments. With our approach, the fiber bundles can directly be assimilated to OARs and their minimum and maximum dose are used as constraints in AMOA fluence optimization. Besides fiber

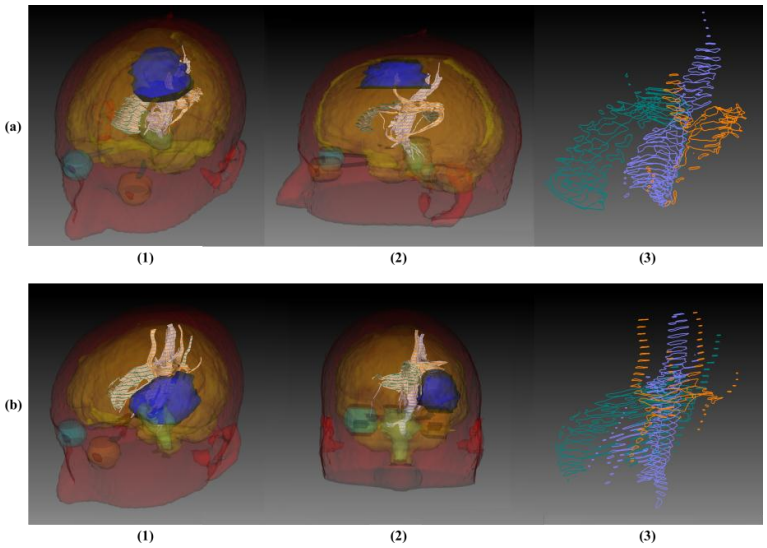

Fig.1. View of reconstructed fibers for patient 1 (a) and 2 (b) in fiberSlicer. Note the position of the fiber bundles with respect to the GTV (in solid blue). Panels (a.3) and (b.3) show the envelope of the reconstructed fascicles, which are used as OARs for dose inverse planning.

bundles, the attending physician contoured also other OARs, including brain, eyes, optical nerves, crystalline lenses, optical chiasm, and brainstem. As these structures were reasonably distant from the target, in this preliminary study, we did not introduce constraints on these OARs.
To quantify the potential benefits of including DTI tractography in radiation therapy planning, we performed an initial plan consisting of 94 beams divided into 5 arcs without any constraint on the fibers and subsequently an inverse planning including fiber bundles as OARs. The plans were compared in terms of Dose Volume Histogram (DVH) of both target and OARs, as well as in terms of cumulated dose at the fibers. Dose matrices calculations were performed on a 3mm grid for patient 1 and 2mm grid for patient 2.

2.5 Optimization procedure

Under the advice of the attending physicists, we decided to ignore corpus callosus in VMAT arcs optimization, under the hypothesis this structure being less critical. For both patients, the maximum dose at corticospinal tract and arcuate fasciculus was set at 800 cGy, applied to 70% and 60% volumes respectively (i.e. the constraint is applied to the volume fraction, while there is no control on the remaining part of the OAR structure). The penalty for the violation of these constraints was 10^4. For the chosen hypofractionated treatment, minimum and maximum dose constraints on the Gross Tumor Volume (GTV) were set at 95% (2850cGy) and 105%(3150cGy) of the total dose delivered. The penalties for these constraints were set respectively to 10^4 and $1.5 \cdot 10^4$, and the condition was restricted to the 98% of the GTV volume.

3 Results

3.1 Fiber bundles reconstruction and slicing

From the selected ROIs we were able to reconstruct anatomically reliable tracts.

Table1. Minimum, Maximum and Average Cumulative Dose before (rVMAT) and after (oVMAT) AMOA inverse planning for Gross Tumor Volume (GTV), Corpus Callosum (CC), Arcuate Fasciculus (AF) and CorticoSpinal Tract (CST).

	Organ	Minimum [cGy]		Maximum [cGy]		Average [cGy]	
	At Risk	rVMAT	oVMAT	rVMAT	oVMAT	rVMAT	oVMAT
Patient 1	**GTV**	2400	2370	3060	3030	2924	2922
	CC	240	210	1200	870	502	395
	AF	300	180	2970	3000	1014	720
	CST	090	060	2910	2880	1000	819
Patient 2	**GTV**	2010	1680	3060	3120	2913	2900
	CC	330	180	2880	2880	906	527
	AF	120	90	2970	2970	1551	1223
	CST	120	120	2970	2880	1480	1203

Figure 1 shows the obtained bundles for patient 1 and 2 in panels a and b respectively. In patient 1, corticospinal tract was entering directly into lesion volume and, as such, this tract is very likely to be compromised by radiation. Corpus callosus and arcuate fasciculus are also located in the immediate proximity to the tumor. Patient 2 tracts were reconstructed less accurately (Figure 1b). In particular, arcuate fasciculus integrity was compromised by the massive lesion and therefore lost the typical arch. In figure 1 (Panels a.3 and b.3), note also the color envelope superimposed onto the tube dilation of the fiber axes and that the different fiber bundles were kept separated in the attempt of differentiating tracts involvement in the treatment.

3.2 Dosimetric evaluation

DVHs of cumulative dose obtained from VMAT without any dose optimization (rVMAT) are presented in Figure 2a and 2c for patient 1 and 2 respectively. In panels b and d, we show the distribution obtained after inverse planning (oVMAT) with constraints on GTV, arcuate and corticospinal tracts only. We note that the coverage of the GTV is maintained also in b and d, whilst a better sparing of both arcuate fasciculus and corticospinal tract is possible. Despite not setting any constraint on corpus callosus, its final dose distribution is improved after optimization.
Cumulative average, maximum and minimum dose at GTV, corpus callosus, arcuate fasciculus and corticospinal tract is also reported in Table 1. For patient 2, the optimized distribution loses in conformity in particular at lower dose grades, while for patient 1 the 95% isodose distribution is very similar to pre-inverse planning one.
We were able to further optimize patient 1 distribution, changing dose constraint on the fiber bundles. The new maximum dose was chosen as the one at 50% volume after first optimization, but it was applied to the volume used in the first optimization run (600 cGy on 60% of the volume and 500 cGy on 70% of the volume for arcuate and corticospinal tracts respectively). Average dose dropped in this case to 571 cGy, 716 cGy and 264 cGy for arcuate, corticospinal and corpus callosus respectively, while GTV mean dose remains at 2914 cGy. The GTV distribution was still homogeneous enough to consider this further optimization suitable for the clinic.

4 Discussion and conclusion

In this feasibility study, we propose to directly incorporate DTI tractography reconstructed fiber bundles into AMOA inverse planning for VMAT hypofractionated treatment. We performed tractography of corticospinal tract, arcuate fasciculus and corpus callosum in the hemisphere ipsilateral to grade III glioma lesion. Tractography quality was visually inspected by the attending physicians and physicists, but more quantitative validation shall be performed in future studies. The error induced by tumor proximity to the tracts as well as by the edema surrounding the neoplastic lesion reflected on tractography quality, as previously shown in terms of FA values by [16]. In particular, patient 2 lesion severely dislocated and interrupted the arcuate fasciculus in the medial region.

Despite the need for further refinement and quantitative validation of fiber bundles, we were able to integrate all tracts into the treatment planning after calculating their envelope with an *adhoc* developed software called fiberSlicer. The smoothness and continuity of the contours was guaranteed by Delaunay triangulation of the sliced surfaces. Therefore, the treatment planning system handled the fiber bundles exactly as all other manually contoured structures.

Considering the fiber bundles in the plan optimization, we were able to strongly reduce the dose delivered to the corticospinal and arcuate tracts, while the optimized target DVH remain mostly unchanged. On the other side, the non-significant difference in the maximum total dose at fibers is due to the fact that the fiber bundles projected inside the GTV, but the shape of their DVH curves after optimization tends to be similar to the typical OAR ones. Further forcing of the maximum dose constraint might prevent optimization convergence and/or escalate dose distribution inhomogeneity. The average dose at arcuate, corticospinal tract and corpus callosus was reduced respectively by 29%, 18% and 20% for patient 1 and 21%, 19% and 42% for patient 2, confirming that this method has the potential to be applicable for planning, enhancing fiber bundles sparing and possibly enhancing functionality preservation.

Future work will be dedicated to enlarge patient database and adding specific dose constraints for all the organs at risk and running a more complex inverse planning. In addition, the promising results underlined by our feasibility study will be extended to high precision treatments (e.g. Cyberknife) of small lesions (benign and malignant) in

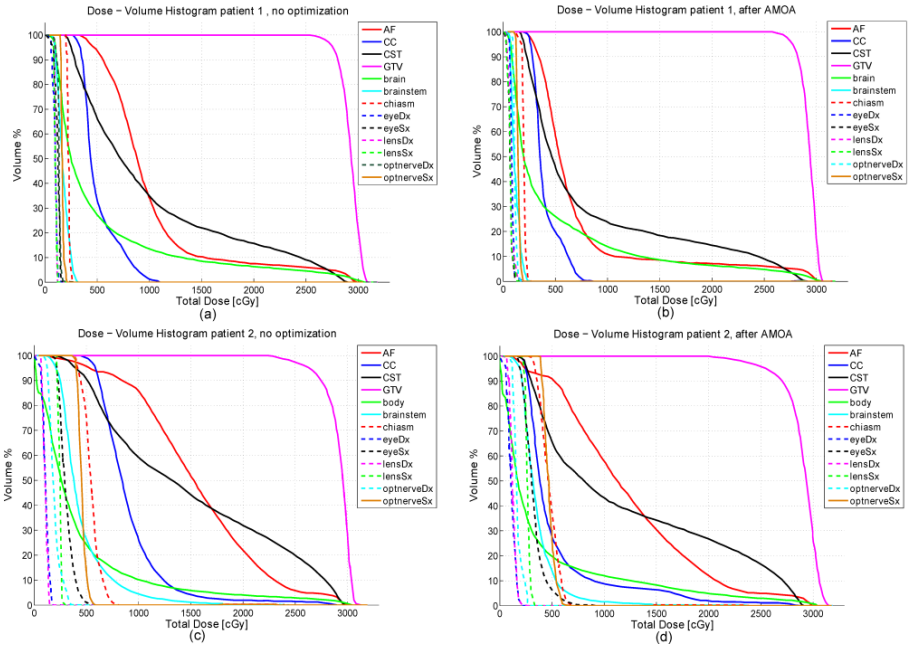

Fig.2. Dose Volume Histogram (DVH) comparison for patient 1 (a,b) and 2 (c,d). Panels a and c show DVHs of both GTV and OARs before inverse planning optimization, while b and d report the results after optimization. Note that in b and d dose of fiber bundles is lower than in the non-optimized version, despite the constant GTV coverage.

critical functional areas.

5 Bibliography

1. Yamada K., Sakai K., Akazawa K., Yuen S., Nishimura T. MR tractography: a review of its clinical applications. Magnetic resonance in medical sciences MRMS an official journal of Japan Society of Magnetic Resonance in Medicine 8, 165-74 (2009).
2. Masutani Y., Aoki S., Abe O., Hayashi N., Otomo K., MR diffusion tensor imaging: recent advance and new techniques for diffusion tensor visualization, European Journal of Radiology, 46(1): 53-66, (2003)
3. Le Bihan D, Mangin JF, Poupon C, Clark CA, Pappata S, Molko N, Chabriat H., Diffusion tensor imaging: concepts and applications., J Magn Reson Imaging., Apr;13(4):534-46 (2001)
4. Inoue T., Ogasawara K., Beppu T., Ogawa A., Kabasawa H., Diffusion tensor imaging for preoperative evaluation of tumor grade in gliomas, Clinical Neurology and Neurosurgery, Apr; 107(3): 174-180 (2005).
5. Basser PJ, Pajevic S, Pierpaoli C, Duda J, Aldroubi A., In vivo fiber tractography using DT-MRI data., Magn Reson Med. Oct;44(4):625-32 (2000).
6. Chung HW, Chou MC, Chen CY., Principles and limitations of computational algorithms in clinical diffusion tensor MR tractography.,AJNR Am J Neuroradiol., Jan;32(1):3-13. (2011).
7. Koga, T. et al. Outcomes of diffusion tensor tractography-integrated stereotactic radiosurgery. International Journal of Radiation Oncology, Biology, Physics 82, 799-802 (2012).
8. Maruyama K, Kamada K, Shin M, Itoh D, Aoki S, Masutani Y, Tago M, Kirino T., Integration of three-dimensional corticospinal tractography into treatment planning for gamma knife surgery., J Neurosurg. Apr;102(4):673-7. (2005)
9. Maruyama K, Koga T, Kamada K, Ota T, Itoh D, Ino K, Igaki H, Aoki S, Masutani Y, Shin M, Saito N., Arcuate fasciculus tractography integrated into Gamma Knife surgery., J Neurosurg. Sep;111(3):520-6.(2009)
10. Maruyama K, Shin M, Tago M, Kurita H, Kawamoto S, Morita A, Kirino T., Gamma knife surgery for arteriovenous malformations involving the corpus callosum.J Neurosurg. Jan;102 Suppl:49-52. (2005)
11. Jena R, Price SJ, Baker C, Jefferies SJ, Pickard JD, Gillard JH, Burnet NG., Diffusion tensor imaging: possible implications for radiotherapy treatment planning of patients with high-grade glioma., Clin Oncol , Dec;17(8):581-90.(2005)
12. Wang JY, Abdi H, Bakhadirov K, Diaz-Arrastia R, Devous MD Sr., A comprehensive reliability assessment of quantitative diffusion tensor tractography.Neuroimage. Apr 2;60(2):1127-38 (2012).
13. Pieper S., Lorensen B., Schroeder W., Kikinis R., The NA-MIC Kit: ITK, VTK, Pipelines, Grids and 3D Slicer as an Open Platform for the Medical Image Computing Community., Proceedings of the 3rd IEEE International Symposium on Biomedical Imaging: From Nano to Macro 2006; 1:698-701 (2006).
14. Wakana S, Jiang H, Nagae-Poetscher LM, van Zijl PC, Mori S., Fiber tract-based atlas of human white matter anatomy., Radiology. Jan;230(1):77-87 (2002).
15. Catani M, Howard RJ, Pajevic S, Jones DK., Virtual in vivo interactive dissection of white matter fasciculi in the human brain., Neuroimage. Sep;17(1):77-94 (2002).
16. Yen PS, Teo BT, Chiu CH, Chen SC, Chiu TL, Su CF., White Matter tract involvement in brain tumors: a diffusion tensor imaging analysis., Surg Neurol. Nov;72(5):464-9; (2009).

A Diffeomorphic MLR Framework for Surrogate-based Motion Estimation and Situation-adapted Dose Accumulation

René Werner, Matthias Wilms, Jan Ehrhardt,
Alexander Schmidt-Richberg, Maximilian Blendowski, and Heinz Handels

Institute of Medical Informatics, University of Lübeck
Ratzeburger Allee 160, 23538 Lübeck, Germany
werner@imi.uni-luebeck.de

Abstract. Respiratory motion a is major source of uncertainty in radiotherapy. Current approaches to cope with it – like gating or tracking techniques – usually make use of external breathing signals, interpreted as surrogates of internal motion patterns. Due to the complex nature of internal motion, a trend exists toward the application of multi-dimensional surrogates. This requires the development and evaluation of appropriate correspondence models between the surrogate data and internal motion patterns. We suggest using a multi-linear regression (MLR) and exploit the Log-Euclidean Framework to embed the MLR within a correspondence model yielding diffeomorphic estimates of motion fields of internal structures. The framework is evaluated using 4D CT data of lung tumor patients and different surrogates (spirometry, diaphragm tracking, monitoring chest wall motion). Further, the application of the framework for incorporating surrogate-based information about breathing variations into the process of dose accumulation is illustrated.

Keywords: radiation therapy, breathing signals, motion estimation, multivariate statistics, diffeomorphic registration, Log-Euclidean framework

1 Introduction

Respiratory motion is a major source of error in conventional radiation therapy (RT) of thoracic and abdominal tumors. Current approaches to cope with it usually rely on the use of external breathing signals that are easy and fast to acquire. This holds on the one hand for 4D CT imaging, during which image or projection data are sorted ("binned") to different breathing states based on breathing signals like spirometry records or abdominal belt measurements; for dose delivery, on the other hand, analogue technical devices are reported to be used to steer gated dose delivery or tumor tracking techniques [1, 2].
These breathing signals usually provide only a surrogate of the object of interest, which is the respiratory motion of internal structures (tumor/clinical target, organs at risk); they are therefore also referred to as surrogates (of the internal motion). Due to the three-dimensional nature of internal motion patterns, intra-

and inter-cycle motion variability like, e.g., phase shifts between movements of different structures, the reliability of simple one-dimensional breathing signals is, however, more and more considered to be problematic, and a trend toward the use of multi-dimensional surrogates can be observed [3]. This requires the development and evaluation of correspondence models between the breathing signals and internal motion patterns that especially take advantage of the multi-dimensional structure of the surrogates.
The use of multi-dimensional signals and the complexity of motion patterns of internal structures, usually described by non-linear transformations or displacement fields, naturally suggests the use of multi-variate statistics. A straightforward approach for defining a correspondence model would therefore be a multi-linear regression (MLR); a patient-specific correspondence between surrogate data and internal motion patterns could then be trained using, e.g., a 4D CT image sequence of the patient and information about internal motion extracted from them on the one hand and surrogate measurements corresponding to the individual image frames on the other hand. In this case, the needed representation of the internal motion information would usually be given by transformations or displacement fields estimated by non-linear registration of the image frames of the 4D CT data [4].
In the context of motion estimation of internal structures it is, however, considered to be a natural choice to restrict the transformations to diffeomorphisms, as these ensure that "connected sets remain connected, disjoint sets remain disjoint, smoothness of anatomical features [...] is preserved, and coordinates are transformed consistently" [5]. This cannot be guaranteed when applying a standard MLR correspondence model – neither for interpolating internal motion fields from a surrogate measurement being in the range of the surrogate data available for the MLR training phase, nor for extrapolation purposes. Now, being placed in that context, the motivation of our contribution is three-fold. First, we propose to exploit the Log-Euclidean framework, which in the last years has been proven to be an efficient way for performing statistics on diffeomorphic transformation [6, 7], for definition of a diffeomorphic MLR-based correspondence model. Second, we present a first evaluation of the diffeomorphic MLR framework, including a comparison of the capabilities of three different but typical types of breathing signals when applied as regressors/surrogates: spirometry, tracking the motion of the diaphragm, and tracking chest wall motion. Third, we demonstrate the use of such a framework in the context of 4D dose calculation. The last part aims at incorporation of information about motion variations as provided by breathing signals into the process of dose accumulation during RT treatment planning.

2 Theoretical Background

During definition of the MLR-based correspondence model we assume the patient's anatomy to be represented by a 4D CT image sequence $(I_j)_{j\in\{1,\ldots,n_{ph}\}}$, $I_j : \Omega \subset \mathbb{R}^3 \rightarrow \mathbb{R}$, with j denoting the breathing states. Designating w.l.o.g. the state $j = 1$ as a reference breathing state, the motion of the anatomical and patholog-

ical structures will then be described by transformations $\varphi_j = id + u_j : \Omega \to \Omega$, which – in the sense of image registration – maximize similarity/minimize dissimilarity of I_1 and $(I_j \circ \varphi_j)$ with respect to additional smoothness requirements for the transformations. Being interested in a general diffeomorphic motion estimation framework, we choose a diffeomorphic registration scheme to compute the transformations φ_j; the scheme is described in Section 2.1. Following, the theory behind the MLR framework is explained in Section 2.2. Finally, in Section 2.3, the integration of the MLR-based correspondence model into the process of dose accumulation is detailed.

2.1 Diffeomorphic Registration and the Log-Euclidean Framework

Diffeomorphic transformations can be modeled as endpoints of the evolution equation over unit time $t \in [0, 1]$,

$$\frac{\partial}{\partial t}\phi_t(x) = v(\phi_t(x), t) \quad \text{with} \quad \phi_0(x) = x, \tag{1}$$

with $v : \Omega \times [0, 1] \to \mathbb{R}^3$ being sufficiently smooth velocity fields parameterizing the flow $\phi : \Omega \times [0, 1] \to \Omega$. Thus, a diffeomorphic transformation $\varphi : \Omega \to \Omega$ can be computed by

$$\varphi(x) = \phi_1(x) = \phi_0(x, 0) + \int_0^1 v(\phi_t(x), t)\, dt \tag{2}$$

[8]. The time-dependence of the velocity fields leads, however, to time and memory consuming algorithms in the context of image registration [5]. To avoid these problems, stationary velocity fields can be considered instead. Then, as part of the Log-Euclidean Framework, it can be exploited that the set of diffeomorphisms $\mathrm{Diff}(\Omega)$, together with the function composition, exhibits a Lie group structure. For a diffeomorphism parameterized by a stationary velocity field v, v is part of the tangential space $\mathcal{T}_{\mathrm{id}}\mathrm{Diff}(\Omega)$ at the neutral element of $\mathrm{Diff}(\Omega)$ [6]. Further, $\mathcal{T}_{\mathrm{id}}\mathrm{Diff}(\Omega)$ and $\mathrm{Diff}(\Omega)$ are connected by the so-called group exponential $\exp : \mathcal{T}_{\mathrm{id}}\mathrm{Diff}(\Omega) \to \mathrm{Diff}(\Omega)$, with the paths $\phi_t = \exp(tv)$ being one parameter subgroups of $\mathrm{Diff}(\Omega)$. Based thereon, Arsigny et al. proposed to rephrase the transformation of (2) by

$$\varphi(x) = \phi_1(x) = \exp(v(x)), \tag{3}$$

with the group exponential being efficiently computed using the scaling-and-squaring algorithm [6].
The parameterization (3) also states the basis of the PDE-driven non-linear registration framework applied in the work at hand to compute the sought transformations φ_j describing the respiratory motion of internal structures in the 4D image sequences. Let therefore I_1 serve as reference image and I_j with j being an arbitrary breathing state denoting the target image, we search for the transformation $\varphi_j = \exp(v_j)$ that minimizes the energy functional

$$\mathcal{J}[v_j] = \mathcal{D}[I_1, I_j \circ \varphi_j] + \alpha \mathcal{S}[v_j]; \tag{4}$$

$\mathcal{D}$ represents a dissimilarity measure and $\mathcal{S}$ a smoothness term/regularizer. The Euler Lagrange equations can then be formulated as

$$f\left(x, \varphi_j\left(x\right)\right) + \alpha \mathcal{A}[v_j]\left(x\right) = 0, \quad x \in \Omega, \tag{5}$$

with f being a force-term corresponding to the dissimilarity measure and $\mathcal{A}$ as a linear differential operator associated to $\mathcal{S}$. Here, a diffusion regularization approach (i.e. $\mathcal{A} = \Delta$) and the so-called active Thirion forces, also referred to as normalized SSD forces, are applied; for details see, e.g., [9].

2.2 Multi-linear Regression for Surrogate-based Motion Estimation

With the transformations $(\varphi_j)_{j\in\{1,\ldots,n_{ph}\}}$ and velocity fields $(v_j)_{j\in\{1,\ldots,n_{ph}\}}$ being computed by diffeomorphic registration, we further assume that surrogate measurements $(\xi_j)_{j\in\{1,\ldots,n_{ph}\}}$, $\xi_j \in \mathbb{R}^{n_{sur}}$ have been acquired simultaneously to the CT image data (or subsequently simulated). Then, the idea of the diffeomorphic MLR-based correspondence model is to apply a regression to estimate the relationship between the surrogate-signals ξ_j (regressors) and the velocity fields v_j (regressands) instead of the motion fields u_j or transformations φ_j. Interpret the velocity fields v_j and the surrogate data ξ_j as random variables $\mathbf{V}_j$ and $\mathbf{Z}_j$, for which the motion information is written in a single column. Let the individual random variables further be combined within the matrices $\mathbf{V} := (\mathbf{V}_1^c, \ldots, \mathbf{V}_{n_{ph}}^c)$ and $\mathbf{Z} := (\mathbf{Z}_1^c, \ldots, \mathbf{Z}_{n_{ph}}^c)$ with $\mathbf{V}_j^c = \mathbf{V}_j - \bar{\mathbf{V}}$ and $\mathbf{Z}_j^c = \mathbf{Z}_j - \bar{\mathbf{Z}}$ as the centered versions of $\mathbf{V}_j$ and $\mathbf{Z}_j$. The multi-variate multi-linear regression can then be phrased as the estimation of the relationship

$$\mathbf{V} = \mathbf{B}\mathbf{Z} \tag{6}$$

by

$$\mathbf{B} = \arg\min_{\mathbf{B}'} \operatorname{tr}\left[\left(\mathbf{V} - \mathbf{B}'\mathbf{Z}\right)\left(\mathbf{V} - \mathbf{B}'\mathbf{Z}\right)^T\right] = \mathbf{V}\mathbf{Z}^T\left(\mathbf{Z}\mathbf{Z}^T\right)^{-1}. \tag{7}$$

Thus, $\mathbf{B}$ represents an ordinary least squares (OLS) estimator between the surrogate data $\xi_j \equiv \mathbf{Z}_j$ and the velocity fields v_j and $\mathbf{V}_j$, respectively.
With the OLS estimator $\mathbf{B}$ computed, for any measurement $\hat{\xi} \equiv \hat{\mathbf{Z}}$ a corresponding velocity field $\hat{v}$ can be derived by $\hat{\mathbf{V}} = \bar{\mathbf{V}} + \mathbf{B}\left(\hat{\mathbf{Z}} - \bar{\mathbf{Z}}\right)$ and resorting the entries of $\hat{\mathbf{V}}$ wrt. the structure of $\hat{v}$. Exploiting the Log-Euclidean framework, the sought diffeomorphic transformation is finally to be calculated by $\hat{\varphi} = \exp\left(\hat{v}_j\right)$.

2.3 Application of the MLR-based Correspondence Model to Situation-adapted Dose Accumulation

In the context of 4D dose calculation, dose accumulation aims at assessing dosimetric effects of respiratory motion for a generated (3D) treatment plan. Given a

4D image sequence $(I_j)_{j\in\{1,\ldots,n_{ph}\}}$ of the patient, a standard dose accumulation for voxels $x \in \Omega$ of the reference image reads

$$D^{4D}(x) = \sum_{j=1}^{n_{ph}} w_j \left(D_j \circ \varphi_j\right)(x) \tag{8}$$

with $D^{4D} : \Omega \to \mathbb{R}_+$ being the sought accumulated dose; in that, the dose contributions $D_j : \Omega \to \mathbb{R}_+$ (3D dose calculated as resulting for the given treatment plan and the CT image I_j) are often equally weighted, i.e. $w_j = 1/n_{ph}$.
It is obvious that neither motion variations nor effects due to the interplay of organ motion and short delivery times of single irradiation fields can be assessed by (8) [10]. Thus, going one step further toward accurate dose accumulation, in this contribution we propose to start the dose accumulation process with a patient-specific surrogate signal measurement and the corresponding OLS estimator $\mathbf{B}$ as computed by (7). Additionally, we assume the beginning time and the duration of each irradiation field of the treatment plan to be known and denoted by $t_{k,0}$ and $t_{k,end}$ $(k = 1, \ldots, n_{fields})$. Then, instead of a weighted summation over the dose distributions D_j, we now sample the surrogate signal equidistantly in time and rephrase the dose accumulation problem as follows:

$$\begin{aligned} D^{4D}(x) &= \sum_{k=1}^{n_{fields}} \int_{t_{k,0}}^{t_{k,end}} \dot{D}_k\left(x(t), t\right) dt \\ &\approx \sum_{k=1}^{n_{fields}} \sum_{l} \dot{D}_k\left(\hat{\varphi}_l(x), t_l\right) \Delta t \\ &\approx \sum_{k=1}^{n_{fields}} \frac{\Delta t}{t_{k,end} - t_{k,0}} \sum_{l} D_k\left(\hat{\varphi}_l(x), t_l\right). \end{aligned} \tag{9}$$

$\dot{D}_k\left(\hat{\varphi}_l(x), t_l\right)$ is the dose rate for field k at time t_l belonging to the sampling point l, which is evaluated at the position of voxel $x \in \Omega$ of the reference CT at time t_l; $D_k\left(\hat{\varphi}_l(x), t_l\right)$ is the corresponding dose with $\hat{\varphi}_l$ being estimated based on the surrogate measurement at t_l and the OLS estimator $\mathbf{B}$ (cf. Section 2.2).

3 Experiments and Results

Our experiments were based on 4D CT images of 10 lung tumor patients (10-14 breathing states, spatial resolution 320×320×270 voxels with an isotropic spacing of 1.5 mm). The image binning was grounded on spirometry records, which were also considered as a first example of a (one-dimensional) breathing surrogate during evaluation of the MLR correspondence model. For evaluation purposes we further identified the domes of the left and the right hemi-diaphragm and interpreted the corresponding displacements $\left\{u_1\left(x^{\mathrm{dia}}\right), \ldots, u_{n_{\mathrm{ph}}}\left(x^{\mathrm{dia}}\right)\right\}$ as a second type of surrogate measurements ($n_{sur} = 2{\cdot}3$). As a third type of breathing signal we simulated a laser-based tracking of lifting/raising of chest wall points within

Table 1. Landmark-based target registration errors and tumor propagation errors (evaluated based on the tumors' centers of mass, COM), obtained for the diffeomorphic MLR-based estimation of inner lung motion as part of the leave-out tests and listed for the different surrogate types (mean± standard deviation for the ten patients considered; EE/ME = end-/mid-expiration, EI/MI = end-/mid-inspiration).

	Landmark-based Target-Registration-Error [mm]			**Tumor COM distance [mm]**
Motion Estimation	**EI → EE**	**EI → MI**	**EI → ME**	**EI → EE**
No motion estimation	6.8 ± 1.8	4.9 ± 1.2	2.5 ± 0.6	6.9 ± 6.1
Intra-patient registration	1.6 ± 0.2	1.6 ± 0.1	1.5 ± 0.2	0.9 ± 0.5
Diffeomorphic MLR framework; surrogate = ...				
spirometry	2.0 ± 0.3	2.0 ± 0.3	1.8 ± 0.3	1.5 ± 0.9
diaphragm motion	2.1 ± 0.4	1.8 ± 0.2	1.7 ± 0.3	1.7 ± 0.9
chest wall motion, sternum	4.7 ± 1.4	2.6 ± 0.9	2.4 ± 0.7	4.7 ± 4.3
chest wall motion, line	2.1 ± 0.4	1.9 ± 0.2	1.8 ± 0.2	1.4 ± 1.0

the 4D CT images by a ray tracing approach (ray direction: anterior-posterior). In a first run, a point laser was simulated with the laser origin placed over the sternum; in the second run, we used several (≈ 150) points lying on line (direction: superior-inferior), aiming at simulating the use of a line laser. For each surrogate and the state of end-inspiration (EI) as reference state, we evaluated the accuracy of the MLR correspondence models in leave-out tests. For evaluating "extrapolation" capabilities, all breathing states but the states of and around end-expiration (EE), i.e. in total $(n_{ph} - 3)$ states, are used for training the OLS estimators; the surrogate values ξ_{EE} were then applied to estimate the transformation $\hat{\varphi}_{EE}$. The accuracy of the motion estimation was evaluated by determining a target registration error based on manually defined corresponding landmarks (70 landmarks per patient and breathing phase). Additionally, the accuracy of a model-based tumor segmentation propagation between EI and EE was quantified considering manual tumor segmentations as ground truth data. Interpolation capabilities were analogously analyzed for motion estimation between EI and mid-inspiration (MI) and mid-expiration (ME).

The corresponding results are listed in Table 1. Referring to the accuracy of the breathing surrogates, no significant differences can be observed between spirometry, tracking diaphragm motion, and combining motion information of several chest wall points (i.e. simulating the line laser). In comparison thereto, the accuracy is significantly decreased when tracking the raising/lifting of only a single chest wall point (here: the sternum); this demonstrates the potential of combining motion information at least for tracking chest wall motion. The values listed in Table 1 were further compared with analogous results obtained by a standard non-diffeomorphic MLR framework (i.e. modeling correspondences directly between the motion fields u_j and the surrogate data ξ_j). It turned out that no significant differences were apparent wrt. the accuracy of the motion estima-

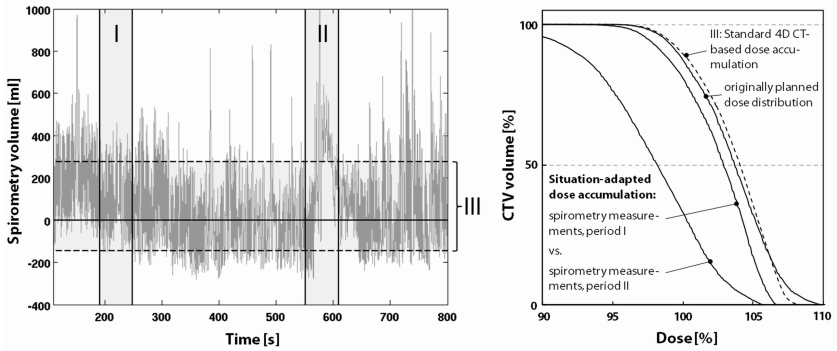

Fig. 1. Illustration of differences between the MLR-based situation-adapted and standard dose accumulation results. Left: spirometry record, acquired during 4D CT image acquisition. The interval III denotes the spirometry values represented by the 4D CT data. The periods I and II are the intervals considered for demonstration of the situation-adapted dose accumulation. Right: dose-volume-histograms for the dose accumulation approaches and the clinical target volume CTV.

tion. However, especially in the case of extrapolation, the motion fields obtained by non-diffeomorphic correspondence models featured a series of singularities – which were not existing for the diffeomorphic framework.

To further demonstrate the application of the diffeomorphic MLR-based correspondence model for dose accumulation purposes, a 3D IMRT treatment plan was generated for a patient with a clinically relevant tumor motion amplitude of 12 mm (10 mm isotropic margin between clinical and planning target volume CTV and PTV; planning phase: MI; treatment planning system: CMS XiO v.4.3.3). Accumulated dose distributions were computed using standard dose accumulation according to (8) and applying the surrogate-based accumulation scheme as derived in (9). The surrogate-based dose accumulation was based on the spirometry data recorded during the 4D CT image acquisition, see Figure 1 (left); we selected both a period of the record with little variance of the distribution of the local maxima (dose accumulation for a "regular breathing situation"; period I in the figure) and a period of high variance of the local maxima ("irregular breathing situation", period II).

The dose-volume-histograms for the CTV and the different dose distributions are shown in Figure 1 (right). It becomes obvious that standard dose accumulation based on only the 4D CT image information underestimates the risk of CTV underdosages due to respiratory motion when compared with the surrogate-based dose accumulation and especially the "irregular breathing situation". It should, however, be noted that for the case at hand the irregularities in the spirometry records are very pronounced compared to other patients. Further, the discrepancies between standard and situation-adapted dose accumulation are consequences of both breathing signal variations and the interplay effects mentioned in Section 2.3. The example case gives, nevertheless, an intuitive illustration of the principle and the idea behind the situation-adapted dose accumulation.

4 Conclusions

Current RT techniques to cope with respiratory motion usually rely on the use of breathing signals, also referred to as surrogates (of internal motion patterns). Taking into account a trend toward multi-dimensional surrogates, we applied the Log-Euclidean framework for defining a diffeomorphic MLR-based correspondence model and, considering different types of breathing signals, presented a first evaluation of its accuracy. Further, its use for incorporating surrogate-based information about breathing motion variations into 4D dose calculation has been illustrated. At this, the focus of the contribution lay on the theoretical concept of both the diffeomorphic MLR-based correspondence modeling and the surrogate-based dose accumulation with the results presented being a first proof-of-concept, which has to be approved in following evaluation studies. This addresses – as potential future work – the generation of suitable ground-truth data, perhaps by acquiring repeatedly 4D CT data of the patients or designing appropriate motion phantom studies.

Acknowledgments. Funded by German Research Foundation (HA 2355/9-2).

References

1. Keall, P.J., Mageras, G., Balter, J.M. et al.: The management of respiratory motion in radiation oncology report of AAPM TG 76. Med. Phys. 33, 3874–3900 (2006).
2. Li, G., Citrin, D., Camphausen, K., et al.: Advances in 4D medical imaging and 4D radiation therapy. Technol. Cancer Res. Treat., 7, 67–81 (2008)
3. Schaller, C., Penne, J., Hornegger, J.: Time-of-flight sensor for respiratory motion gating. Med. Phys. 35, 3090–3093 (2008)
4. Klinder, T., Lorenz, C., Ostermann, J.: Prediction framework for statistical respiratory motion modeling. In: Jiang, T., Navab, N., Pluim, J.P.W., Viergever, M.A. (eds.) Medical Image Computing and Computer-Assisted Intervention – MICCAI 2010. LNCS, vol. 6363, pp. 327–334. Springer, Heidelberg (2010).
5. Beg, M.F., Miller, M.I., Trouve, A., Younes, L.: Computing Large Deformation Metric Mappings via Geodesic Flows of Diffeomorphisms. Int. J. Comput. Vision 61, 139–157 (2005)
6. Arsigny, V., Commowick, O., Pennec, X., Ayache, N.: A Log-Euclidean Framework for Statistics on Diffeomorphisms. In: Larsen, R., Nielsen, M., Sporring, J. (eds.) Medical Image Computing and Computer-Assisted Intervention – MICCAI 2006. LNCS, vol. 4190, pp. 924–931. Springer, Heidelberg (2006).
7. Ehrhardt, J., Werner, R., Schmidt-Richberg, A., Handels, H.: Statistical Modeling of 4D Respiratory Lung Motion Using Diffeomorphic Image Registration. IEEE T. Med. Imaging 30, 251–65 (2011)
8. Dupuis, P., Grenander, U., Miller, M.I.: Variational Problems on Flows of Diffeomorphisms for Image Matching. Q. Appl. Math. LVI, 587–600 (1998)
9. Schmidt-Richberg, A., Ehrhardt, J., Werner, R., Handels, H.: Diffeomorphic Diffusion Registration of Lung CT Images. In: van Ginneken, B., et al. (eds.) Medical Image Analysis for the Clinic: A Grand Challenge. pp. 55–62. (2010).
10. Werner, R., Ehrhardt, J. et al.: Towards Accurate Dose Accumulation for Step-&-Shoot IMRT: Impact of Weighting Schemes and Temporal Image Resolution on the Estimation of Dosimetric Motion Effects. Z. Med. Phys. 22, 109–122 (2012)

Lung tumour motion models from cone-beam CT

James Martin[1], Jamie McClelland[1], Christopher Thomas[2], Richard O'Brien[3], Shahreen Ahmed[3], Clare Hartill[3], Connie Yip[3], David Landau[3], Ivan Meir[4] and David Hawkes[1]

[1] Centre for Medical Image Computing, University College London, London.
[2] Medical Physics, Guys and St. Thomas NHS Foundation Trust, London.
[3] Department of Oncology, Guys and St. Thomas NHS Foundation Trust, London.
[4] Vision RT Ltd., Dove House, Arcacia Avenue, London, N3 2JU.
[1] james.martin.09@ucl.ac.uk

Abstract. Presented is a method to build a surrogate-driven motion model of a lung tumour from cone-beam CT (CBCT) projection data. The method is markerless and can utilise a standard CBCT scan from radiotherapy treatments. A motion compensated reconstruction of the tumour region also results from calculation of the tumour motion model. It is envisaged that this technique be used to better assess tumour shape and motion prior to dose delivery and over the course of treatment. The method could also be used to guide gated and tracked treatments. The two-step method involves enhancing the tumour region in the projections, and then fitting the surrogate-driven motion model. Preliminary results on a patient dataset using a surrogate extracted directly from the CBCT projections are presented.

1 Introduction

State of the art radiotherapy treatments rely on the accurate identification of cancerous regions and successful exposure of them to lethal doses of radiation [14]. With the advent of stereotactic body radiotherapy (SBRT), involving fewer treatment fractions and higher dose per fraction, it is important that tumour respiratory motion is taken into account. An increasing body of evidence shows that there are indeed changes between planning and treatment fractions [9, 7, 10, 11, 5], which would invalidate motion models built from 4DCT planning data.

4D-CBCT reconstructions [12] are able to provide an indication of tumour motion on the day of treatment, but produces poor quality reconstructions and could underestimate [1] the true extent of

tumour motion. Presented in this work is a method of building a motion model of the tumour, without markers, utilising a standard CBCT scan during treatment. Briefly introduced in [4], preliminary results on clinical patient data are given.

2 Methods and materials

The method involves enhancing the tumour in each projection and then iteratively determining the motion compensated reconstruction (MCR) and surrogate-driven motion model, using an SSD-driven cost function.

2.1 Tumour enhancement

Prior to fitting a motion model to the data, the projections are first pre-processed to enhance the tumour. A standard FDK reconstruction [3] is performed, from which the tumour region is delineated. A simple program to import the target volume from planning was constructed in MatLab (MathWorks, Massachusetts, USA), which also allows the volume to be stretched in superior-inferior (SI), anterior-posterior (AP) and left-right (LR) directions. This target volume should encompass the tumour and the extent of its motion over the entire scan. A mask is created of the tumour region and used to create two volumes. One is of the tumour region with voxels outside set to the intensity of air. The other is of non-tumour region with the tumour region voxels set to the intensity of air. A CBCT is simulated of the non-tumour region volume and the projections subtracted from the original projections. Given a stationary patient, the resulting enhanced projections would be of just the tumour region. In practice these enhanced projections are corrupted with artefacts, of which the effect is minimised by masking the projections according to the projected tumour region volume, giving the tumour region projections. Figure 1 shows an example projection at various stages of the tumour enhancement process.

2.2 Motion models

A motion model is used to constrain the estimated patient motion to physically realistic variation. A realistic parameterisation of the

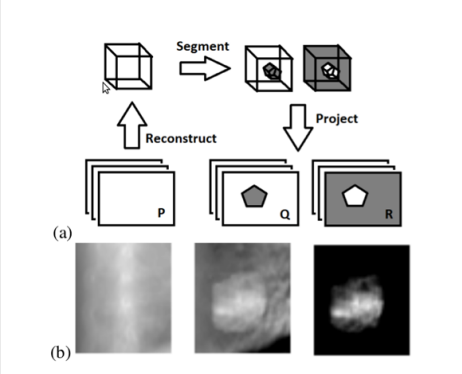

Fig. 1. (a) Illustration of tumour enhancement process. The tumour enhanced projections are the original projections (P) minus non tumour region projections (Q); which are then masked by the tumour region projections (R). (b) Using labels from (a), part of an example projection shown at various stages of tumour enhancement: P, (P-Q) and (P-Q) masked by R, from left to right respectively.

motion of just the tumour region is desired, but one that requires a minimal number of parameters. Assuming that the tumour motion can be approximated as movement of a solid, non-deforming mass, a rigid, translation-only motion model should provide physically realistic motion estimates, whilst providing a low number of parameters to optimise. A simple, linear motion model only requiring the breathing trace current value is used for this work. Surrogate traces were extracted directly from the projections with a method based on [15]. The raw surrogates were then normalised (mean subtracted; divided by standard deviation). The motion model used is:

$$V_{t_n}(\boldsymbol{x}) = V_{t_0}(\boldsymbol{x} + s_{t_n}\boldsymbol{m}), \tag{1}$$

where $\boldsymbol{x}$ is an artibrary point in the patient volume. V_{t_n} is the patient volume at the time t_n of the n^{th} projection, with the first projection taken at time t_0. V_{t_0} is the reference volume. A projection at time t_n has an associated scalar surrogate signal value s_{t_n}. $\boldsymbol{m}$ is a three element vector which determines the SI, AP and LR motion dependence on the current value of the surrogate signal s_{tn}, respectively.

2.3 Iterative approach to calculate motion compensated reconstruction (MCR) and motion model parameters

Using an approach first presented in [4], we attempt to jointly estimate the MCR and motion model parameters iteratively. Beginning with zero motion (i.e. $\boldsymbol{m} = \mathbf{0}$), an MCR is calculated. An open-source, FDK-based reconstruction algorithm was modified for the reconstructions [8]. MCRs werecalculated by back-projecting each projection through the inverse transformation of that that the motion model estimated, given the motion model parameters.

The MCR was used as the reference volume and the motion model parameter updates calculated. An SSD-based cost function is combined with an optical flow approach, to re-express the difference between actual and simulated projections (residue) as motion model parameter updates [6]. Because of the form of the motion model, the cost function could be expressed in a manner which reduced the optimisation time.

$$\boldsymbol{\delta m} = \underset{\boldsymbol{\delta m}}{argmin} \left[\sum_{\theta,\phi=0}^{3} \lambda_\theta \lambda_\phi \sum_{t_n} \sum_{pixels} C_\theta C_\phi \right], \tag{2}$$

where

$$\begin{aligned} &\lambda_0 = 1; \quad C_0 = R_{t_n}; \\ &\lambda_1 = \delta m_z; \, C_1 = -s_{t_n} P_{t_n} \left(\partial_z V_{t_n} \right); \\ &\lambda_2 = \delta m_y; \, C_2 = -s_{t_n} P_{t_n} \left(\partial_y V_{t_n} \right); \\ &\lambda_3 = \delta m_x; \, C_3 = -s_{t_n} P_{t_n} \left(\partial_x V_{t_n} \right); \end{aligned} \tag{3}$$

R_{t_n} is the residue for the simulated and actual projections at time t_n, described earlier. P_{t_n} is the forward projection operator. ∂_z, ∂_y and ∂_x are the partial derivatives in SI, AP and LR directions, respectively. The parameter space was searched for the minimum, giving the motion model parameter updates $\boldsymbol{\delta m}$. A BFGS Quasi-Newton method with a cubic line search procedure [2] was used to search the parameter space. The new motion model parameters $\boldsymbol{m}_{new}$ can now be calculated:

$$\boldsymbol{m}_{new} = \boldsymbol{m} + \boldsymbol{\delta m}. \tag{4}$$

After recalculating the MCR with the new motion model parameters, the process is repeated until the convergence. The algorithm was terminated if the motion model updates gave a maximum additional shift of less than one voxel (i.e. the largest additional shift over all seen surrogate values less than one voxel), or if a maximum number of iterations was met (set at 10).

3 Results

Preliminary testing of the algorithm on patient data is given. Two sequential CBCT scans (termed scan A and scan B) during a fraction of SBRT treatment were used. Scans were taken on an Elekta Synergy (Elekta, Crawley, UK) at Guys and St. Thomas Hospital (London, UK). For this dataset, circa 700 projections were taken at an acquisition rate of 5.5Hz. Simulating the 3D trajectory of both scans and motion model parameters, the average maximum variations were 11.9, 2.10 and 0.63mm in the superior-inferior (SI), anterior-posterior (AP) and left-right (LR) directions, respectively. The mean (max) RMS errors of using either extracted motion model parameters were 0.412mm (1.09) for the scan A estimated trajectory, and 0.425mm (1.16) for scan B's. Please see Table 1 for further information. Figure 2 shows the original and motion compensated reconstructions using the original projections of scan B.

Table 1. Maximum tumour motion by surrogate source and extracted motion model parameters.

Trajectory	Motion model parameters	Max. motion (mm) (SI,AP,LR)
Scan A	Scan A	12.5, 1.75, 1.23
Scan A	Scan B	11.0, 2.42, 0.01
Scan B	Scan A	12.7, 1.78, 1.25
Scan B	Scan B	11.2, 2.46, 0.01
Mean		11.9, 2.10, 0.63

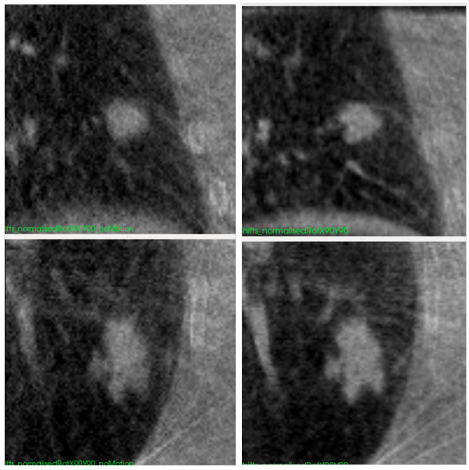

Fig. 2. Slices of scan B reconstructions with (right) and without (left) motion compensation.

4 Discussion

The authors have presented preliminary evidence that tumour motion can be extracted from a CBCT scan and used to build a motion model and MCR. The simple motion model presented here is able to improve the quality of the reconstruction and allow target volume motion to be assessed prior to treatment. There is an improvement in contrast of the surrounding structures, such as airways, which move similarly to the tumour. Structures that do not move as the tumour appear more blurred in the MCR. The method provides encouraging results, even in the presence of scatter and limited field of view (possible missing patient anatomy in the reconstruction) artefacts affecting CBCT scans. By optimising the code and utilising a GPU, the authors are confident convergence could be achieved within a clinical timeframe; minutes as opposed to hours. The authors are currently performing tests on further datasets and with other surrogates. Motion models which can account for hysteresis are also being tested. Work on extending the motion model to include more complex deformations, and modelling motion of the organs at risk are also planned.

Acknowledgments

James Martin gratefully acknowledges the support of the EPSRC funded UCL VEIV EngD programme and Vision RT. Jamie McClelland acknowledges the support of EPSRC project EP/H046410/1.

References

1. Biederer, J., Dinkel, J., Remmert, G., Jetter, S., Nill, S., Moser, T., Bendl, R., Thierfelder, C., Fabel, M., Oelfke, U., Bock, M., Plathow, C., Bolte, H., Welzel, T., Hoffmann, B., Hartmann, G., Schlegel, W., Debus, J., Heller, M., Kauczor, H.U.: 4d-imaging of the lung: Reproducibility of lesion size and displacement on helical ct, mri, and cone beam ct in a ventilated ex vivo system. International Journal of Radiation Oncology*Biology*Physics 73(3), 919 – 926 (2009)
2. Broydon, C.G.: The convergence of a class of double-rank minimization algorithms. Journal Int. Math Applic. 6, 76–90 (1970)
3. Feldkamp, L.A., Davis, L.C., Kress, J.W.: Practical cone-beam algorithm. J. Opt. Soc. Am. A 1(6), 612–619 (Jun 1984)
4. Martin, J., McClelland, J., Thomas, C., Wildermuth, K., Landau, D., Ourselin, S., Hawkes, D.: Motion modelling and motion compensated reconstruction of tumours in cone-beam computed tomography. In: Mathematical Methods in Biomedical Image Analysis (MMBIA), 2012 IEEE Workshop on. pp. 281 –286 (jan 2012)
5. McClelland, J.R., Hughes, S., Modat, M., Qureshi, A., Ahmad, S., Landau, D.B., Ourselin, S., Hawkes, D.J.: Inter-fraction variations in respiratory motion models. Physics in Medicine and Biology 56(1), 251 (2011)
6. Odille, F., Vuissoz, P.A., Marie, P.Y., Felblinger, J.: Generalized reconstruction by inversion of coupled systems (grics) applied to free-breathing mri. Magnetic Resonance in Medicine 60(1), 146–157 (2008)
7. Redmond, K.J., Song, D.Y., Fox, J.L., Zhou, J., Rosenzweig, C.N., Ford, E.: Respiratory motion changes of lung tumors over the course of radiation therapy based on respiration-correlated four-dimensional computed tomography scans. International Journal of Radiation Oncology*Biology*Physics 75(5), 1605 – 1612 (2009)
8. Rit, S., Wolthaus, J.W.H., van Herk, M., Sonke, J.J.: On-the-fly motion-compensated cone-beam ct using an a priori model of the respiratory motion. Medical Physics 36(6), 2283–2296 (2009)
9. Seppenwoolde, Y., Shirato, H., Kitamura, K., Shimizu, S., van Herk, M., Lebesque, J.V., Miyasaka, K.: Precise and real-time measurement of 3d tumor motion in lung due to breathing and heartbeat, measured during radiotherapy. International Journal of Radiation Oncology*Biology*Physics 53(4), 822 – 834 (2002)
10. Sonke, J.J., Lebesque, J., van Herk, M.: Variability of four-dimensional computed tomography patient models. International Journal of Radiation Oncology*Biology*Physics 70(2), 590 – 598 (2008)
11. Sonke, J.J., Rossi, M., Wolthaus, J., van Herk, M., Damen, E., Belderbos, J.: Frameless stereotactic body radiotherapy for lung cancer using four-dimensional cone beam ct guidance. International Journal of Radiation Oncology*Biology*Physics 74(2), 567 – 574 (2009)
12. Sonke, J.J., Zijp, L., Remeijer, P., van Herk, M.: Respiratory correlated cone beam ct. Medical Physics 32(4), 1176–1186 (2005)

13. Tikhonov, A.N.: Solutions of Ill Posed Problems. Winston, Washington and New York (1977)
14. Verellen, D., De Riddeer, M., Linthout, N., Tournel, K., Soete, G., Storme, G.: Innovations in image-guided radiotherapy. Nature Review (2007)
15. Zijp, L., Sonke, J.J., van Herk, M.: Extraction of the respiratory signal from sequential thorax cone-beam x-ray images. In: International Conference on the Use of Computers in Computational Radiotherapy 2004 (2004)

Improved accuracy in 2D/3D registration for image guided radiotherapy by using kV-MV image pairs

Hugo Furtado[13], Michael Figl[13], Markus Stock[23], Dietmar Georg[23], and Wolfgang Birkfellner[13]

[1] Center for Biomedical Engineering and Physics, Medical University Vienna, Austria
[2] Department of Radiation Oncology, Medical University Vienna, Austria
[3] Christian Doppler Laboratory for Medical Radiation Research for Radiation Oncology, Medical University Vienna, Austria

Abstract. Patient motion during radiotherapy (intra-fractional motion), is one of the major sources of uncertainty in dose application. 2D/3D registration is an intensity based method used successfully to track tumor motion with the potential to reduce uncertainty. Despite promising results, the direction perpendicular to the 2D imaging plane cannot be accurately resolved leading to an incomplete, five-degrees-of freedom tracking. In this paper, we propose the use of two 2D images to improve registration results. Modern LINACs have the ability to acquire mega-voltage images, with significantly different contrast, simultaneously to the kilo-voltage image acquisition. Our results show that, when using both images, registration accuracy in all six degrees of freedom dramatically improves. This means that accurate motion tracking can be performed and it integrates easily with the clinical workflow.

Keywords: 2D/3D registration, motion tracking, radiation therapy, kilo-Voltage/mega-Voltage

1 Introduction

One of the major sources of uncertainty in dose application during radiotherapy is patient motion during the treatment or intra-fractional motion. Periodic motion related to the breathing cycle or heartbeat and other forms of aperiodic motion require the enlargement of the planned target volume (PTV) to make sure the full tumor is correctly irradiated. The most important consequence is that dose delivery is increased to healthy tissue.

Tumor motion tracking can help reduce the PTV by reducing the uncertainty about tumor position and help deliver more precise therapy. In the case of lung tumors, approaches to motion tracking include tracking of implanted fiducial markers [10], magnetic transponders [11], external surrogate markers [2] and correlation of external motion with lung motion models [9]. Recently, the CyberKnife® system has also the possibility of intensity based markerless tumor tracking using two cameras [1] where the the tumor position is detected at

certain points of the breathing cycle and correlated to external markers. Purely intensity based 2D/3D registration [4] is an important approach as it does not require markers or fiducials to be implanted and can deal well with aperiodic motion. Despite promising results, an intrinsic problem with this approach is the inability to accurately resolve displacement occurring in the direction perpendicular to the imaging plane [12].

Modern LINACs have not only the ability to acquire portal kiloVoltage (kV) images during treatment but also the possibility to acquire a megaVoltage (MV) image using the treatment beam. The two images are, at least in the case of the Elekta^{TM} treatment machines, perpendicular and they can both be used for 2D/3D registration. In this paper, we present a comparison of registration results when using only one kV image or when using different combinations of kV and MV images. We evaluated the different combinations using a porcine phantom data set and standard patient data. Our results on both data sets show that when using both images registration accuracy increases, leading to more accurate motion tracking in six degrees-of-freedom.

2 Materials and methods

2.1 2D/3D registration

2D/3D registration is a widely used approach in image guided interventions [6]. In a first step, a simulated x-ray image - a DRR - is generated from a 3D volume by a ray casting algorithm, simulating the attenuation of virtual x-rays. The DRR image is then compared to the x-ray image acquired during treatment by means of a merit function. An optimizer searches for the spatial transformation which generates the best match between the DRR and the x-ray. The final translational and rotational parameters $(t_x, t_y, t_z, \omega_x, \omega_y, \omega_z)$ represent the tumor displacement. In this work we used a mutual information (MI) [3] based merit function and the optimization was performed using the Powel optimizer [8].

2.2 Image datasets and Image preprocessing

For the evaluation, we used a freely available porcine head dataset [7] and images from a patient undergoing routine treatment in our clinic. From the porcine dataset we used computed tomography (CT) 3D images and four 2D images: two kV images taken from lateral (LAT) and anterior-posterior (AP) views and two MV images taken from the same views. The gold-standard transformation between all images is available. Because the porcine head features soft tissue which can deform, registration was performed on a region of interest (ROI). Figure 1 shows the 2D images for the LAT view and the ROI mask used.

The patient dataset consists of images from a patient suffering from non-small cell lung cancer undergoing regular treatment in our clinic. We used a planning CT volume where the tumor margins and organs at risk were delineated in a standard planning procedure, a sequence of (151) kV x-ray images and a sequence

of (52) MV x-ray images acquired simultaneously during treatment with rates of approximately 5.4 Hz and 2 Hz respectively. The registration is done on a region of interest (ROI) centered around the PTV for two reasons: (a) the PTV is the region where we want to follow motion and where the assumption of a rigid transformation is valid and (b) rendering a smaller area is also less time consuming as there are less pixels to render. Figure 2 shows a CT slice with the planning contoured structures (left) and one kV x-ray and one MV x-ray with the structures projected on them (center and right).

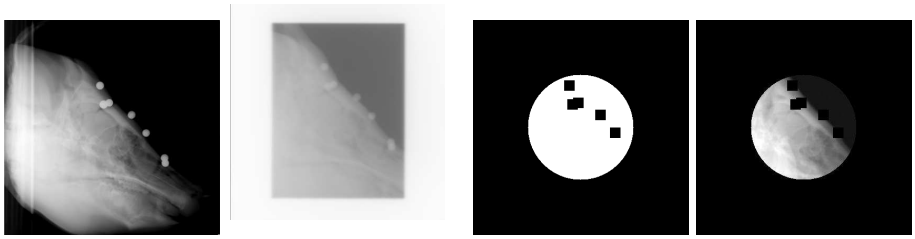

Fig. 1. Pig 2D image data: The first column shows a kV images from lateral view, the second column a correponding MV image, the third, the mask used for the ROI and the last column shows the kV image after masking

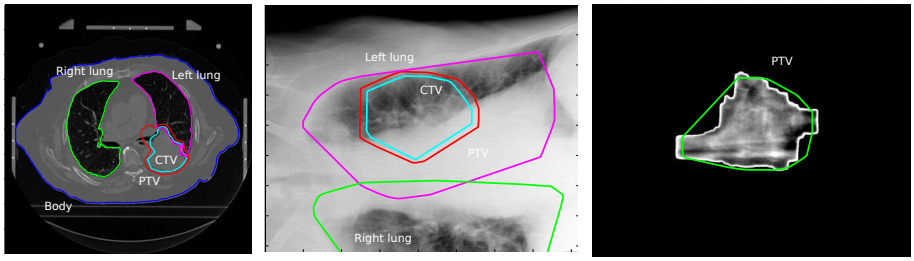

Fig. 2. Patient image data: On the left a slice of the planning CT with the planning structures is shown, on the center the structure were projected on an X-ray acquired during treatment and on the right, only the PTV was projected on an EPID image acqured during treatment.

The sequence of patient kV and MV images, was acquired with different rates. The sample rate ratio was not accurately known and so, the time correspondence between images was not defined. To find this correspondence, first the ground truth motion was extracted from both sequences by segmenting visible features on the images (e.g. the diaphragm). Then, the motion with lower sample rate (MV) was iteratively re-sampled until a maximum of cross correlation between both motion signals was found.

2.3 Evaluation methodology

We followed slightly different evaluation approaches for each of the datasets as they have different characteristics. In the case of the pig, only static images are available but with a well known gold standard. In the case of the patients, there is no gold standard but a fluoroscopic image sequence was available. The general approach consisted in comparing the accuracy of the 2D/3D registration using only one 2D image and 2D image pairs.

For the pig dataset, the accuracy evaluation was performed following the methodology proposed by [5] where a mean target registration error (mTRE) metric is used. The mTRE, consists of the mean of distances between target points spread evenly on the volumes, transformed by the ground truth, and by the transformation obtained with the registration method. We compared registrations performed using only one 2D image (referred to as 1-kV), one kV and one MV image (kV-MV) and two kV images (2-kV). For each of the combinations we evaluated the registration results using 250 initial displacements, chosen randomly, which are offsets of the gold standard. The total initial mTRE ranges from 0 to 25 mm in steps of 1 mm with 10 points at each step.

For the patients, we performed different registration sequences attempting to extract tumor motion as described in [4]. To compare performance, we extracted motion in 5 degrees-of-freedom (DOF) using only the kV sequence, in 6 DOF using only the MV sequence and in 6 DOF using a sequence of kV-MV image pairs. In the latter case, we used a subset (52) of the kV images that approximately corresponds to the MV image sequence in time.

Although there is no gold standard available, we also performed an evaluation similar to the pig dataset, where we used a pair of 2D images (kV-MV) that correspond well in time, and evaluated results using 150 initial displacements from an initial point, evaluating the coherence of registration results. The total initial mTRE ranges from 0 to 15 mm in steps of 1 mm.

3 Results

The results obtained for the pig dataset are shown in table 1 as mean and standard deviation final mTRE for all the registrations. Figure 3 shows a plot of individual registration results leaving out results that are above 25 mm. Table 2 shows the mean, standard deviation and rms of the error of the final translation parameters in relation to the gold standard summarizing the error data for all registrations.

Regarding the patient resuls, figure 4 shows the reconstructed tumor centroid motion along the cranial-caudal (CC, blue line), left-right (LR green line) and anterion-posterior (AP red line) directions in 5 DOF using only the kV image sequence for registration. The black dashed line shows the extracted diaphragm motion. The major contribution to the motion is in the CC direction as was seen in our previous work [4]. Figure 5 shows a plot of the extracted tumor centroid motion along the AP direction (the direction perpendicular to the kV

	mTRE: MEAN ± STD (mm)
1-kV	4.9 ± 4.1
kV-MV	1.8 ± 1.1
2-kV	1.7 ± 1.3

Table 1. Mean (MEAN) and standard deviation (STD) of mTREs for the different image combinations.

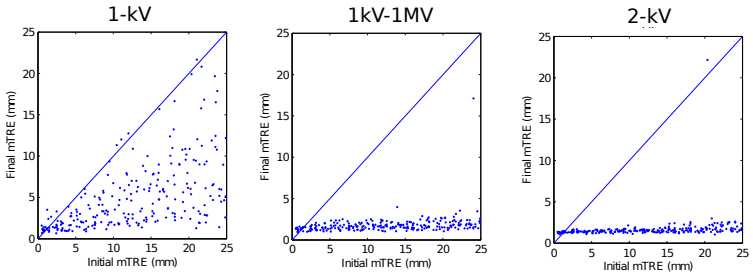

Fig. 3. Plots of individual registration results for each of the image combinations: one kV image (first row), one kV and one MV images (second row) and two kV images calculated using a mutual information based merit function.

	error t_x (mm)		error t_y (mm)		error t_z (mm)	
2D image	MEAN ± STD	RMS	MEAN ± STD	RMS	MEAN ± STD	RMS
1-kV	0.2 ± 0.2	0.3	-0.3 ± 0.3	0.4	0.1 ± 5.7	5.7
1kV-1MV	0.3 ± 0.1	0.3	-0.2 ± 0.1	0.3	-1.0 ± 0.5	1.1
2-kV	0.4 ± 0.1	0.5	-0.5 ± 0.1	0.5	-0.2 ± 0.2	0.3

Table 2. Summary of the offset error in relation to the gold standard for the three translation parameters, X, Y and Z. The offset errors are shown as the mean (MEAN) ± standard deviation (STD) and the root mean square (RMS) error.

imaging plane) for three registration combinations: 5 DOF with one 2D image sequence, 6 DOF with one 2D image sequence and 6 DOF with a kV-MV image pair sequence. The motion along the AP direction ranges from very little to up to 25 mm in the case of registration in 6 DOF with only one 2D image sequence. Table 3 summarizes these results as a mean, standard deviation and RMS amplitute of the motion in the AP direction for the three registration sequences.

Finally, figure 6 shows a comparison of the final registration translation parameter t_z (shown as offset to the mean), for 150 starting positions with increasing initial mTRE when using only one kV image (left) and a kV-MV image pair (right). Table 4 summarizes these results as mean and standard deviation of the final translation parameters for both cases.

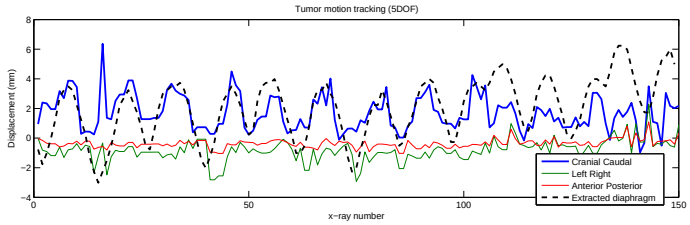

Fig. 4. Reconstructed motion of the centroid of the tumor along CC (blue line), LR (green line), AP (red line) directions for the patient dataset in 5 degrees of freedom using only the kV image sequence. The diaphragm motion is also shown as a black dotted line. Note that some outliers are omitted in the case of the AP direction.

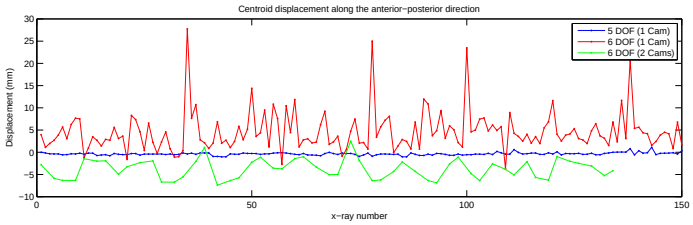

Fig. 5. Reconstructed motion of the centroid of the tumor along the AP direction for the patient dataset, in 5 DOF using one 2D image for registration (blue line) in 6 DOF using one 2D image for registration and in 6 DOF using two 2D images for registration.

4 Discussion and Conclusions

Our results demonstrate the improvement on accuracy by using two 2D images in the 2D/3D registration. For the pig dataset, it is easily seen in figure 3 that when only one image is used, the mTRE increases as the initial displacement also increases. The large errors stem from a random final t_z parameter as this translation cannot be accurately resolved with only one projection. The data in table 1 and table 2 confirm this finding showing that the final mTRE and

	Motion along AP direction (mm)	
2D image	MEAN ± STD	RMS
1-kV (5DOF)	-0.37 ± 0.3	0.48
1-kV (6DOF)	4.61 ± 4.52	6.45
2-kV (6DOF)	-3.78 ± 2.22	4.37

Table 3. Summary of the tumor centroid motion along the AP direction shown as the mean (MEAN) ± standard deviation (STD) and RMS of the amplitude of the set of registrations over time.

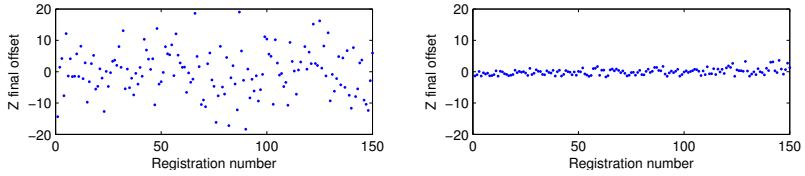

Fig. 6. Plots of the offset to the mean of the final translation parameter t_z for the individual registrations on the patient data shown for the two a image combinations, 1-kV and 1kV-1MV

	t_x (mm)	t_y (mm)	t_z (mm)
2D image	MEAN ± STD	MEAN ± STD	MEAN ± STD
1-kV	4.94 ± 1.89	-7.55 ± 2	545.83 ± 7.4
1kV-1MV	13.38 ± 1.14	-3.84 ± 1.63	534.78 ± 1.07

Table 4. Summary of the offset error in relation to the gold standard for the three translation parameters, X, Y and Z. The offset errors are shown as the mean (MEAN) ± standard deviation (STD) and the root mean square (RMS) error of the offset of the gold standard. The registration was calculated for the four different merit functions.

the parameter error is much lower when an image pair is used. The results are slightly better when two kV images are used but typically, there is only the possibility of acquiring a kV-MV image pair during treatment.

For the patient dataset, tumor motion could be tracked in 5 DOF with reasonable accuracy. Figure 4 shows good correlation between extracted diaphragm motion and tumor motion obtained by registration. It is evident from figure 5 that extracting tumor motion in 6 DOF using only a kV image sequence for registration leads to high inaccuracy. It is known that there is almost no motion in the AP direction so we can conclude that the extracted motion is incorrectly resolved, as large displacements (red line) are shown. When using a sequence of image pairs (green line) the motion is again much smaller. Table 3 also shows that both the standard deviation and the RMS of the motion amplitude are significantly smaller when an image pair sequence is used.

Finally, in figure 6 the displacement perpendicular to the imaging plane (here Z direction) is not accurately resolved (left) in contrast with the case when using image pairs (right) where much smaller offset to the mean is obtained. This is also seen in table 4 where a dramatic decrease in standard deviation on the Z translation parameter is shown when using two images for registration.

It is important to say that for the time being, these results are preliminary as accuracy can improve. One of the main sources of uncertainty comes from the fact that the kV and MV image pair sequences do not have a one to one correspondence in the time domain. Further work has to be done to deal with images pairs that are not taken at the same point in time or a synchronization mechanism has to be implemented.

Despite this, taking the presented results into account, we can say that using a pair of images for registration is a good approach to improve accuracy. This is also workflow efficient as acquiring extra MV imaging during treatment adds no additional dose to the patient or burden to the physician.

Acknowledgments. The financial support by the Federal Ministry of Economy, Family and Youth and the National Foundation for Research, Technology and Development is gratefully acknowledged.

References

1. Bibault, J.E., Prevost, B., Dansin, E., Mirabel, X., Lacornerie, T., Lartigau, E.: Image-guided robotic stereotactic radiation therapy with fiducial-free tumor tracking for lung cancer. Radiation Oncology p. 102 (2012), article in press.
2. Cho, B., Poulsen, P.R., Sawant, A., Ruan, D., Keall, P.J.: Real-time target position estimation using stereoscopic kilovoltage/megavoltage imaging and external respiratory monitoring for dynamic multileaf collimator tracking. Int. J. Radiat. Oncol. Biol. Phys. 79(1), 269–78 (2010)
3. Clippe, S., Sarrut, D., Malet, C., Miguet, S., Ginestet, C., Carrie, C.: Patient setup error measurement using 3D intensity-based image registration techniques. International Journal of Radiation Oncology Biology Physics 56(1), 259–265 (2003)
4. Gendrin, C., Furtado, H., Weber, C., Bloch, C., Figl, M., Pawiro, S., Bergmann, H., Stock, M., Fichtinger, G., Georg, D., Birkfellner, W.: Monitoring tumor motion by real time 2d/3d registration during radiotherapy. Radiotherapy and Oncology 102(2), 274–280 (2012)
5. van de Kraats, E.B., Penney, G.P., Tomaževič, D., van Walsum, T., Niessen, W.J.: Standardized evaluation methodology for 2-D-3-D registration. IEEE Transactions on Medical Imaging 24(9), 1177–1189 (2005)
6. Markelj, P., Tomaževič, D., Likar, B., Pernuš, F.: A review of 3d/2d registration methods for image-guided interventions. Med. Image Anal. In press (2010)
7. Pawiro, S.A., Markelj, P., Pernuš, F., Gendrin, C., Figl, M., Weber, C., Kainberger, F., Noebauer-Huhmann, I., Bergmeister, H., Stock, M., Georg, D., Bergmann, H., Birkfellner, W.: Validation for 2d/3d registration. i: A new gold standard data set. Med. Phys. 38(3), 1481–1490 (2011)
8. Powell, M.: Nonconvex Optimization and Its Applications, chap. The NEWUOA sorftware for unconstrained optimization without derivatives, pp. 255–297. Springer US (2006)
9. Ren, Q., Nishioka, S., Shirato, H., Berbeco, R.I.: Adaptive prediction of respiratory motion for motion compensation radiotherapy. Phys. Med. Biol. 52(22), 6651–6661 (2007)
10. Schweikard, A., Glosser, G., Bodduluri, M., Murphy, M.J., Adler, J.R.: Robotic motion compensation for respiratory movement during radiosurgery. Comput. Aided Surg. 5(4), 263–277 (2000)
11. Shah, A.P., Kupelian, P.A., Willoughby, T.R., Langen, K.M., Meeks, S.L.: An evaluation of intrafraction motion of the prostate in the prone and supine positions using electromagnetic tracking. Radiotherapy and Oncology 99(1), 37–43 (2011)
12. Suh, Y., Dietrich, S., Keall, P.J.: Geometric uncertainty of 2d projection imaging in monitoring 3d tumor motion. Phys. Med. Biol. 52, 3439–3454 (2007)

Deformable Registrations for Head and Neck Cancer Adaptive Radiotherapy

Catarina Veiga[1], Jamie McClelland[1], Kate Ricketts[1], Derek D'Souza[2] and Gary Royle[1]

[1] Department of Medical Physics and Bioengineering, University College London
[2] Radiotherapy Physics Group, University College London Hospital

Abstract. Preliminary tests and results are described to evaluate the accuracy and robustness of a FFD voxel-based deformable registration algorithm in registering planning CTs to CBCTs from head and neck patients. Similarity measures, computation time and visual inspection are used to assess the effect of different registration parameters in the results and to find a promising interval of parameters' values.

1 Motivation

Developments in radiotherapy techniques aim at delivering increasingly more conformal doses to the target volumes while sparing the surrounding healthy tissues. However, the steeper the dose gradients become the more important it is to precisely set up the patient. This includes accurate positioning of the internal organs [1]. Inaccuracy in positioning can cause underdosage of the target volume and overdosage of normal tissues, which can result in increased risk of tumour recurrence and complications [2].

The incorporation of daily setup images taken on the treatment site into the radiotherapy process can facilitate adaptive radiation therapy (ART). In ART the treatment is evaluated periodically using in-room imaging, such as cone-beam computed tomography (CBCT), and the plan is adaptively modified to take in consideration changes in dose due to changes in patient setup and anatomy [3].

ART could be particularly useful for head and neck (HN) patients due to the complexity of the surrounding anatomy and the proximity to several radiosensitive critical structures. Conventionally, it is assumed that the targets in the HN region are quite rigidly attached to the bony anatomy [4] and so organ motion is minimal. However, recent studies report progressive changes in the patient anatomy during the course of the treatment and relate them to dosimetric changes from the original plan [2][5][6]. The reasons for anatomical changes are multifactorial and can be related with the decrease of tumour and nodal volumes, weight loss (due to difficulties in swallowing), alteration in muscle mass and fat distribution, fluid shift within the body [7] and resolving posteoperative changes/edema [2]. Studies done on mid-treatment re-planning of HN patients show that there is benefit to some patients, but there is no method to identify the ones that will benefit more from replanning and the optimal timeframe for it to take place.

For some HN patients at least one replanning is necessary. Currently replanning is done in University College London Hospital (UCLH) in Intensity Modulated Radiation Therapy (IMRT) treatments only when absolutely necessary, usually mid-way through the treatment when considerable anatomical changes take place and the patient no longer fits in their personal immobilizing thermoplastic mask. The new plan is built from scratch by acquiring a new planning CT and without accurately knowing the dosimetric consequences so far. It may be more beneficial to replan the patients earlier in their treatment, but there is no evaluation method to assess the necessity and timing for replanning.

UCLH and University College London (UCL) are currently developing a clinical proton therapy facility, expecting to treat its first patients in 2017. In Proton Therapy (PT) accounting for setup and anatomical changes becomes even more important as more conformal doses are delivered and the dose distribution is more sensitive to the patient's anatomy. Therefore, the question of if and when to replan is even more relevant in PT.

It is widely accepted in literature that the future of ART depends on the use of accurate deformable registration algorithms [7][8][9]. A deformable registration resolves the major challenges in ART: planning CT scans warped to match the daily CBCT can be used for reliable dose calculations, regions of interest can be propagated from the planning CT and daily dose distributions can be warped back to the planning CT to calculate the accumulated delivered dose [6]. The main challenge is in how to proper validate deformable registrations on clinical data, so for now they must be used with care.

In this work we investigate a deformable registration algorithm to register the planning CT and weekly CBCT images taken from HN patients. These findings will be useful for developing and validating a future ART protocol for HN patients.

2 Methods and Materials

NifTK software was developed by the Centre of Medical Image Computing (CMIC), at the Department of Medical Physics and Bioengineering of UCL. The software is in constant development and contains several tools for image registration and visualization. It combines a set of different toolkilts, including the open-source NiftyReg (http://cmic.cs.ucl.ac.uk/home/software) for rigid and deformable image registration, and a viewer (NiftyView).

The rigid/affine registration code uses a Block Matching algorithm [10], while the deformable registration code is a re-factoring of Rueckert et al. (1999) Free-Form Deformation (FFD), based on B-Splines and a voxel-based similarity measurement - Normalized Mutual Information (NMI) [11]. The major differences from the original paper are in the calculation of the gradient and joint histogram, introduction of other penalty terms, and a GPU implementation, which make the code faster and more robust [12].

In this preliminary study we aim to evaluate the image registration algorithm on a small set of data to find a set of promising parameters to use in further

studies. This set of parameters should give good results for any HN registration by minimizing the computation time and keeping acceptable values for the similarity measures. Since high values of similarity measurements do not necessarily mean a better registration the analysis is aided with visual assessment of the registered images. The similariy measure used was the NMI,

$$\mathrm{NMI}(A,B) = \frac{H(A)+H(B)}{H(A,B)} \tag{1}$$

where $H(A)$ and $H(B)$ are the entropy of the images A and B. NMI can take any value between 0 and 2, where higher values correspond to higher similarity and values of NMI$>$ 1 typically represent a good agreement between images. Initial tests using SSD as similarity measure showed that it did not perform well due to the intensity differences between CT and CBCT images.

This study can then be divided in two parts based on the input parameters of the registrations:

1. Optimization of the rigid transformation
   - Effect of masking the reference image;
   - Effect of ignoring the last level of resolution;
2. Optimization of the deformable transformation
   - Effect of the bending energy weight (BE): the bending energy is a penalty term introduced in the cost function to constrain the transformation to be smooth.

$$\begin{aligned}\mathrm{BE} = \int\int\int_{\Omega} \left(\frac{\partial^2 \mathbf{T}}{\partial x^2}\right)^2 + \left(\frac{\partial^2 \mathbf{T}}{\partial y^2}\right)^2 + \left(\frac{\partial^2 \mathbf{T}}{\partial z^2}\right)^2 \\ +2\left[\left(\frac{\partial^2 \mathbf{T}}{\partial xy}\right)^2 + \left(\frac{\partial^2 \mathbf{T}}{\partial xz}\right)^2 + \left(\frac{\partial^2 \mathbf{T}}{\partial yz}\right)^2\right]\end{aligned} \tag{2}$$

   - Effect of the logarithm of the jacobian weight (JL): the logarithm of the jacobian penalty penalizes large local volume changes and prevents folding.

$$\mathrm{JL} = \frac{1}{n}\sum |\log\left(det(\nabla \mathbf{T})\right)| \tag{3}$$

   - Number of histogram bins used to calculate the joint histogram;
   - Effect of thresholding the reference and floating images;
   - Maximum number of iterations used;
   - Control Point (CP) spacing;
   - Effect of masking the reference image;
   - Effect that the choice of rigid transformation has on the deformable registration results;

Registrations were repeated changing the parameters of interest for two clinical datasets from HN patients.

3 Results

Rigid only transformations were applied to describe the global motion, as it is an intra-subject registration. Mask usage in the rigid registration improved the global alignment results and reduced significantly the computation time. Ignoring the last level of registration has no visual effect if masks are used, which reduces the computation time even further. The rigid registrations took approximately 1 minute to compute.

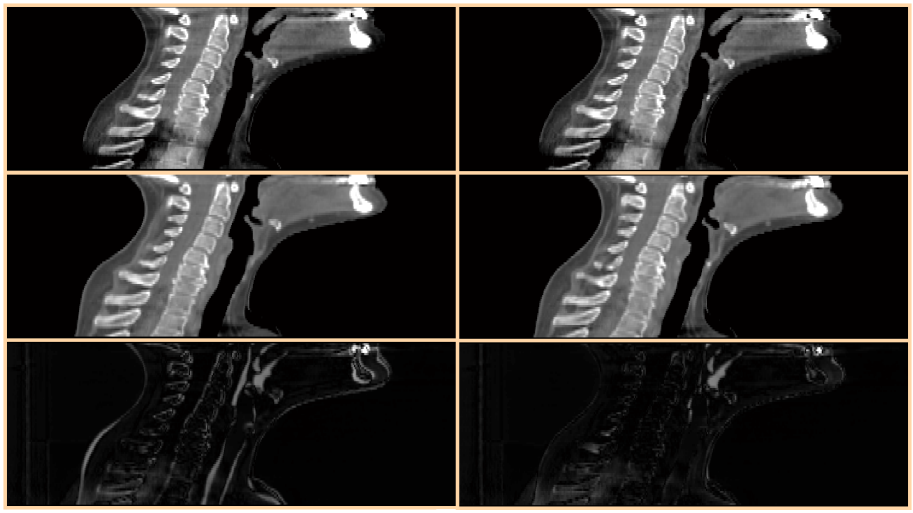

Fig. 1. Saggital slices of the CBCT, registered image and difference image between the two. The first column refers to a rigid-only transformation, and the second to the deformable transformation. Gray areas show where the CBCT and registered image disagree. Even though the anatomy of the HN in conventionally considered rigid, a rigid-only registration cannot fully capture all the changes. A rigid registration shows considerable disagreement in the bone and external contours alignment. Using deformable registration the matching is improved. Near the throat there are still discrepancies due to swallowing.

Regarding the deformable registration,

1. Values of BE within the interval [0.01, 0.10] seem to produce acceptable results. For these two datasets the best visual results are produced by a narrower range ([0.02, 0.06]). Low values of BE may give good NMI values, but visually the alignment is incorrect (Fig. 2).
2. In general, using the jacobian penalty term only causes dramatic visual changes for low values of BE, where folding is more likely to occur. The introduction of this parameter appears to smooth the effect that other parameters changes have. Thus values within [0.01, 0.10] seem like a good

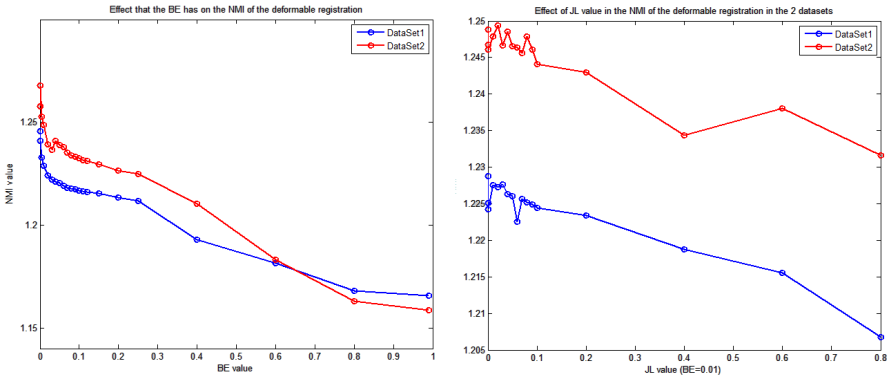

Fig. 2. Decreasing of the NMI value with increasing BE/JL value. Increasing values of BE and JL overall decrease the similarity measure as the code is built to maximize it and penalty terms constrain that maximization.

compromise between constrain of the transformation and stopping folding from occurring.

3. The number of bins used in the joint histogram calculations affects the overall results. Unexpectedly, increasing the number of bins does not seem to increase the computation time but it degrades the final registration. It is possible that a higher binning value makes the code more sensitive to noise in the images. Also, CBCT intensity values for the same type of tissue may vary in different areas of the image so smaller binning intervals may lead to the same tissue being separated in different bins on different zones of the image. Considering NMI values and visual assessment, a binning of 64 was found as acceptable in all tests done.
4. A thresholding may be advisable to remove "padding" values (voxels with intensities inferior to -1000HU) and to deal with high-intensity artefacts. The thresholding conducted showed no improvement in image alignment and computation time. However, since the effect of threshold is similar to the effect of increasing the binning of the joint histogram, for thresholding to have a positive effect the choice of binning must be adjusted properly. We are still to find the best combination of both.
5. Reducing the maximum number of iterations reduces the computation time by forcing the algorithm to finish before it reaches a convergence value. Overall it looks like a good compromise to use a maximum of 1000 iterations at, which limits the maximum computation time to approximately 5 minutes.
6. Good results were achieved when using CP spacing between 5 and 10 voxels. For lower values it is difficult to sufficiently constrain the registration and the algorithm looses the capture range of bigger deformations.
7. The choice of rigid registration parameters does have an impact in the following deformable registration. In general initializing the deformable registration with a better rigid alignment reduces the time spent to reach con-

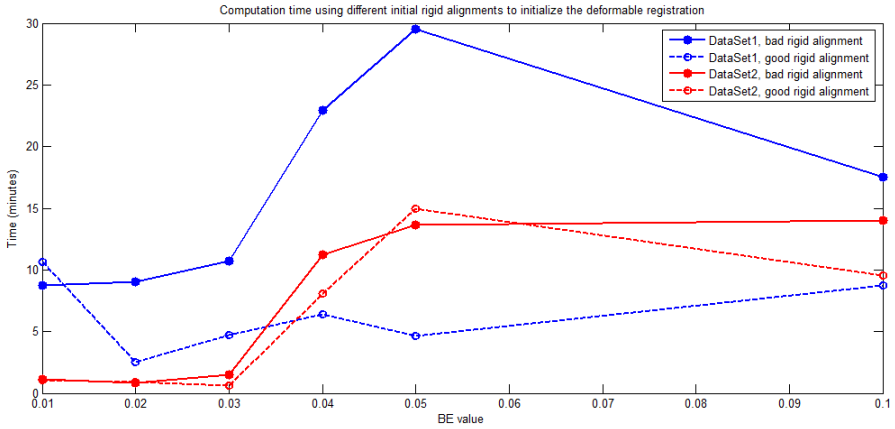

Fig. 3. Computation time using different initial rigid alignments.

vergence (Fig. 3). The final resuls are visually similar while overall the NMI value is slightly improved.

8. Masking the reference image in the deformable transformation reduces the computation time to 1 minute, but can make the registrations more sensitive to other parameters.

Combining all these results, overall the deformable registration takes around 1 minute if a mask is used, and up to a maximum of 5 minutes if none is used.

4 Conclusions

The code used is fairly robust as small changes in the parameters do not cause dramatic changes in the registration results, particularly when the jacobian penalty term is used. For the parameters investigated there are intervals of values that give promising results.

For rigid registrations the best results were achieved using a mask and ignoring the last level of resolution. The optimal parameters found for the deformable registration are: BE=[0.02, 0.06], JL=[0.01, 0.10], a maximum number of 1000 iterations, a binning of 64 for the joint histogram calculation, no thresholding and a control point spacing between 5 and 10 voxels. Such registrations can take up to a maximum of 5 minutes to finish; using a mask this time can be reduced to less than 1 minute.

5 Future Work

On this preliminary work we focused only on two datasets. We will use our findings on more datasets to narrow this range of parameters to a single value,

valid for all HN images produced in UCLH. On this next step we will also include more quantitative analysis of the registration.

Future quantitative checks must assess accuracy, robustness and consistency. They can include jacobian analysis of the deformation field and calculation of other similarity measures that are not maximized by the algorithm, such as the Sum of the Square Distances (SSD). The output of the deformable registration is a deformation field that relates each point in the CT to the CBCT image. This information can be used to deform the contours delineated in the CT to the CBCT space. A quantitative analysis of the registration can be done by comparing the automatically generated contours with the ones drawn by a trained physician (generally considered as gold-standard) by using quantities such as Dice Similarity Index (DSI), Pearson's correlation coefficient (CC) [7], Overlap Index [8] and Distance Transformation (DT).

We will also investigate whether image pre-processing to reduce noise and enhance contrast can improve the registrations.

6 Acknowledgments

The authors would like to thank Marc Modat, Pankaj Daga, Gergely Zombori, and Matt Clarkson for all the help and support with NifTK. C.V. is funded by Fundação para a Ciência e a Tecnologia (FCT) grant SFRH/BD/76169/2011, co-financed by FSE, POPH/QREN and EU.

References

1. Chen, J., Morin, O., Aubin, M., Bucci, M., Chuang, C., Pouliot, J.: Dose-guided radiation therapy with megavoltage cone-beam CT. The British Journal of Radiology 79 (2006) S97-S98
2. Barker, J., Garden, A., Ang, K., O'Danniel, J., Rosenthal, D., Chao, K., Tucker, S., Mohan, R., Dong, L.: Quantification of volumetric and geometric changes occuring during fractionated radiotherapy for head-and-neck cancer using an integrated CT/linear accelerator system. International Journal of Radiation Oncology Biology Physics 59(4) (2004) 960-970
3. Lu, W., Olivera, G., Chen, Q., Ruchala, K., Haimer, J., Meeks, S., Langen, K., Kupelian, P.: Deformable registration of the planning image (kVCT) and the daily images (MVCT) for adaptive radiation therapy. Physics in Medicine and Biology 51 (2006) 4357-4374
4. Zeidan, O., Langen, K., Meeks, S., Wagner, T., Willloughy, T., Jenkis, W., Kupelain, P.: Evaluation of image-guidance protocols in the treatment of head and neck cancers. Int. J. Radiation Oncology Biol. Phys. 67 (2007) 670-677
5. Hansen, E., Bucci, K., Quivey, J., Weinberg, V., Xia, P.: Repeat CT imaging and replanning during the course of IMRT for head-and-neck cancer. International Journal of Radiation Oncology Biology Physics 64(2) (2006) 355-362

6. Lee, C., Langen, K., Lu, W., Haimeri, J., Schnarr, E., Ruchala, K., Olivera, G., Meeks, S., Kupelian, P., Shellenberger, T., Mañon, R.: Assessment of parotid gland dose changes during head and neck cancer radiotherapy using daily, megavoltage computed tomography and deformable image registration. International Journal of Radiation Oncology Biology Physics 71(5) (2008) 1563-1571
7. Castadot, P., Lee, J., Geets, X., Grégoire, V.: Adaptive Radiotherapy for Head and Neck Cancer, Seminars in Radiation Oncology 20 (2008) 84-937
8. Tsuji, S., Hwang, A., Weinberg, V., Yom, S., Quivey, J., Xia, P.: Dosimetric evaluation of automatic segmentation for adaptive IMRT for head-and-neck cancer. International Journal of Radiation Oncology Biology Physics 77(3) (2010) 707-714
9. Castadot, P., Lee, J., Geets, X., Grégoire, V.: Adaptive Radiotherapy for Head and Neck Cancer, Seminars in Radiation Oncology 20 (2010) 84-93
10. Ourselin, S., Roche, A., Subsol, G., Pennec, X., Ayache, N.: Reconstructing a 3D Structure from Serial Histological Sections Image and Vision Computing 19(1) (2001) 25-31(7)
11. Rueckert, D., Sonoda, L., Hayes, C., Hill, D., Leach, M., Hawkes, D.: Non-rigid Registration Using Free-Form Deformations: Application to Breast MR Images. IEEE Transactions on Medical Imaging 18(8) (1999) 712-721
12. Modat, M., Ridgway, G., Taylor, Z., Lehmann, M., Barnes, J., Hawkes, D., Fox, N., Ourselin, S.: Fast free-form deformation using graphics processing unit. Computer methods and programs in Biomedicine 98 (2010) 278-284

Numerical phantom generation to evaluate non-rigid CT/CBCT registration algorithms for prostate cancer radiotherapy

Mathieu Rubeaux[1,2], Guillaume Cazoulat[1,2], Aurélien Duménil[1,2], Caroline Lafond[1,2,3], Oscar Acosta[1,2], Renaud de Crevoisier[1,2,3], Antoine Simon[1,2], and Pascal Haigron[1,2]

[1] INSERM, U 1099, Rennes, F-35000, France
[2] Université de Rennes 1, LTSI, F-35000, France
[3] Département de Radiothérapie, Centre Eugène Marquis, Rennes, F-35000, France
mrubeaux@gmail.com

Abstract. In Image-Guided Radiation Therapy of prostate cancer, the CBCT scan acquired at each treatment fraction could be used to estimate a cumulative dose distribution thanks to non-rigid registration. However, this cumulative dose estimation is highly sensitive to non-rigid registration errors. For this reason, validation of the registration algorithm with organ overlap measures or visual assessment is not sufficient. In this paper, we describe the construction of a numerical phantom based on a finite element model of the prostate and the neighbor organs which can be used to assess the non-rigid registration accuracy. Preliminary results show the potential of this phantom to better characterize registration algorithms than traditional Dice score.

1 Introduction

Image-Guided Radiation Therapy (IGRT) aims at increasing the precision of radiation dose delivery. In the context of prostate cancer, a planning Computed Tomography (CT) image with manually defined prostate and organs at risk (OAR) delineations is usually associated with daily Cone Beam Computed Tomography (CBCT) follow-up images. The CBCT images allow to visualize the prostate position and to reposition the patient accordingly. The goal of this rigid registration step is to avoid the prostate being under-irradiated and subsequently the main OARs (bladder and rectum) to be over-irradiated. However, prostate rigid motion is not the only anatomical variation from fraction to fraction. Large deformations can occur due to bladder and rectum filling variations, leading to a received dose that can differ from the planned one. At any fraction, if dose criteria are not met, the clinician may decide to replan the treatment. To compare the actually received dose with the prescribed one, non-rigid registration is used to estimate the tissue deformation to be able to compute the dose locally accumulated.

In order to register pelvic CT and CBCT images, some approaches have been proposed [1, 2], which combine non-rigid registration and segmentation in order to propagate CT delineations in the CBCT images. To evaluate the accuracy of the registration algorithms used in this context, the Dice score remains one widely used criteria, even if it has been shown [3] that it does not necessarily reflect the quality of the registration. Indeed, the Dice score measures the overlap between two delineations, which

in our context are the CBCT delineations and the propagated CT delineations. It only characterizes the correspondance of the organs, whereas it is necessary to evaluate the local matching of the voxels. Indeed, the radiotherapy requires a precise knowledge of the local dose accumulation. However, obtaining a reference of this local matching is very difficult with real images. Another approach is to use the Target Registration Error using pairs of landmarks that are automatically or manually defined. But due to the poor quality of the CBCT images, this is a difficult task, and the landmarks are usually placed on distinctive anatomical marks (e.g bones), where the registration quality is not as crucial as on the considered organs. Recently, new validation approaches have been developed in order to better characterize the quality of registration algorithms [4]. Our work is part of the effort made to bring some new evaluation procedures for CT/CBCT non-rigid registration of pelvic structures.

To do so, a numerical phantom is generated using a biomechanical model integrating the prostate and the OARs (bladder, rectum and seminal vesicles). This phantom is realistic enough to allow non-rigid registration without modifying algorithm parameters that would be used for real subject registration. Moreover, the transformation model used to generate the numerical organs is different from the ones usually used in non-rigid registration, allowing a fair comparison between different kind of algorithms. Even if these deformations remain simple, they give some answers regarding the validity of the deformation fields estimated during registration.

In the first section, the approach used to generate the numerical phantom is described in detail. Then, some non-rigid registration methods under study are explained, justifying the different components of the scheme. Finally, some preliminary results are given, which show that the numerical phantom allows to discriminate more finely between different registration algorithms.

2 Phantom generation

2.1 Biomechanical model

A finite element model of the prostate and OAR (seminal vesicles, bladder, rectum) is used to generate the phantom. It is described using ANSYS DesignModeler. The geometry of the anatomical structures is defined by considering typical sizes and shapes derived from patient CT data. They are represented by parasolid surfaces from either B-splines contours of organs (rectum) or by geometrical sculpting of object (prostate, seminal vesicles, bladder) and then discretized in surface (rectum, bladder) or volume (prostate, seminal vesicles) finite elements.

The simulation is set up by considering typical elastic material properties for the tissues (Young modulus, Poisson ratio) derived from [5, 6]. The organs' wall thickness and the internal pressures for bladder and rectum are obtained from [7]. The values used fo this simulation are provided in table 1. The boundary conditions are defined by fixed supports attached to the extremities of the rectum and the prostate apex, and elastic support to represent organs surrounding the rectum. Moreover contacts are defined between the different organs of interest. The simulation of organ deformations is performed by ANSYS Mechanical. Different values of internal pressure of rectum

Table 1. Linear elastic material properties and Walls thickness

Organ	Poisson's ratio	Young's modulus (kPa)	Wall thickness (mm)
Bladder	0.49	10	2.9
Rectum	0.45	10	2.28
Prostate	0.4	21	
Seminal Vesicles	0.49	10	1

and bladder are applied to deform the structures in a range comparable with typical deformations observed on real patient through CT data.

Typical results of this simulation are given in figure 1. In this preliminary study, two different simulated sets of organs are used: one to generate a CT phantom, the other to create a CBCT phantom.

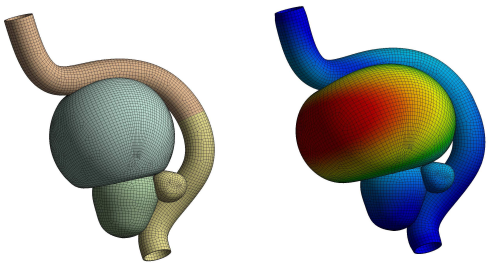

(a) CBCT organs (b) CT organs

Fig. 1. Numerical organs generated using ANSYS. Phantom represented in (a) is used to generate the CBCT phantom, while (b) is used for the CT.

2.2 CT/CBCT reconstruction

To reconstruct synthetic images, the aim is to integrate the finite element models of the different organs in real CT/CBCT images. To do so, two different CT/CBCT images pairs taken from two subjects are considered: the first one ($subjectA$) receive the synthetic organs, while the intensities of the second one ($subjectB$) are used to fill these synthetic organs. The choice to use the organs' intensities of a second subject was guided by technical difficulties encountered while building the phantom. For this data, a clinician manually delineated the prostate and OARs.

The $subjectA$ is drained from its real organs, using the expert delineations. Then the goal is to fill it back with the synthetic organs. The $subjectB$ is used for that purpose. For the bladder and the prostate, an affine registration between the binary images of

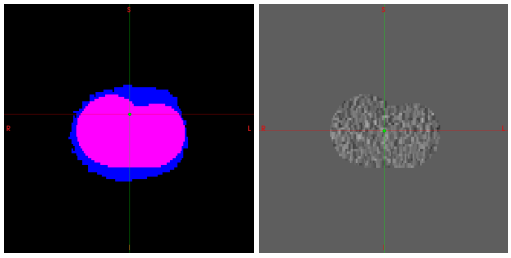

(a) bladder affine registration (b) Filled synthetic bladder

Fig. 2. synthetic CT bladder reconstruction. (a) shows the overlap between syntethic (pink) and $subjectB$ (blue) bladder after affine registration. The intensities of the $subjectB$ bladder taken from the original CT are used to fill the synthetic one (b).

$subjectB$ and the binary images of the synthetic organs is performed. This allows to align the modeled organs with real organs and then to fill the synthetic bladder and prostate with the textures and pixels intensities of $subjectB$.

However, this procedure is not adapted to the rectum and seminal vesicles, due to the geometrical differences between the synthetic organs and the ones of $subjectB$. So some pixels are randomly selected in the $subjectB$ organs to fill the synthetic organs. For the rectum, two regions are differentiated to take into account the gas areas that often come across with the pelvic images. The same procedure is adopted for both CT and CBCT images. An illustration of the synthetic CT bladder reconstruction is given in figure 2.

2.3 Experimental data

Finally, two sets of data are used during the experiments, as shown in figure 3: the numerical CT/CBCT phantom generated as described above, and the $subjectA$, a real patient, which serves as a reference to assess the relevance of the phantom. Two procedures are considered: a phantom CT to CBCT registration, and a real subject CT to CBCT registration.

3 Registration procedure set-up

An iconic registration scheme, taking into account the grey values of the pixels of the images to register, is applied. A registration method is usually defined by i) a similarity measure, ii) a motion model and iii) an optimization procedure. In the experiments, the elastiX toolbox [8] is used during the registration procedures, which allows the reproducibility of the results. The Mutual Information (MI) similarity measure based on Mattes [9, 10] implementation is chosen, since it allows efficient multimodal registration. Regarding the motion model, the registration procedure is divided in two steps: first, a

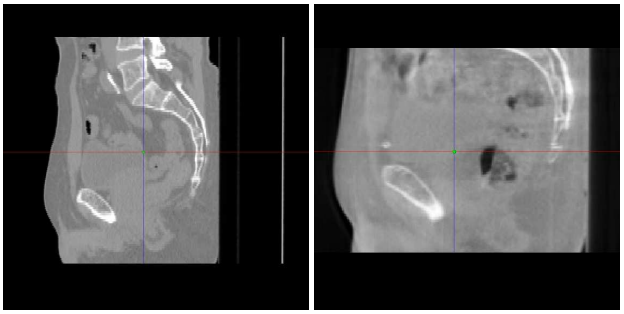

(a) Original CT (b) Original CBCT

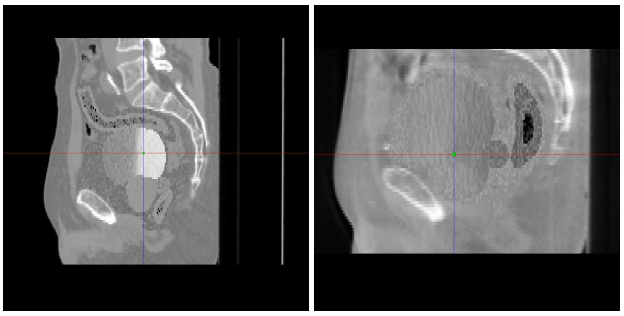

(c) Phantom CT (d) Phantom CBCT

Fig. 3. Images used during the tests. (a) Original CT image. (b) Original CBCT image. (c) Generated CT phantom image. (d) Generated CBCT phantom image.

rigid registration to globally align the two images; second, a non-rigid registration using a Free-Form Deformation (FFD) model based on B-Splines [11]. The optimization is based on the adaptive stochastic gradient descent procedure described in [12]. Moreover, a coarse to fine (or pyramidal) approach allows to register global as well as local motion.

Besides this global scheme, the motion is regularized using two different methods: (i) a penalty term based on the bending energy of a thin metal sheet [11], that insures the global smoothness of the transformation.

(ii) a rigid penalty term [13] on the bones that are extracted by thresholding the original image. This term forces the bones to deform rigidly during the non-rigid registration.

In the following, the three methods are compared. MI denotes the registration scheme without regularization, MI_{BE} stands for the registration with a Bending Energy penalty, while MI_{RP} designates the procedure with a Rigid Penalty on the bones.

4 Results

The registration experiments are led using exactly the same parameters for both subject and phantom registration. They are conducted in two steps: first, the Dice scores between the CBCT organs and the propagated CT organs for both phantom and subject registration is calculated. Then, the measures of local estimation errors given by the phantom are provided.

4.1 Dice score

The evaluation of the registration is made using the Dice score to assess the relevance of the phantom compared to the real subject. The results are given in table 2. Two major remarks can be made regarding these results.

First, the Dice scores obtained with the subject and the phantom reach similar levels, even if some differences occur: rectum and seminal vesicles results are slightly better with the phantom, while bladder results seem better on the real subjects. In fact, during the phantom's registration, the drained out organs, which have been refilled with some random pixels taken from fat and muscles of the subject, disturb the registration procedure.

Nevertheless, the results seem promising. Indeed, regarding the different registration algorithms used, one can see that for both datasets, the Dice scores improve when a penalty term is added to the mutual information. On the other hand, by using only the Dice score for validation, it is not possible to choose a particular penalty term, since the results obtained with MI_{BE} and MI_{RP} are relatively close.

Table 2. Dice score obtained for the different organs and registration methods. The results obtained with the phantom are close from those obtained on the subject. The results obtained after the rigid regstration step are also given for comparison.

	Bladder		**Prostate**		**Rectum**		**Seminal Vesicles**	
	Phantom	**Subject**	**Phantom**	**Subject**	**Phantom**	**Subject**	**Phantom**	**Subject**
Rigid	0.70	0.73	0.67	0.76	0.54	0.58	0.34	0.36
MI	0.76	0.79	0.69	0.75	0.60	0.62	0.36	0.37
MI_{BE}	0.79	0.89	0.75	0.83	0.69	0.66	0.63	0.41
MI_{RP}	0.73	0.85	0.91	0.79	0.79	0.66	0.79	0.41

4.2 Local registration errors

The numerical phantom gives access to local validation results that cannot be obtained from the Dice score. Indeed, one can obtain the registration error, as a distance in mm, for each voxel on the surface of the phantom, since we know the exact transformation of the organs between the 2 images. In table 3 are reported the mean, minimum and maximum registration error in mm, for each organ and each registration method. While the

Dice score didn't allow to clearly separate MI_{BE} and MI_{RP} methods, these new error measures are very informative. They show the clear superiority of MI_{RP} compared to MI_{BE} with a total mean error for all the organs which is almost halved (3.76mm for MI_{BE} against 6.09mm for MI_{RP}). They also confirm that taking into account a penalty term during registration improves the results.

Table 3. Local registration errors (in mm), for the different organs and registration methods. This demonstrates the superiority of MI_{RP} compared to MI_{BE}.

		Bladder	**Prostate**	**Rectum**	**SV**
MI	**Mean**	**11.58**	**8.95**	**6.24**	**5.58**
	Min	0.10	0.12	0.08	0.11
	Max	21.42	16.73	15.36	11.22
MI_{BE}	**Mean**	**11.62**	**4.62**	**5.10**	**3.02**
	Min	0.09	0.05	0.06	0.05
	Max	20.32	8.30	12.52	5.16
MI_{RP}	**Mean**	**8.19**	**1.88**	**2.72**	**2.25**
	Min	0.08	0.01	0.02	0.01
	Max	14.94	3.41	6.07	3.06

5 Discussion and conclusion

In this paper, we have presented a numerical phantom of the pelvic structures for CT/CBCT image registration evaluation.

This phantom aims to be a complement to the classical Dice coefficient which do not evaluate the local matching of the organs, on which relies the cumulated dose computation. We showed that this phantom is able to differentiate registration algorithms that cannot be characterized with the use of the Dice score. It especially gives access to a precious information concerning the deformations estimated during registration. Indeed, with its use, the local motion of every voxel on the surface of the phantom can be evaluated precisely.

Regarding the conclusions we can get from the registration evaluation, although the experiments were performed on a reduced data set, it seems that a registration scheme including a rigid penalty term on the bones can produce better results than the traditionnal scheme or the one including a bending energy. This has to be confirmed on a larger dataset, and this will be the object of our future work. The 2 regularization terms given here could also be combined in order to obtain an even better result.

It would also be important to build a phantom which could be closer to a real patient, in order to be able to use affine registration to fill the rectum and seminal vesicles. For that purpose, we plan to generate a patient specific phantom that would take into account the geometrical particularity of each subject.

Acknowledgments

This work was partially funded by the french research agency (ANR): TIGRE project n°ANR-09-BLAN-0378-01.

References

1. Greene, W., Chelikani, S., Purushothaman, K., Knisely, J., Chen, Z., Papademetris, X., Staib, L., Duncan, J.: Constrained non-rigid registration for use in image-guided adaptive radiotherapy. Medical image analysis **13**(5) (2009) 809–817
2. Lu, C., Chelikani, S., Papademetris, X., Knisely, J.P., Milosevic, M.F., Chen, Z., Jaffray, D.A., Staib, L.H., Duncan, J.S.: An integrated approach to segmentation and nonrigid registration for application in image-guided pelvic radiotherapy. Medical Image Analysis **15**(5) (2011) 772–785
3. Rohlfing, T.: Image similarity and tissue overlaps as surrogates for image registration accuracy: Widely used but unreliable. IEEE Transactions on Medical Imaging **31**(2) (2012) 153–163
4. Paganelli, C., Peroni, M., Baroni, G., Riboldi, M.: Validation of deformable registration in adaptive radiation therapy with scale invariant feature transform. In: International Symposium on Biomedical Imaging. (2012)
5. Hensel, J.M., Menard, C., Chung, P.W.M., Milosevic, M.F., Kirilova, A., Moseley, J.L., Haider, M.A., Brock, K.K.: Development of multiorgan finite Element-Based prostate deformation model enabling registration of endorectal coil magnetic resonance imaging for radiotherapy planning. Internationl Journal Radiation Oncology Biology Physics **68**(5) (2007) 1522–1528
6. Chai, X., van Herk, M., van de Kamer, J.B., Hulshof, M.C., Remeijer, P., Lotz, H.T., Bel, A.: Finite element based bladder modeling for image-guided radiotherapy of bladder cancer. Medical physics **38**(1) (January 2011) 142–150
7. Boubaker, M.B., Haboussi, M., Ganghoffer, J.F., Aletti, P.: Finite element simulation of interactions between pelvic organs: Predictive model of the prostate motion in the context of radiotherapy. Journal of Biomechanics **42**(12) (August 2009) 1862–1868
8. Klein, S., Staring, M., Murphy, K., Viergever, M., Pluim, J.: elastix: a toolbox for intensity-based medical image registration. IEEE Transactions on Medical Imaging **29**(1) (2010) 196 – 205
9. Thévenaz, P., Unser, M.: Spline pyramids for inter-modal image registration using mutual information. In: Proceedings of the SPIE Conference on Mathematical Imaging: Wavelet Applications in Signal and Image Processing V. Volume 3169., San Diego CA, USA (1997) 236–247
10. Mattes, D., Haynor, D.R., Vesselle, H., Lewellen, T.K., Eubank, W.: PET-CT image registration in the chest using free-form deformations. IEEE Transactions on Medical Imaging **22**(1) (2003) 120–128
11. Rueckert, D., Sonoda, L., Hayes, C., Hill, D., Leach, M., Hawkes, D.: Nonrigid registration using Free-Form Deformations: Application to breast MR images. IEEE Transactions on Medical Imaging **18**(8) (1999) 712–721
12. Klein, S., Pluim, J., Staring, M., Viergever, M.: Adaptive stochastic gradient descent optimisation for image registration. International Journal of Computer Vision **81**(3) (2009) 227–239
13. Staring, M., Klein, S., Pluim, J.: A Rigidity Penalty Term for Nonrigid Registration. Medical Physics **34**(11) (November 2007) 4098 – 4108

Computerized Determination of Robust Beam Directions Against Patient Setup Errors in Hadron Particle Therapy

Hidetaka Arimura[1*], Genyu Kakiuchi[1], Yoshiyuki Shioyama[1], Shin-ichi Minohara[2]
Asumi Mizoguchi[3], Katsumasa Nakamura[1], Yasuhiko Nakamura[4], Hiroshi Honda[1]
Fukai Toyofuku[1], Masafumi Ohki[1], Hideki Hirata[1]

[1]Graduate School of Medical Sciences, Kyushu University, Fukuoka, Japan
[2]Kanagawa Cancer Center, Yokohama, Japan
[3]Kurume University Hospital, Kurume, Japan
[4]Kyushu University Hospital, Fukuoka, Japan

Abstract. We have proposed a computerized method for determination of robust beam directions against patient setup errors using electron density (ED)-based beam's eye view (BEV) in hadron particle therapy. The basic idea of our proposed method was to find the robust beam directions, whose ED-based BEV image has spatial fluctuations with low special frequency and small amplitude. The proposed method was applied to four head and neck cancer patients for evaluation of the proposed method. As a preliminary result, radiation oncologists agreed with most beam directions, which seem to be robust against patient setup errors, suggested by the proposed method. Our proposed method could be feasible to determine the robust beam directions against patient setup errors in hadron particle therapy.

Keywords: hadron particle therapy, robust beam direction, electron density (ED)-based beam's eye view (BEV) image, Fourier analysis

1 Introduction

Proton therapy or heavy ion therapy (carbon ion) has the physical ability to increase the high dose delivered to tumors while achieving a very low dose to normal tissue [1,2]. In particular, the highly-ionizing property of the heavy ion charged particles, i.e., higher linear energy transfer (LET), leads to eventual tumor cell death with higher tumor control probability than conventional radiotherapy of X-rays or electrons from the biological point of view.

In the hadron particle therapy, the distal end shape of dose distribution is modulated by a passive or active beam shaping method according to beam's eye view (BEV) of a 3D electron density (ED) map of a computed tomography (CT) image for each patient. However, the accurate dose distributions produced by the hadron particles

*E-mail: arimurah@med.kyushu-u.ac.jp

adfa, p. 1, 2011.

may be very sensitive to patient setup errors [3-9] occurring in a lateral direction orthogonal to the beam direction. If the patient setup errors are not taken into account during the treatment planning, the actual dose distribution that would occur in the patient during treatment could be strongly degraded compared with the planned dose distribution. In other words, due to patient setup errors, the distal end of the dose distribution in a beam direction could not be fitted with that of a tumor shape if the ED-based BEV in the beam direction changed more abruptly (high frequency fluctuation) with large amplitude fluctuation. This incident could lead to significant tumor underdose, but fatal overdose in organs at risk.

The goal in this study was to develop a computerized method for determination of robust beam directions against the patient setup errors based on the ED-based BEVs in the beam direction in the hadron therapy.

2 Materials and methods

2.1 Overall procedure

The proposed method mainly consisted of the following two steps: (1) production of a beam's eye view (BEV) image by projecting a 3D electron density image from a particle source to a planning target volume (PTV) distal end, (2) determination of robust beam directions against patient setup errors by using the slope of the power spectrum.

2.2 Clinical cases

Radiation treatment planning (RTP)-CT (referred to as planning CT) images of four head and neck cancer patients (ages: 48-85; median: 64.5) who had undergone conventional x-ray radiotherapy at our institution were selected for determination of the robust beam directions. All patients were scanned to acquire planning CT images (pixel size: 0.59 mm x 0.59 mm, depth bits per pixel: 16) using a 4-slice CT scanner (Mx 8000, Philips, Amsterdam, The Netherlands) with a slice thickness of 3.0 mm. Contours of clinical target volumes (CTV) of head and neck cancers were manually outlined by radiation oncologists on the planning CT images using a commercially available RTP system (Eclipse, Varian Medical Systems Inc., Palo Alto, USA).

2.3 Determination of robust beam directions against patient setup errors by using the slope of the power spectrum

The fundamental idea of our proposed method was to find the robust beam directions whose ED-based BEV images had spatial fluctuations with low spatial frequency and small amplitude. A BEV image was produced by projecting a 3D electron density image in a beam direction from a particle source to the distal end of a planning target

volume (PTV). Power spectra of the ED-based BEV images in all directions, i.e., 0 to 355 degrees, with an interval of 5 degrees were calculated for evaluation of the spatial fluctuations in the ED-based BEV images in a beam direction. We assumed that as the average spatial frequency and amplitude of the fluctuation in the ED-based BEV images in a beam direction become lower and smaller, respectively, the absolute value of the slope of the power spectrum becomes larger. Therefore, the slopes of one-order polynomial of the power spectra were calculated for determination of the robust beam directions.

Prior to calculation of the power spectral images, the ED-based BEV images were preprocessed as follows. First, the pixel values outside the irradiation field were assigned the average pixel value of the ED-based BEV inside the simulated irradiation field for decreasing the difference in the pixel value between inside and outside of the irradiation field. Second, a Gaussian filter was applied to inner and outer narrow bands (10 pixels) apart from the edge of the ED-based BEV for reducing the higher frequency components in the power spectrum, which were not related to the ED-based BEV. Third, a mean value in the ED-based BEV image was subtracted from the image to remove the influence of the mean value of the power spectral image.

Fourth, a power spectral image was calculated by using two-dimensional Fourier transformation from the preprocessed image. The power spectral image in the Cartesian coordinate system was converted to the polar coordinate system, which has the horizontal axis of the angle and the vertical axis of the spatial frequency. The power spectral image was integrated over a range of angles from 0 to 360 degrees to calculate the slope of an average power spectrum by using the following equation:

$$G(f) = \int_0^{360} \ln P(f,\theta) d\theta \ , \qquad (1)$$

where f is the spatial frequency (mm-1), and θ is the angle (degree) in the power spectral image. The slope of the average power spectrum was evaluated as the slope of a one-order polynomial of the power spectrum from 0.0195 mm-1 to a Nyquist frequency, which was calculated by a least square method. The slopes were calculated in all directions (0 to 355 degrees) with an interval of 5 degrees. Finally, the robust beam directions against patient setup errors were determined by selecting the directions corresponding to the several largest gradients of average power spectra for all beam directions. Figure 1 shows the resulting images in the major steps of the proposed method.

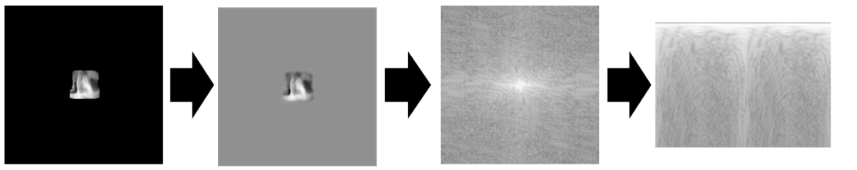

Fig. 1. Resulting images in the major steps of the proposed method.

3 Results and discussion

We applied the proposed method to four head and neck cancer cases and detected the beam directions. Nine beams of 13 beams (69%), which were used for the four patients in clinical practice, would be theoretically acceptable from the robustness point of view against the patient setup error. Figure 1 shows an example of the slope of the average power spectra as a function of beam direction, and the detected beam directions of 0 to 355 degrees are indicated by blue lines. Figure 2 shows the robust beam directions determined by the proposed method on three CT slices for a case. Each red region shows a PTV region, and each light blue region shows the beam path. In this case, 125, 130, and 135 degrees were considered as the robust beam directions. In a discussion of the results with radiological oncologists, all the oncologists agreed with most of the optimum beam directions determined by the proposed method. The suggested beam directions were close to those employed as one of beam directions in clinical practice.

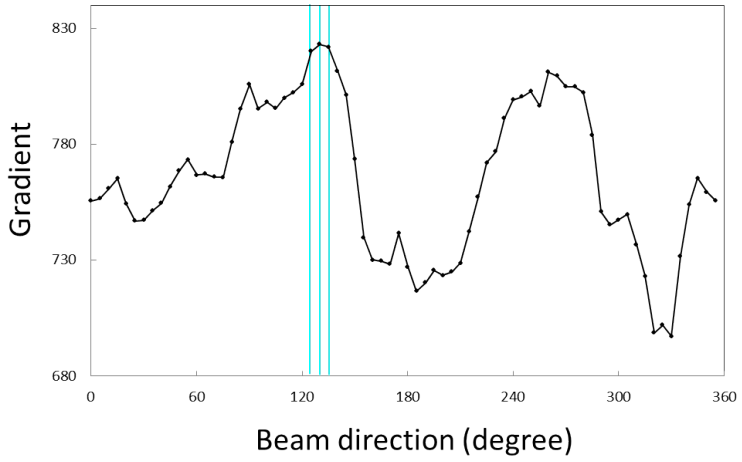

Fig. 2. Slope of average power spectral value as a function of the beam direction (0 to 355 degree).

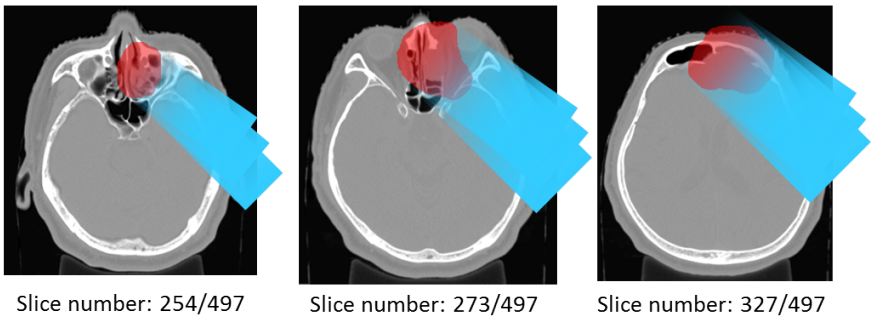

Fig. 3. Robust beam directions determined by the proposed method on three CT slices for a case by selecting the directions corresponding to the three largest slopes of average power spectra for all beam directions.

4 Conclusions

We have proposed a computerized determination of robust beam directions against patient setup errors based on Fourier analysis of ED-based BEVs in hadron particle therapy. The proposed method could be useful to select the robust beam directions against patient setup errors in hadron particle therapy such as carbon ion therapy.

Acknowledgments

The authors are grateful to all members of the Arimura Laboratory (http://www.shs.kyushu-u.ac.jp/~arimura), whose comments made an enormous contribution to this chapter. This research was partially supported by the Ministry of Education, Science, Sports and Culture, Grant-in-Aid for Scientific Research (C), 22611011, Grant-in-Aid for Scientific Research on Innovative Areas, 24103707, 2012.

References

1. Okada T, Kamada T, Tsuji H, Mizoe JE, Baba M, Kato S, Yamada S, Sugahara S, Yasuda S, Yamamoto N, Imai R, Hasegawa A, Imada H, Kiyohara H, Jingu K, Shinoto M, Tsujii H. (2010) Carbon ion radiotherapy: clinical experiences at National Institute of Radiological Science (NIRS). J Radiat Res 51: 355-64
2. Minohara S, Fukuda S, Kanematsu N, Takei Y, Furukawa T, Inaniwa T, Matsufuji N, Mori S, Noda K. (2010) Recent innovations in carbon-ion radiotherapy. J Radiat Res 51: 385-92
3. Hui Z, Zhang X, Starkschall G, Li Y, Mohan R, Komaki R, Cox JD, Chang JY (2008) Effects of interfractional motion and anatomic changes on proton therapy dose distribution in lung cancer. Int J Radiat Oncol Biol Phys 72: 1385-1395
4. Inaniwa T, Kanematsu N, Furukawa T, Hasegawa A (2011) A robust algorithm of intensity modulated proton therapy for critical tissue sparing and target coverage. Phys Med Biol 56: 4749-4770

5. Lomax AJ. (2008) Intensity modulated proton therapy and its sensitivity to treatment uncertainties 2: the potential effects of inter-fraction and inter-field motions. Phys Med Biol 53: 1043-1056
6. Pflugfelder D, Wilkens JJ, Oelfke U (2008) Worst case optimization: a method to account for uncertainties in optimization of intensity modulated proton therapy. Phys Med Biol 53: 1689-1700
7. Sejpal SV, Amos RA, Bluett JB, Levy LB, Kudchadker RJ, Johnson J, Choi S, Lee AK (2009) Dosimetric changes resulting from patient rotational setup errors in proton therapy prostate plans. Int J Radiat Oncol Biol Phys 75: 40-48
8. Unkelbach J, Bortfeld T, Martin BC, Soukup M (2009) Reducing the sensitivity of IMPT treatment plans to setup errors and range uncertainties via probabilistic treatment planning. Med Phys 36: 149-163
9. Zhang X, Dong L, Lee AK, Cox JD, Kuban DA, Zhu RX, Wang X, Li Y, Newhauser WD, Gillin M, Mohan R (2007) Effect of anatomic motion on proton therapy dose distribution in prostate cancer treatment. Int J Radiat Oncol Biol Phys 67: 620-629

Explaining relationships between local dose and rectal toxicity in prostate cancer radiotherapy with voxel-based population analysis

Oscar Acosta[1,2], Gaël Dréan[1,2], Juan David Ospina[1,2,4], Antoine Simon[1,2], Pascal Haigron[1,2], and Renaud de Crevoisier[1,2,3]

[1] INSERM, U 1099, Rennes, F-35000, France
[2] Université de Rennes 1, LTSI, F-35000, France
Oscar.Acosta@univ.rennes1.fr
[3] Département de Radiothérapie, Centre Eugène Marquis, Rennes, F-35000, France
[4] School of Statistics, Universidad Nacional de Colombia, Campus Medellin, Colombia

Abstract. Intensity Modulated Radiotherapy (IMRT) allows delivering of highly conformal dose to complex targets, implying nevertheless the choice of optimal constraints for the organs at risk (OAR) with the aim of reducing toxicity. To estimate the risk of toxicity, current predictive models stand on the dose-volume histograms (DVH) whose main drawback is the lack of spatial accuracy as they consider the organs as a whole volume and thus ignore the heterogeneous intra-organ radio-sensitivity. A framework for finding relationships between local dose and toxicity is proposed here. In this approach, the planned dose distributions are registered together on a common coordinate system and compared across a population at a voxel level, thereby allowing the highlighting of 3D anatomical patterns which may be in part responsible of toxicity. We demonstrated here the value of the approach by explaining rectal toxicity in prostate cancer radiotherapy (PCRT). 116 patients with 31 month median follow-up were considered. They received a total dose of 80 Gy in the prostate by IMRT. When analyzing rectal toxicity, significant difference of dose was found in large regions within the anterior wall close to the prostate (1cm). This promising voxel-wise approach allowed the highlighting of regions that may be involved in rectal toxicity.

1 Introduction

Radiation therapy (RT) is a commonly prescribed treatment for people diagnosed with prostate cancer which has proven to be efficient for tumor control. Several strategies have been recently developed to increase local control, particularly by increasing the dose of radiation demonstrating a close dose-effect relationship [1,2]. However, in prostate cancer radiotherapy (PCRT), rectal and urinary toxicity occurrences, that are frequent with standard prescribed doses (70 Gy), may increase for higher doses. With the precision of the accelerators steadily growing (ARC-Therapy, cyberknife), the possibilities for achieving better control by increasing the dose are available but at the expense of the risk of toxicity if efficient adaptive plannings allowing the inclusion of accurate predictive models are not devised.

The prediction of complications as a consequence of the irradiation has been largely treated in the literature [3] [4]. These predictions are commonly based on the planned

dose distribution using the dose-volume histograms (DVH) [5] within radiobiological Normal Tissue Complication Probability (NTCP) models [6,7,8]. NTCP models were proposed in the early 1980s to estimate the risk of toxicity, based on the dose distribution and the irradiated volume of the structures at risk. Different studies have shown a correlation between dose, volume and rectal toxicity [9,10,11,12,13,14]. However, current DVH-based models for prediction of toxicity exhibit many limitations. Firstly, they do not implicitly integrate individual's specificities (such as the medical history, ...) and concomitant treatments (chemotherapy, androgen deprivation), which may differ across a population. Secondly, they lack spatial accuracy since they are not able to correlate the treatment outcome with spatial patterns of dose thereby considering homogeneous radiosensitive organs. Indeed, the subtle correlation that may exist between local dose and toxicity may not be detected if the rich three-dimensional dose distribution is reduced and represented as a DVH. The waste may be even worse when the DVH is reduced to a single value such as the effective dose (D_{eff}) or the Equivalent Uniform Dose (EUD), which has also proved to be correlated with the risk of toxicity [15,14]. A tri-dimensional cartography depicting sub-regions presenting higher risk of damage will help to define more accurate organ constraints in terms of local dose.

The notion of spatiality and local dose related with toxicity has been raised in previous works [16] either with a parametric description of the dose distribution [17] [18] or within a voxel-based approach [19] however very approximative in terms of both anatomical matching and therefore dose mapping. In this particular work we are addressing the question of producing a 3D cartography (a set of parameters $\Phi(x)$, $x \in 3D$), which may explain the local dose-toxicity relationships from a voxel-based population analysis. The framework as depicted in fig 1 lies on non-rigid registration.

The particularity here is to take full advantage of the 3D dose distributions thereby explaining toxicity at a local level through voxel-wise comparisons. We use a non-rigid registration strategy which allows the inter-individual mapping of doses in a single coordinate system. This approach advantageously exploits information available at the planning, namely the 3D anatomical data, 3D organ delineations and TPS planned doses. It stands on a non-rigid registration scheme which combines organs delineations with CT scans in order to achieve a better organ matching across all the individuals.

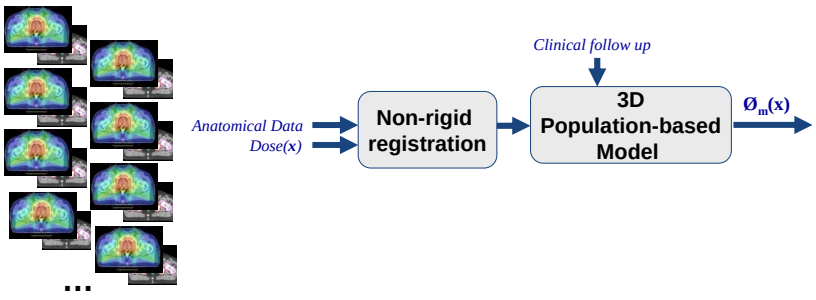

Fig. 1. 3D population-based approach. It includes inter-individual non-rigid registration for dose mapping before population comparisons.

2 Materials and Methods

The main steps of the method are depicted in figure 2. i) The inter-individual CT and contour delineations are non-rigidly registered towards a single template (common coordinate system), ii) the planned doses distributions are mapped towards the template by applying the computed transformations and iii) a voxel-wise comparison of the mapped doses is performed in the common coordinate system (in this work, two sampled t-tests). The output is a 3D map highlighting voxels where the differences are significant between two groups.

2.1 Data

116 individuals treated for prostate cancer with IMRT and a three-year follow-up were selected. The patients underwent a planning CT scan before the treatment. The size of the images in the axial plane was 512*512 pixels with 1 mm resolution 2-mm thick slices. For each patient, the bladder, rectum, prostate and seminal vesicles (SV) were manually contoured by the same expert. For each patient, the prescribed dose was computed in a standard Treatment Planning System (TPS) step and then resampled into the CT native space. The patients received a total dose of 80 Gy in the prostate. 2nd year-rectal toxicity was included in the analysis using the SOMALENT classification and bleeding scoring (at least 1 episode).

2.2 Registration

In order for the voxel-wise comparisons to be meaningful in terms of dose-effect relationships, anatomical correspondences across the population were previously computed through non-rigid registrations and dose mappings of all individuals towards a single template.

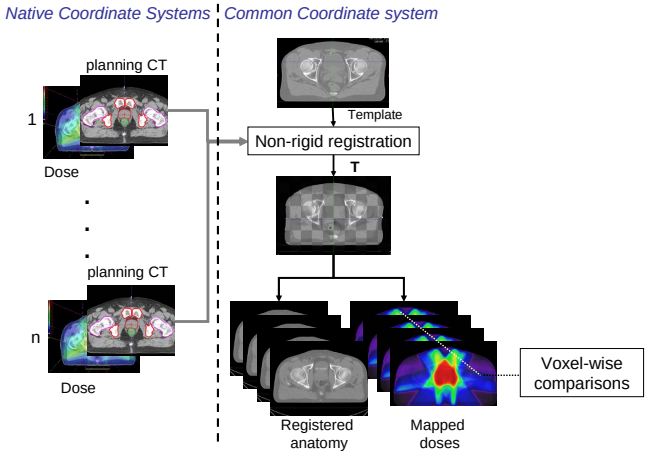

Fig. 2. Dose mapping using a non-rigid registration (NRR) approach.

Registering inter-individual CTs is particularly challenging because of the poor soft-tissue contrast, the large inter-individual variability and the filling differences of the bladder and the rectum [20]. In this context, it has been shown that a pure intensity-based registration is not accurate as required in population analysis and may lead to local errors [21]. If all the complementary knowledge about the individuals' anatomy is used, the performance of the registration would considerably improve. To this end, we developed an organ-driven non-rigid registration strategy which yields an accurate matching between organs in the common coordinate system (CS). In this study, the template was selected as a representative individual.

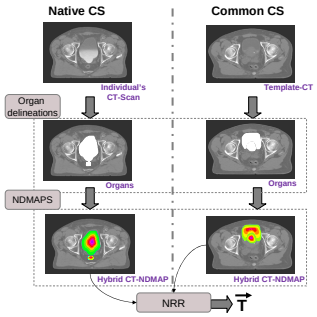

Fig. 3. Hybrid Non-rigid registration (NRR) approach bringing 3D doses from their native Coordinate System (CS) towards the Common CS. After organ delineation, Normalized Distance Maps (NDMAPS) are computed and combined with the CT scan to be registered. The result is the transformation used to fartherly map the dose.

The methodology exploits both the CT scans and the organ delineations as depicted in fig. 3. Thus, normalized Distance Maps (NDMAPS) for each of manually-segmented organs (prostate, bladder and rectum) were obtained as follows: For each individual's organ, i) an euclidean distance map was computed, ii) the distance maps of both the individual and the template were multiplied by the maximum distance of the template's and the individual's maps, respectively. Those maps replaced the corresponding individual's organs within the CT scan yielding a new hybrid image where the organs appear clearly defined. Finally, the diffeomorphic demons algorithm [22] was applied to register those images towards the template.

2.3 Voxel-based Analysis

According to predefined inclusion criteria, comparisons between non-toxic individuals and individuals with different toxicity scores were performed. For each comparison, two-sampled t-tests at a voxel-basis, produced 3D maps for both the dose differences and the p-values. Voxels where the differences were significant between the groups (p-values < 0.01) were characterized in terms of: absolute volume, mean dose difference and their localization in the rectum, namely the distance of the region to the prostate and the seminal vesicles surfaces as shown in Fig 3.

3 Validation and Results

3.1 Registration

To assess the quality of the registration, the Dice Similarity Coefficient defined as $DSC = 2\left(\frac{S_C \cap S_R}{|S_C|+|S_R|}\right)$ was computed between each individual's registered rectum and the corresponding organ in the common coordinate system. 30 individuals were randomly selected from the data base and leave-one-out cross validation was performed thereby obtaining averaged DSC. Results were compared with different intensity registration strategies [23,24,22]as illustrated in Fig. 4 illustrates the results.

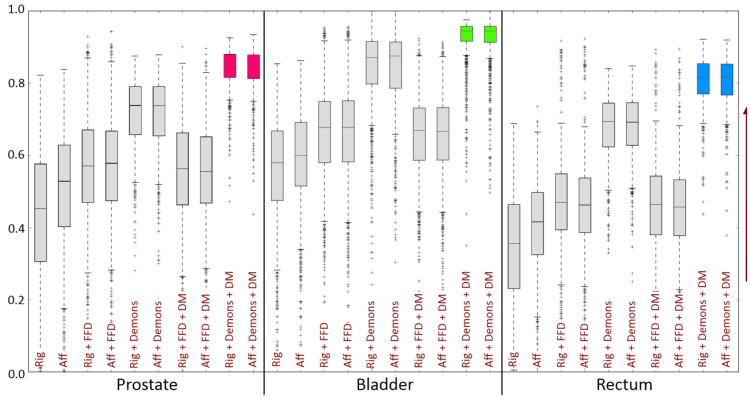

Fig. 4. Dice score comparisons between different intensity-based registration strategies and the hybrid approach used in this paper. The different strategies result from a combination of Rigid, Affine [23], Free Form Deformation (FFD) [24] and Demons [22] non-rigid registration.

Considering the whole population (116 patients), the median dice score was 0.75 $\pm$0.12 for the rectum and 0.92 $\pm$0.13 for the bladder. Fig. 5 depicts an example of the dose mapping from the native coordinate system to the common coordinate system (template) through the different steps of this method.(fig. 5(a)), individual's CT, (fig. 5(b)) manual segmentations on the template (fig. 5(c)) individual's planned dose distribution and (fig. 5(d)) mapped dose distributions in the template CS.

3.2 Voxel-based comparisons

The statistical analysis was conducted only on the properly registered patients (Dice score $\geq$ 0.7), leading to the inclusion of 74 patients for the rectal toxicity analysis. Median follow-up was 31 months (6 to 64). Grade 1 and 2 rectal acute toxicity rates were 26% and 4% respectively. Two year rectal toxicity (> grade 2) and bleeding rates were: 9% (95% CI: 3-14) and 20% (95% CI: 12-27). As shown in table 1 significant differences of dose were found in large regions. More than 90% of them were within the first 1cm (anterior wall). These results suggest that rectal bleeding is more related with higher dose in regions close to the prostate. The more sensitive area seems to be between 10 and 15mm. fig. 6

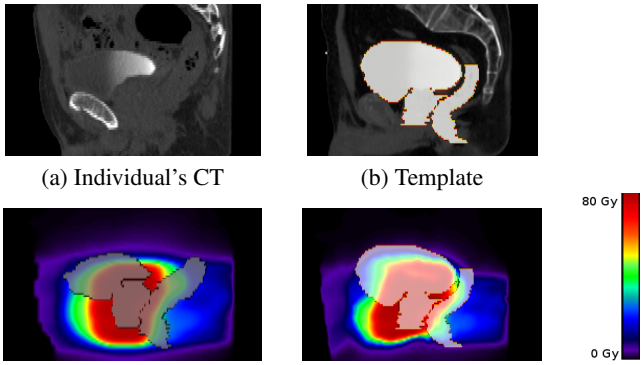

(a) Individual's CT (b) Template

(d) Individual's dose (e) Dose warped to the template

Fig. 5. 3D Dose mapping through an organ-driven non-rigid registration methodology. (a) A typical individual's CT; (b) Manually Segmented organs on the template; (c) Individual's TPS planned dose in the native CS; (d) Dose mapped to the template CS.

Significant (p<0.01) voxel characteristics voxel characteristics		Rectal Bleeding (2 years)		Grade 2 rectal toxicity (2years)	
Absolute Volume(mm3)		1555.07 (4.45%)		2913.02 (8.33%)	
Dose Difference		8.06		10.16	
Distribution (%) of the voxels	5mm	16.02	6.35Gy	48.87	10.33Gy
by the distance of the voxel	10mm	96.65	7.98Gy	94.27	10.21Gy
from the prostate	15mm	99.65	8.05Gy	94.64	10.22Gy
and the seminal vesicles	20mm	100	8.06Gy	94.64	10.22Gy
	30mm	100	8.06Gy	94.64	10.22Gy

Table 1. voxel-wise comparison: characterization in terms of absolute volume, mean dose difference and localization in the rectum, defined as the distance to the prostate and the seminal vesicles surfaces.

4 Discussion and conclusion

We proposed in this paper a methodological framework based on non-rigid registration aimed at determining the local dose-effect relationship in PCRT, thereby helping to unravel the heterogeneous intra-organ radio-sensitivity to predict toxicity. Further work considers the inclusion of individuals clinical variables that may also be involved in toxicity (age, concomitant treatments, etc). Another issue to take into account is the differences between the planned and delivered doses, as during the treatment the organs at risk may deform or displace with respect to the initial conditions at the planning step.

To a large extent, determining the heterogeneous intra-organ sensitivity across a population, combined with patient-specific information in an inverse IMRT planning will allow to produce a personalized treatment with high local control and reduced toxicity. This general framework may be extended in order to adapt the ongoing treatment and thereby take into account not only data from a model but also integrate the dynamic individual's specificities (i.e. tumour response, anatomical modifications) as depicted

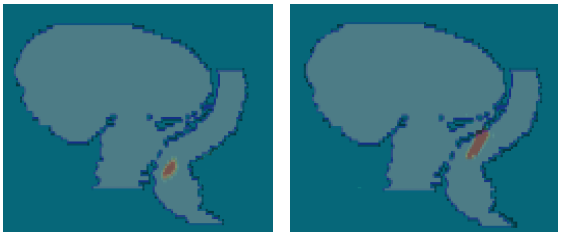

(a) (b)

Fig. 6. Results of voxel-wise analysis in the template: regions where the difference in dose are significant (p-values < 0.01) for rectal bleeding at 2 years (a) and rectal toxicity at 2 years (b).

in fig. 7. In this framework for adaptive radiotherapy, the set of parametres Φ extracted from population data may be then combined with the individual's parameters $\phi_p(t)$, which may change during the treatment (t) in order to adapt the therapy.

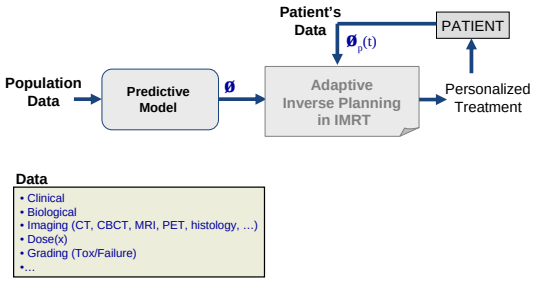

Fig. 7. General Adaptive Inverse Planning considering population data and dynamic individual's specificities ($\phi_p(t)$=anatomical modifications, tumor response).

References

1. Beckendorf, *et al.*: multicenter study on dose escalation with conformal and conventional radiotherapy for the treatment of localized prostatic cancer. preliminary results of tolerance and quality of life. Prog Urol **11**(2) (Apr 2001) 264–276
2. Zietman,, *et al.*: Randomized trial comparing conventional-dose with high-dose conformal radiation therapy in early-stage adenocarcinoma of the prostate: long-term results from proton radiation oncology group/american college of radiology 95-09. J Clin Oncol **28**(7) (Mar 2010) 1106–1111
3. Fiorino, C., Rancati, T., Valdagni, R.: Predictive models of toxicity in external radiotherapy: dosimetric issues. Cancer **115**(13 Suppl) (Jul 2009) 3135–3140
4. de Crevoisier, R., Fiorino, C., Dubray, B.: Dosimetric factors predictive of late toxicity in prostate cancer radiotherapy. Cancer Radiother **14**(6-7) (Oct 2010) 460–468
5. Ting, J.Y., *et al.*: Dose-volume histograms for bladder and rectum. Int J Radiat Oncol Biol Phys **38**(5) (Jul 1997) 1105–1111
6. Jensen, I., *et al.*: Radiobiological impact of reduced margins and treatment technique for prostate cancer in terms of tumor control probability (TCP) and normal tissue complication probability (NTCP). Med Dosim (May 2010)

7. Cambria, R., *et al.*: Evaluation of late rectal toxicity after conformal radiotherapy for prostate cancer: a comparison between dose-volume constraints and NTCP use. Strahlenther Onkol **185**(6) (Jun 2009) 384–389
8. Grigorov, G.N., *et al.*: IMRT: improvement in treatment planning efficiency using NTCP calculation independent of the dose-volume-histogram. Med Phys **33**(5) (May 2006) 1250–1258
9. Sohn, M., Alber, M., Yan, D.: Principal component analysis-based pattern analysis of dose-volume histograms and influence on rectal toxicity. Int J Radiat Oncol Biol Phys **69**(1) (Sep 2007) 230–239
10. Fiorino, C., *et al.*: Rectum contouring variability in patients treated for prostate cancer: impact on rectum dose-volume histograms and normal tissue complication probability. Radiother Oncol **63**(3) (Jun 2002) 249–255
11. Fiorino, C., *et al.*: Relationships between dvhs and late rectal bleeding after radiotherapy for prostate cancer: analysis of a large group of patients pooled from three institutions. Radiother Oncol **64**(1) (Jul 2002) 1–12
12. Marzi, S., *et al.*: Relationships between rectal wall dose-volume constraints and radiobiologic indices of toxicity for patients with prostate cancer. Int J Radiat Oncol Biol Phys **68**(1) (May 2007) 41–49
13. Benk, V.A., *et al.*: Late rectal bleeding following combined x-ray and proton high dose irradiation for patients with stages t3-t4 prostate carcinoma. Int J Radiat Oncol Biol Phys **26**(3) (Jun 1993) 551–557
14. Rancati, T., *et al.*: Fitting late rectal bleeding data using different NTCP models: results from an italian multi-centric study (airopros0101). Radiother Oncol **73**(1) (Oct 2004) 21–32
15. Schwarz, M., Lebesque, *et al.*: Sensitivity of treatment plan optimisation for prostate cancer using the equivalent uniform dose (eud) with respect to the rectal wall volume parameter. Radiother Oncol **73**(2) (Nov 2004) 209–218
16. Kupchak, C., Battista, J., Dyk, J.V.: Experience-driven dose-volume histogram maps of NTCP risk as an aid for radiation treatment plan selection and optimization. Med Phys **35**(1) (Jan 2008) 333–343
17. Buettner, F., *et al.*: Assessing correlations between the spatial distribution of the dose to the rectal wall and late rectal toxicity after prostate radiotherapy: an analysis of data from the mrc rt01 trial (isrctn 47772397). Physics in Medicine and Biology **54**(21) (2009) 6535
18. Buettner, F., Gulliford, *et al.*: Modeling late rectal toxicities based on a parameterized representation of the 3d dose distribution. Physics in Medicine and Biology **56**(7) (2011) 2103
19. Heemsbergen, W.D., *et al.*: Urinary obstruction in prostate cancer patients from the dutch trial (68 gy vs. 78 gy): Relationships with local dose, acute effects, and baseline characteristics. Int J Radiat Oncol Biol Phys (Jan 2010)
20. Acosta, O., *et al.*: Evaluation of multi-atlas-based segmentation of ct scans in prostate cancer radiotherapy. In: Biomedical Imaging: From Nano to Macro, 2011 IEEE International Symposium on. (30 2011-april 2 2011) 1966 –1969
21. Dréan, G., Acosta, *et al.*: Evaluation of inter-individual pelvic ct-scans registration. IRBM 32 (2011) 288–92 –
22. Vercauteren, T., Pennec, *et al.*.: Non-parametric diffeomorphic image registration with the demons algorithm. Med Image Comput Comput Assist Interv **10**(Pt 2) (2007) 319–326
23. Ourselin, S., Roche, *et al.*: Reconstructing a 3d structure from serial histological sections. Image and Vision Computing **19**(1-2) (2001) 25 – 31
24. Rueckert, D., Sonoda, *et al.*: Nonrigid registration using free-form deformations: Application to breast MR images. IEEE Transactions on Medical Imaging **18** (1999) 712–721

Phantom validation of optical soft tissue navigation for Brachytherapy

Christoph Otte[1], Gereon Hüttmann[2], György Kovacs[3], and Alexander Schlaefer[1,4]

[1] Institute for Robotics and Cognitive Systems, University of Lübeck, Lübeck
[2] Institute for Biomedical Optics, University of Lübeck, Lübeck
[3] Interdisciplinary Brachytherapy, University Clinics Schleswig Holstein, Lübeck
[4] Graduate School for Computing in Medicine and Life Sciences, University of Lübeck, Lübeck

Abstract. In high dose rate brachytherapy, needles are inserted into soft tissue and subsequently radioactive sources are used to deliver a high dose inside the target region. While this approach can achieve a steep dose gradient and offers a focused, organ sparing treatment, it also requires a careful positioning of the needles with respect to the tissue. We have previously proposed to use an optical fiber embedded in the needle to detect soft tissue deformation. To validate the approach, we have developed an experimental setup to compare the actual needle motion with the motion estimated via the fiber. Our results show a good agreement between actual and estimated motion, indicating that optical deformation detection through the needle is possible.

1 Introduction

In high dose rate (HDR) brachytherapy, needles are inserted into soft tissue and subsequently radioactive sources are used to deliver a high dose inside the target region. On the one hand, this approach can achieve a steep dose gradient and offers a focused, organ sparing treatment. On the other hand, it also requires a careful positioning of the needles with respect to the tissue, as the dose is highest in the direct proximity of the sources [1–3].

Different methods including gridlike templates and robotic needle drivers have been proposed for needle placement. One issue is the soft tissue deformation resulting from the insertion force [4]. One approach is modeling the needle tissue interaction [5], or to study the resulting force [6]. Clearly, image guidance can also help identifying tissue motion. However, sophisticated modalities like magnetic resonance imaging (MRI) are typically not available in brachytherapy settings. Moreover, imaging can be subject to artifacts caused be the needles, e.g., phantom echoes in ultrasound images.

We have previously proposed to embed an optical fiber into a brachytherapy needle to allow for optical coherence tomography (OCT) along the needle path [7]. Moreover, we have studied the feasibility of using Doppler data acquired through the needler to estimate the relative motion between needle tip and soft

tissue [8]. However, the actual validation of the approach requires measuring the tissue deformation caused by the needle. We present a phantom setup to measure the deformation and to compare the motion estimated from the Doppler data with the measurements.

2 Material and Methods

Optical coherence tomography (OCT) is an interferometric approach that can penetrate up to 3 mm into tissue, resulting in images with a depth resolution of better than 10 μm. While the images represent different scattering properties in the probe, OCT it can also be used to obtain Doppler data [9]. As the phase shift between subsequent A-scans is proportional to the relative velocity between fiber tip and scatter source, integrating over the velocities yields an estimate of the relative motion of the needle with respect to the tissue.

We use a bevel point tipped needle with an embedded optical fiber (Figure 1a) connected to an OCT-System (Callisto, Thorlabs) with a 1200 Hz A-scan rate. An industrial robot (Adept Viper s850) with a positioning accuracy of 30 µm is used to move the needle along its axis. Tissue motion is monitored using a Logitech Pro 9000 camera using the vcapg2-plugin for Matlab [10]. The camera's sensitivity was adapted to provide good contrast between needle and phantom structures.

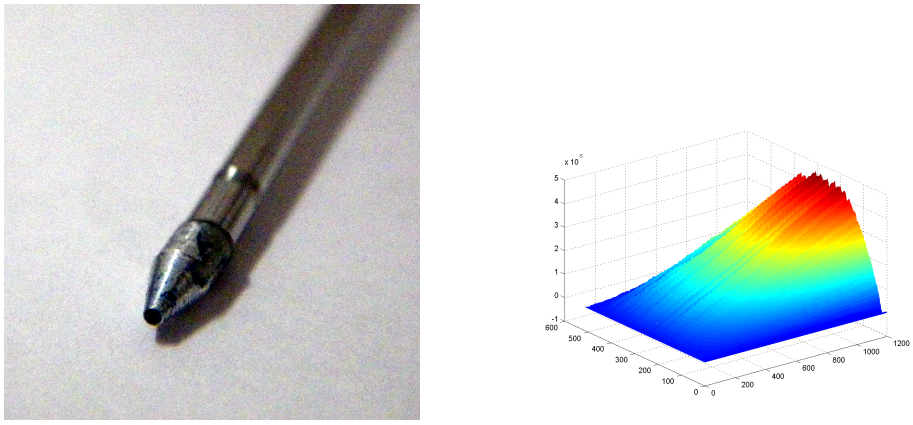

(a) (b)

Fig. 1: On the left the modified needle with the embedded fiber is shown (a). On the right an image of the relative motion profiles for different depth accumulated over one second of needle motion (b).

For our experiments we used phantoms made of gelatine. To obtain sufficient scattering, TiO_2 powder was added. However, typically gelatine shows little friction and hence little deformation after the initial penetration of the surface. To

induce and detect deformations we added layers of colored gelatine with a different stiffness, such that the needle tip and the layers are well visible in the camera images. The robot was configured to continuously move the needle with a speed of approximately 0.05 mm/s while OCT and camera images were recorded with 1200 Hz and 30 Hz, respectively. In a post-processing step, the camera images with maximum deformation of the gelatine layer were identified and the related time stamp defined the end point of the motion trace. The deformation was then estimated from the camera image by taking the needle as a reference, and the relative motion estimated by the OCT as well as the actual robot motion were determined from the recorded data.

As the OCT Doppler data can be considered as one-dimensional depth profiles of the relative velocity v_{rel} between tissue and needle tip, we need to decide in which depth to measure the motion. To this end we compute the accumulated motion for all depth and a windows of 1 s. Figure 1b shows the resulting motion profiles, which generally show a maximum approximately 300 pixels or 1 mm from the needle tip.

3 Results

Figures 2a and 2b show the deformation caused by the needle. The horizontal layer is gelatine with a higher stiffness, leading to the distinct deformation,

(a) (b)

Fig. 2: The left image shows the situation before the needle moved into the colored gelatine layer visible as a black horizontal bar (a). The right image illustrates the maximum deformation of the layer, this defines the endpoint for the measurements (b). The distance between the lower boundary of the layer in (a) and the needle tip in (b) is measured as an estimate for the deformation, it is approximately 3.28 mm.

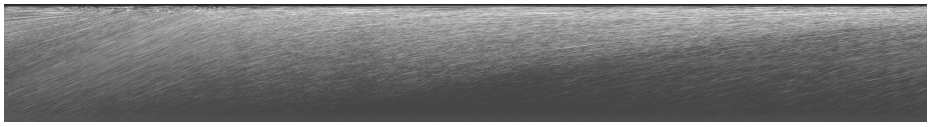

Fig. 3: An overview of the OCT A-scans at different time steps / needle positions, from left to right.

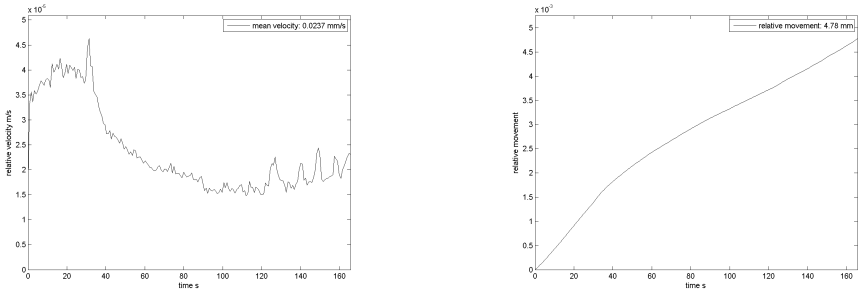

(a) (b)

Fig. 4: The left plot shows the velocity of material in front of the needle over time / needle position (a). The right plot shows the corresponding motion estimate (b).

which is approximately 3.28 mm in this case. In Figure 3 the OCT data recorded during the needle motion is summarized. Note that each column in the image corresponds to an A-scan showing the real part of the signal, i.e., the left hand side represents the situation before entering the layer and the last column on the left corresponds to the A-scan in the situation shown in Figure 2b. A careful look at the image reveals that there is a brighter region that gradually gets smaller on the left, indicating some compression.

The actual velocity of material in front of the needle and the resulting estimate of the relative motion are presented in Figures 4a and 4b, respectively. Note that the total motion through the gelatine is estimated as approximately 4.78 mm. The robot moved 8.16 mm while deformation of 3.28 mm and the estimated motion add to 8.06 mm

4 Discussion

Our experiments are preliminary in that they need to be repeated and the determination of the deformation from the images should be automated. Moreover, the scattering and absorption in actual tissue may affect ability to detection of motion in sufficient depth, where the smaller SNR typically leads to an underestimation of the Doppler signal [11].

However, the results still provide further indication that a precise estimation of the needle tip motion relative to soft tissue is possible using OCT Doppler data. Such information would be valuable when placing needles for brachytherapy or biopsies, where proper placement of the needle with respect to soft tissue is important. The methods is not affected by artifacts from other needles and the high sampling rate allows for real-time control, e.g., of robotic needle drivers.

References

1. Damore, S.J., Syed, A., Puthawala, A.A., Sharma, A.: Needle displacement during hdr brachytherapy in the treatment of prostate cancer. International Journal of Radiation Oncology **46**(5) (2000) 1205–1211
2. Nakamura, R., Ishiyama, H., Tanji, S., Satoh, T., Oikawa, H., Inatsu, W., Ehara, S., K., H.: Effects of ellipsoid prostate deformation on dose delivery during permanent interstitial brachytherapie. Brachytherapy **10**(3) (2011) 208–213
3. Yoshida, K., Yamazaki, H., Nose, T., Shiomi, H., Yoshida, M., Mikami, M., Takenaka, T., Kotsuma, T., E.Tanaka, Kuriyama, K., Harada, Y., Tohda, A., Yasunaga, Y., Oka, T.: Needle applicator displacement during high-dose-rate interstitial brachytherapy for prostate cancer. Brachytherapy **9**(1) (2010) 36–41
4. Lagerburg, V., Moerland, M.A., Lagendijk, J.J., Battermann, J.J.: Measurement of prostate rotation during insertion of needles for brachytherapy. Radiotherapy and Oncology **77**(3) (2005) 318–23
5. Alterovitz, R., Goldberg, K.Y., Pouliot, J., Hsu, I.C.J.: Sensorless motion planning for medical needle insertion in deformable tissues. IEEE Trans Inf Technol Biomed **13**(2) (Mar 2009) 217–225
6. Mahvash, M., Dupont, P.E.: Mechanics of dynamic needle insertion into a biological material. IEEE TRANSACTIONS ON BIOMEDICAL ENGINEERING **57**(4) (2010) 934 – 943
7. Schlaefer, A., Otte, C., Richter, L., Heinig, M., Bruder, R., Kovacz, G., Hüttman, G.: Towards high resolution image guided needle navigation in prostate brachytherapie. CARS 2010 **2010** (2010) 24–25
8. Otte, C., Hüttmann, G., Schlaefer, A.: Feasibiliy of optical detection of soft tissue deformation during needle insertion. In III, D.R.H., Wong, K.H., eds.: Medical Imaging 2012: Image-Guided Procedures, Robotic Interventions, and Modeling. Volume 8316. (2012)
9. Wang, R.K., Ma, Z.H., Kirkpatrick, S.J.: Tissue doppler optical coherence elastography for real time strain rate and strain mapping of soft tissue. Appl. Phys. Lett **89**(14) (2006) 144103–3
10. Kobayashi, K.: MATLAB Utilization Book. Shuwa System Co, Ltd. (2001)
11. Szkulmowska, A., Szkulmowski, M., Kowalczyk, A., Wojtkowski, M.: Phase-resolved doppler optical coherence tomography-limitations and improvements. Opt Let **33**(13) (2008) 1425–1427

Computer-assisted determination of the usable beam arrangement from similar treatment plans in stereotactic body radiotherapy

Taiki Magome[1, 2], Hidetaka Arimura[3], Yoshiyuki Shioyama[4], Asumi Mizoguchi[1]
Chiaki Tokunaga[1], Katsumasa Nakamura[5], Yasuhiko Nakamura[6], Hiroshi Honda[5]
Masafumi Ohki[3], Fukai Toyofuku[3], and Hideki Hirata[3]

[1]Department of Health Sciences, Graduate School of Medical Sciences, Kyushu University, Fukuoka 812-8582, Japan
[2]Research Fellow of the Japan Society for the Promotion of Science, Tokyo, Japan
[3]Department of Health Sciences, Faculty of Medical Sciences, Kyushu University, Fukuoka 812-8582, Japan
[4]Department of Heavy Particle Therapy and Radiation Oncology, Graduate School of Medical Sciences, Kyushu University, Fukuoka 812-8582, Japan
[5]Department of Clinical Radiology, Graduate School of Medical Sciences, Kyushu University, Fukuoka 812-8582, Japan
[6]Department of Medical Technology, Kyushu University Hospital, Fukuoka 812-8582, Japan

Abstract The goal of this study was to develop a computer-assisted treatment planning system for the stereotactic body radiation therapy (SBRT) based on several similar cases in a radiation treatment planning (RTP) database. Similar cases were automatically selected based on image features from the radiation treatment planning point of view. The beam angles were determined by registration of similar cases to an objective case with respect to lung regions using a linear registration technique. We applied the proposed method to 10 test cases by using an RTP database of 81 cases with lung cancer. As a result, the proposed method suggested usable beam arrangements, which might be equivalent to manual beam arrangements of cases in the RTP database. Therefore, the proposed method could be feasible for automated determination of beam arrangements in SBRT.

Keywords: Radiotherapy treatment planning, Similar treatment plans, Beam arrangement, Image features.

1 Introduction

With the recent advancement of radiation treatment technique, e.g., stereotactic body radiation therapy (SBRT), it has become possible to concentrate very large doses of radiation to tumors, and minimize the doses to surrounding organs by using multiple beams with coplanar and non-coplanar directions [1-3]. Therefore, it is very important to determine the appropriate beam arrangement for the successful implementation of the SBRT. However, a process of treatment planning for SBRT is labo-

adfa, p. 1, 2011.

rious and dependent on an experience of a treatment planner. The treatment planner makes tradeoff decision between the benefit to a tumor and the risk to the surrounding normal tissues. This is traditionally handled by comparison of several treatment plans developed in a time consuming iterative manner. We address this problem by suggestion of treatment plans, which are automatically determined based on similar cases to each patient in a database including plans designed by senior experienced treatment planners.

The usefulness of similar cases in the field of radiation oncology has been shown in some papers. Commowick et al. used a most similar image in a database for the segmentation of critical structures [4]. Chanyavanich et al. developed new prostate intensity modulated radiation therapy plans based on a most similar case [5]. However, we assumed a most similar case could not necessarily be a most usable case for the treatment planning. The goal of this study is to develop a computer-assisted treatment planning system for SBRT based on several similar cases in a radiation treatment planning (RTP) database. In this paper, we aim to evaluate beam arrangements, which are determined based on 1st to 5th most similar cases to each patient in the RTP database.

2 Methods

2.1 Clinical cases

We built a RTP database including 81 cases (47 males and 34 females) and a test dataset of 10 cases (9 males and a female) with lung cancer who received SBRT. These patients were scanned by using a 4-slice computed tomography (CT) scanner (Mx 8000; Philips, Amsterdam, The Netherlands) with a slice thickness of 2.0 - 5.0 mm, and a pixel size of 0.78 - 0.98 mm. Treatment planning was performed by experienced radiation oncologists on a commercially available RTP system (Eclipse version 6.5 and 8.1; Varian Medical Systems Inc., Palo Alto, USA). Seven to eight beams with coplanar and non-coplanar directions were arranged depending on each patient. All patients received a prescribed dose of 48 Gy at the isocenter in 4 fractions.

2.2 Selection of similar cases

Similar cases to an objective case should be defined from the treatment planning point of view. In the proposed method, the five most similar cases to the objective case were automatically selected in the RTP database by defining the weighted Euclidean distance of image feature vectors between the objective case and each case in the RTP database. The weighted Euclidean distance d_{image}, which is considered a similarity measure, was calculated by:

$$d_{image} = \sqrt{\sum_{i=1}^{G} w_i \left(\alpha_i - \beta_i\right)^2} \quad , \tag{1}$$

where G is the number of image features, w_i is the weight of the i-th image feature, α_i is the i-th image feature for the objective case, and β_i is the i-th image feature for each case in the RTP database. In this study, we defined four types of image features, i.e., planning target volume (PTV) location, PTV shape, lung size, and spinal cord positional features. The weights of image features were considered as the importance of image features in terms of the treatment planning. We gave a large weight to the spinal cord positional features for reducing extra dose to the spinal cord. The weights for the PTV location, PTV shape, lung size, and spinal cord positional features were set as 0.3, 0.1, 0.3, and 1.0, respectively.

2.3 Determination of beam arrangements using an affine transformation

The beam angles of the objective case were determined by registration of similar cases to the objective case with respect to lung regions using the following linear registration technique, i.e., affine transformation [6]:

$$\begin{pmatrix} p' \\ q' \\ r' \\ 1 \end{pmatrix} = \begin{pmatrix} u_{11} & u_{12} & u_{13} & u_{14} \\ u_{21} & u_{22} & u_{23} & u_{24} \\ u_{31} & u_{32} & u_{33} & u_{34} \\ 0 & 0 & 0 & 1 \end{pmatrix} \begin{pmatrix} p \\ q \\ r \\ 1 \end{pmatrix}, \tag{2}$$

where the transformation parameters $u_{11} \ldots u_{34}$ were determined based on feature points. First, the affine transformation matrix to register the lung regions of each similar case with that of the objective case was calculated based on two feature points, which were automatically selected for the registration in vertices of the circumscribed parallelepiped of lung regions. Second, a beam direction based on a gantry angle θ and couch angle φ was converted from a spherical polar coordinate system to a Cartesian coordinate system as unit direction vector (p, q, r) as follows:

$$\begin{pmatrix} p \\ q \\ r \end{pmatrix} = \begin{pmatrix} \sin\theta\cos\varphi \\ -\cos\theta \\ \sin\theta\sin\varphi \end{pmatrix}. \tag{3}$$

Third, each beam direction vector of the similar case in the Cartesian coordinate system was modified by using the same affine transformation matrix of equation (2) as a registration with respect to lung regions. Finally, the resulting direction vector (p', q', r') in the Cartesian coordinate system was transformed into the spherical polar coordinate system as gantry angle θ' and couch angle φ' as follows:

$$\theta' = \tan^{-1}\left(\frac{\sqrt{p'^2 + r'^2}}{-q'}\right), \tag{4}$$

$$\varphi' = \tan^{-1}\left(\frac{r'}{p'}\right). \tag{5}$$

In this step, five beam arrangements were determined based on the five most similar cases.

3 Evaluation Methodology

The proposed method was evaluated by comparing eight planning evaluation indices between an objective original plan based on the manual beam arrangement and the five plans based on the five most similar cases to the objective case. Moreover, the five plans obtained from the proposed method were sorted based on an RTP evaluation measure with eight planning evaluation indices, which was the Euclidean distance in a feature space between each plan and an ideal plan. In this study, the ideal plan was assumed to produce a uniform irradiation with a prescription dose in the PTV and no irradiation to the surrounding organs and tissues. The usefulness of each plan was estimated by the following Euclidean distance d_{plan} of the planning evaluation vector between the ideal plan and each plan determined by a similar plan:

$$d_{plan} = \sqrt{\sum_{j=1}^{N}\left(a_j - b_j\right)^2}, \tag{6}$$

where N is the number of planning evaluation indices, a_j is the j-th planning evaluation index for the ideal plan, and b_j is the j-th planning evaluation index for the plan based on the five most similar plans obtained by the proposed method. Note that each planning evaluation index was divided by standard deviation of all cases in RTP database for normalizing the range of each index. The eight evaluation indices were the D95, homogeneity index (HI), conformity index (CI) for the PTV, V5, V10, V20, mean dose for the lung, and maximum dose for the spinal cord, whose values for the ideal plan were set to 48 Gy (prescription dose), 1.0, 1.0, 0%, 0%, 0%, 0 Gy, and 0 Gy, respectively.

The planning evaluation indices for the PTV calculated in this study were the D95, HI, and CI. The D95 was defined as a minimum dose in the PTV that encompasses at least 95% of the PTV. The HI was calculated as the ratio of the maximum dose to the minimum dose in the PTV [7]. The CI represented a degree of conformity, defined as the ratio of the treated volume to the PTV. The treated volume is defined as the tissue volume that is intended to receive at least the selected dose and that is specified by the radiation oncologist as being appropriate to achieve the purpose of the treatment [8].

In this study, the treated volume was defined as the volume receiving the minimum target dose.

The planning evaluation indices for normal tissues, i.e., the lung and spinal cord, were calculated as described below. For the lung volume, which was defined as total lung volume minus PTV, a V5, V10, V20, and mean dose were calculated. The Vx was defined as a percentage of the total lung minus PTV receiving $\geq x$ Gy. The maximum dose of the spinal cord was also calculated.

4 Results and Discussion

Figure 1 shows dose distributions obtained from (a) an original beam arrangement of an objective case, (b) beam arrangement based on the most similar case, and (c) the most usable beam arrangement based on the 4th most similar case. The value of HI, CI, and spinal cord maximum dose were 1.10, 1.65, and 5.37 Gy, respectively, for the original beam arrangement (Figure 1a). On the other hand, they were 1.13, 1.84, and 6.16 Gy, respectively, for the beam arrangement based on the most similar case (Figure 1b). And also, they were 1.08, 1.58, and 4.90 Gy, respectively, for the most usable beam arrangement (Figure 1c). Therefore, the most usable plan has better conformity to the tumor and better sparing of the spinal cord compared with the beam arrangements based on original and also the most similar case.

Table 1 shows the planning evaluation indices obtained from the dose distributions produced by original beam arrangements, beam arrangements based on the most similar case, and beam arrangements of the most usable plan determined by the RTP evaluation measure. In terms of the homogeneity index and conformity index, there were statistically significant differences between the original beam arrangements and beam arrangements based on the most similar case ($P < 0.05$). On the other hand, there were no statistically significant differences between the original beam arrangements and the most usable beam arrangements ($P > 0.05$) in all planning evaluation indices. Therefore, the most usable beam arrangement could be feasible compared with the beam arrangement based on the most similar case.

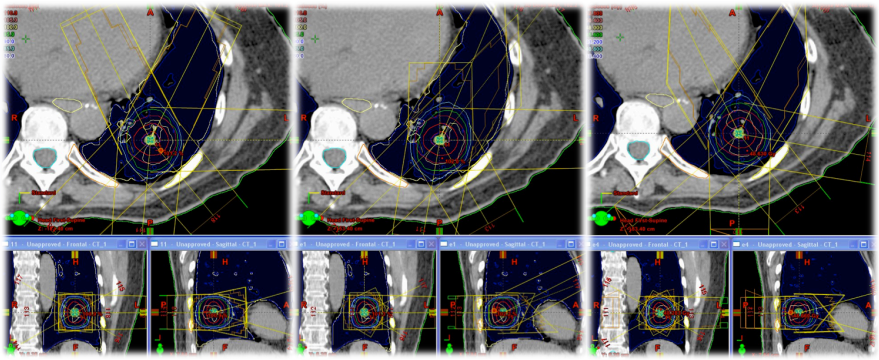

(a) (b) (c)

Fig. 1. Dose distributions obtained from (a) an original beam arrangement, (b) beam arrangement based on the most similar case, and (c) the most usable beam arrangement.

Table 1. Average planning evaluation indices in ten test cases obtained from the dose distributions produced by original beam arrangements, beam arrangements based on the most similar case, and beam arrangements of the most usable plan determined by the RTP evaluation measure.

	Original beam arrangement	Beam arrangement based on the most similar case	Beam arrangement of the most usable plan
PTV			
D95 (Gy)	45.5 ± 0.47	45.4 ± 0.61	45.8 ± 0.62
Homogeneity index	1.13 ± 0.03	1.15 ± 0.04	1.13 ± 0.04
Conformity index	1.70 ± 0.15	1.80 ± 0.18	1.74 ± 0.18
Lung			
V5 (%)	16.0 ± 6.30	15.7 ± 5.04	14.4 ± 4.98
V10 (%)	9.96 ± 4.52	9.54 ± 3.35	9.10 ± 3.08
V20 (%)	3.98 ± 1.46	4.16 ± 1.40	4.06 ± 1.29
Mean dose (Gy)	3.03 ± 1.11	3.04 ± 0.94	2.90 ± 0.93
Spinal cord			
Maximum dose (Gy)	6.13 ± 3.62	5.19 ± 4.94	8.21 ± 7.23

5 Conclusions

We have developed a computer-assisted determination of the usable beam arrangement from similar treatment plans in SBRT. Furthermore, we have studied the feasibility of beam arrangements, which are determined based on 1st to 5th most similar cases to each patient in the RTP database. As a result, the proposed method may

provide usable beam arrangements, which have no statistically significant differences with the original beam directions ($P > 0.05$). Therefore, the proposed method can assist radiation treatment planners in determination of beam arrangements in SBRT.

Acknowledgements

This research was supported by Grant-in-Aid for Japan Society for the Promotion of Science (JSPS) Fellows. The authors would like to express our gratitude to all members in Arimura laboratory (http://web.shs.kyushu-u.ac.jp/~arimura/) for insightful comments and suggestions.

References

1. Nagata Y, Wulf J, Lax I, Timmerman R, Zimmermann F, Stojkovski I, Jeremic B.: Stereotactic radiotherapy of primary lung cancer and other targets: results of consultant meeting of the International Atomic Energy Agency. Int. J. Radiat. Oncol. Biol. Phys. 79, 660-669 (2011)
2. Onishi H, Shirato H, Nagata Y, Hiraoka M, Fujino M, Gomi K, Karasawa K, Hayakawa K, Niibe Y, Takai Y, Kimura T, Takeda A, Ouchi A, Hareyama M, Kokubo M, Kozuka T, Arimoto T, Hara R, Itami J, Araki T.: Stereotactic Body Radiotherapy (SBRT) for Operable Stage I Non-Small-Cell Lung Cancer: Can SBRT Be Comparable to Surgery? Int. J. Radiat. Oncol. Biol. Phys, 81, 1352-1358 (2011)
3. Takayama K, Nagata Y, Negoro Y, Mizowaki T, Sakamoto T, Sakamoto M, Aoki T, Yano S, Koga S, Hiraoka M.: Treatment planning of stereotactic radiotherapy for solitary lung tumor. Int. J. Radiat. Oncol. Biol. Phys. 61, 1565-1571 (2005)
4. Commowick O, Malandain G.: Efficient selection of the most similar image in a database for critical structures segmentation. Proc. MICCAI'07, Part II. Volume 4792 of LNCS. 203-210 (2007)
5. Chanyavanich V, Das SK, Lee WR, Lo JY.: Knowledge-based IMRT treatment planning for prostate cancer. Med. Phys. 38, 2515-2522 (2011)
6. Burger W, Burge MJ.: Digital image processing: An algorithmic introduction using java. 1st ed. New York, Springer, (2007)
7. Kadoya N, Obata Y, Kato T, Kagiya M, Nakamura T, Tomoda T, Takada A, Takayama K, Fuwa N.: Dose-volume comparison of proton radiotherapy and stereotactic body radiotherapy for non-small-cell lung cancer. Int. J. Radiat. Oncol. Biol. Phys. 79, 1225-1231 (2011)
8. International Commission on Radiation Units and Measurements (ICRU). Prescribing, recording and reporting photon beam therapy (Supplement to ICRU Report 50). ICRU Report 62. Bethesda, ICRU, (1999)

Plastimatch 1.6 – Current Capabilities and Future Directions

James A. Shackleford[1], Nadya Shusharina[1], Joost Verberg[1], Guy Warmerdam[1], Brian Winey[1], Markus Neuner[2], Philipp Steininger[2], Amelia Arbisser[3], Polina Golland[3], Yifei Lou[4], Chiara Paganelli[5], Marta Peroni[5], Marco Riboldi[5,6], Guido Baroni[5,6], Paolo Zaffino[7], Maria Francesca Spadea[7], Aditya Apte[8], Ziad Saleh[8], Joseph O. Deasy[8], Shinichro Mori[9], Nagarajan Kandasamy[10], Gregory C. Sharp[1]

[1] Massachusetts General Hospital, Radiation Oncology
[2] Paracelsus University, Institute of Research and Development on Advanced Radiation Technologies (radART)
[3] Massachusetts Institute of Technology, Computer Science and Engineering
[4] Georgia Institute of Technology, Electrical and Computer Engineering
[5] Politecnico di Milano, Biomedical Engineering
[6] Centro Nazionale di Adroterapia Oncologica, Bioengineering Unit
[7] Magna Graecia University, Experimental and Clinical Medicine
[8] Memorial Sloan Kettering Cancer Center, Department of Medical Physics
[9] National Institute of Radiological Sciences, Research Center for Charged Particle Therapy
[10] Drexel University, Electrical and Computer Engineering

Abstract. Open-source software provides an economic benefit by reducing duplicated development effort, and advances science knowledge by fostering a culture of reproducible experimentation. This paper describes recent advances in the plastimatch open software suite, which implements a broad set of useful tools for research and practice in radiotherapy and medical imaging. The focus of this paper is to highlight recent advancements, including 2D-3D registration, GPU-accelerated mutual information, analytic regularization of B-spline registration, automatic 3D feature detection and feature matching, and radiotherapy plan evaluation tools.

Keywords: Open source software, medical imaging, software engineering, radiotherapy.

1 Introduction

The fields of medical imaging and radiotherapy use sophisticated software to achieve advanced medical results. Commercial software is generally closed source, which makes it difficult to use for research, and often lacks the flexibility to communicate with complementary software from other vendors. This gap in functionality is properly filled by open-source solutions, which are well suited for

research. This paper describes the plastimatch software suite for radiotherapy image processing [1]. Plastimatch is open-source software, distributed under a BSD-style license. The focus of plastimatch is on high-performance algorithms for medical image computing, and on flexible radiotherapy utilities. Using standard interchange formats such as DICOM and DICOM-RT, plastimatch can be easily used together with other open source tools, including CERR [13], Conquest DICOM [2], ImageJ [3], VV [23], and 3D Slicer [4].

2 Background and History

The origin of the plastimatch project was a collection of image processing software written to support medical physics research. The first utility, DRR generation, was written in 2003. Shortly thereafter, deformable image registration was developed using the Insight Segmentation and Registration Toolkit (ITK) [5], and cone-beam CT reconstruction using the Feldkamp, Davis and Kress (FDK) algorithm [14].

In an attempt to overcome the long computation times of ITK's deformable registration algorithms, we began exploring GPU accelerated algorithms in 2006. The first algorithms targeted were FDK filtered backprojection and demons deformable registration [30]. At the time, CUDA was not yet mature, and therefore these algorithms were deployed using the BrookGPU compiler and runtime library [9]. Working together with our institutional lawyers, we released the first open source version of the GPU Imaging Toolkit (GPUIT) in early 2007. Later in 2007, the GPUIT registration routines were consolidated with the ITK registration routines to create the plastimatch project.

Table 1: Summary of plastimatch algorithms for 3D image registration.

Registration Algorithm	ITK	SC	MC	GPU
Translation	✓			
Rigid	✓			
Affine	✓			
Demons	✓	✓		✓
B-spline (MSE,MI)	✓	✓	✓	✓
Viscous Fluid				✓
Thin-plate spline	✓			
Wendland, Gaussian Spline		✓		

In 2008, a native implementation of B-spline registration was designed to replace the ITK implementation, and the FDK reconstruction code was ported from BrookGPU to CUDA. In 2009, we added GPU accelerated B-spline registration [24], landmark-based interactive registration, and DICOM-RT. This year also saw the first usable user interfaces, as command-line programs launched from 3D Slicer and Aqualizer. In 2010, we considerably improved the landmark-based registration by offering three different algorithms: thin-plate spline, Wendland radial basis spline, and regularized Gaussian spline. The first GPU accelerated

mutual information algorithm was released this year, together with OpenCL acceleration, and dose volume histogram (DVH) computation capabilities. In 2011, we released Reg23, a full-featured 2D-3D registration algorithm, capable of automatic registration using five different cost functions, interactive initialization, and programmable pre-processing and post-processing. Analytic regularization of B-spline registration was also introduced, as was automatic feature detection and matching using the scale-invariant feature transform (SIFT) algorithm.

3 Overview of Plastimatch

Traditionally, plastimatch has been conceived and developed as an end-user application, rather than as a library or toolkit. The standard method of using plastimatch is on the command line, with configuration files and command line options. A typical invocation would be to specify a command, such as register, together with the necessary input files, configuration files, and options. A list of supported commands are shown in the usage screen:

```
$ plastimatch --help
plastimatch version 1.5.11-beta (3583M)
Usage: plastimatch command [options]
Commands:
  add           adjust        average       crop          compare
  compose       convert       diff          dvh           fill
  header        mask          probe         register      resample
  scale         segment       stats         synth         synth-vf
  thumbnail     warp          xf-convert
```

3.1 Automatic 3D-3D Registration

Plastimatch uses a multi-stage, multi-algorithm framework for automatic image registration. Only pairwise registration is supported. In the initialization stage, the images are loaded, together with any image masks or initial transformations. The framework runs a fixed sequence of registration stages, as directed by a parameter file. Each registration stage specifies the image resolution (for multi-resolution registration), the transform and metric to be optimized, and the optimization algorithm and parameters. If desired output files can be specified at each stage for saving intermediate results. A typical sequence of stages might include a single rigid alignment stage, followed by two to four deformable registration stages with increasing resolution and decreasing grid spacings.

Table 1 lists the summary of algorithms included in plastimatch, which includes six different core registration methods. Depending on the registration method, you can choose one of four implementations: ITK, single core (SC), multi-core (MC), or GPU. The six registration algorithms can operate on eight different transform types: six ITK transforms and two native transforms. At the end of each stage, the optimal transform is propagated to the next stage, and automatically converted to a new transform type by the plastimatch application framework.

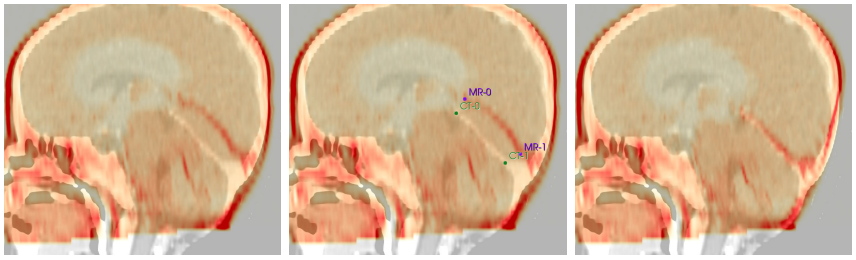

Fig. 1: Interactive registration is used to warp the MRI of a 6-month old infant onto the CT of the same patient at age 2. The initial registration properly matches the skull, but features within the brain are not properly aligned (left). Landmarks are placed (center), which improve the registration (right).

3.2 Cone-beam CT and Digitally Reconstructed Radiographs

A cone-beam CT reconstruction application is provided which implements filtered back projection using the Feldkamp, Davis and Kress (FDK) algorithm. Input images in either raw, pfm, or hnd format are read, filtered, and backprojected into a user defined volume geometry. Images in raw or pfm format must be accompanied by a geometry specification file, whereas files in the Varian hnd format use the geometry specified by the file header. Ramp filtering is performed on the CPU using the FFTW library [16], while backprojection is performed on either CPU or GPU. The plastimatch DRR generator implements three variants of the Siddon ray tracing method [26]. The fastest and most popular method uses the original exact pathlength method based on the intersection of rays with the image voxels. In addition, two voxel interpolation methods are included, which can be used to increase the apparent resolution of the DRR construction. Both multi-core and GPU versions are available.

3.3 Interactive (Landmark-based) Image Registration

While automatic registration yields acceptable results in many cases, we are often confronted with difficult registration problems where automatic registration fails. For this purpose, plastimatch includes two manual registration tools: a global landmark-based tool based on thin plate splines, and a tool based on radial basis functions (RBF) which allows us to make local registrations by adjusting the RBF support .

The global tool is implemented as an ITK wrapper, takes a list of corresponding points in 3D, and generates a complete vector that interpolates all of the input landmarks. This method requires a minimum of six landmarks, which are used to find a global affine transform superimposed with a minimum energy deformation field [8]. The global landmark registration results can be used as a standalone method, or to initialize the automatic registration. In contrast, the RBF tool is a native warper, and does not perform global rigid or affine mapping. Instead, it uses a small number of landmark pairs to correct failed deformable registration results. The algorithm utilizes two types of radial basis functions,

Wendland function with finite support [7, 15] and non-truncated Gausian function [6, 25]. In both cases, a deformation is found by solving a system of linear equations which is computationally very efficient as compared with algorithms based on complex multidimensional minimization. In addition, Gaussian RBF have a distinct feature with respect to regularization, because the regularized vector field can be solved exactly with a simple equation. An independent regularization parameter is defined to control the balance between the fidelity of the alignment of landmark pairs, and the smoothness of the deformation field. An example of this idea is shown in Fig. 1, where the failed registration (left), is corrected using two pairs of landmarks (center, right).

3.4 2D-3D Registration

The Reg23 module of plastimatch along with the oraifutils-sublibrary enables rigid registration of a 3D volumetric image (e.g. a computed tomography) with an essentially arbitrary number of projective 2D images (e.g. X-rays). The transformation parameters (3 rotations, 3 translations) are iteratively optimized with respect to a cost function which assesses the similarity between the X-rays and on-the-fly DRRs computed from the volume. Uniform ray-casting DRR computation is implemented on the GPU using the openGL shading language (GLSL). Beside of selected similarity metrics (normalized mutual information, normalized cross correlation, gradient difference, mean reciprocal square difference) derived from ITK, stochastic rank correlation [27] is a further configurable cost function. All input images can be configured to be pre-processed prior to registration including resampling, rescaling, cropping and unsharp masking. Downhill simplex (AMOEBA) and 1+1 evolutionary algorithms are available for optimization. In order to restrict similarity evaluation to a certain region of interest (ROI) in the X-rays, a so-called auto-masking module is available [22]. Based on RT structure sets which are typically generated in the pre-planning stage, an entity-specific heuristic is configurable which allows logical combination, dilation/erosion and projection of structures onto the X-ray planes which produces binary mask images that constrain metric evaluation. For example, in the case of pelvis registration, this mechanism enables automatic determination of ROIs that exclude the femora which are prone to move relatively over the treatment course [22, 28, 29]. Fig. 2 gives a schematic overview of the main components using the example of dual 2D/3D pelvis registration.

In addition to the core algorithm offering the mentioned capabilities, a Qt-based general user interface (GUI) is provided as shown in Fig. 2. The GUI enables the user to monitor the registration process, and simultaneously to influence registration by mouse interactions (translation, rotation, registration initialization). The overall program is configurable via a simple ASCII-based file in order to enable easy integration with other applications such as recordverify-systems. Moreover, utilizing this mechanism batch processing is achievable where the registration results are stored in output files. Current work aims at providing more convenient means for setting up the imaging geometry, extending the port-

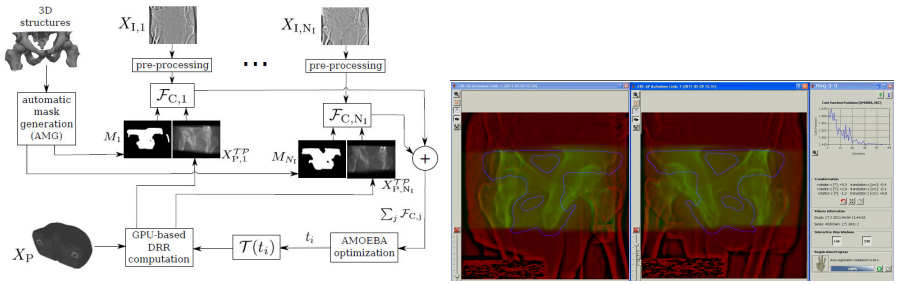

Fig. 2: (left) Schematic overview of Reg23 components and their interconnections. (right) Reg23 GUI showing colored overlays of X-rays and DRRs. The ROI generated by the auto-masking module is shown as a blue contour. Registration parameters are displayed in the control panel on the right.

folio of available DRR algorithms and implementing appearance-model-based 2D/3D registration.

3.5 Automatic Feature Detection and Matching

Several algorithms have been developed to perform automatic landmarks extraction and matching, with the goal of increasing the accuracy of detection and decreasing the cost in terms of time. First operators for the automatic extraction of points have examined an image at a single scale, thus limiting the accuracy and stability of feature detection. Scale Invariant Features Transform (SIFT) is a method that provides extraction and matching of stable and prominent points at different scales between two images. The algorithm supported by Plastimatch was derived from Cheung and Hamarneh [11] and implemented in C++ using the Insight Toolkit (ITK) [5]. This method takes in inputs two 3D (isotropic or anisotropic) images and generates lists containing stable landmarks for each image as well as feature matches between the two images. The output files (.fcsv) contain landmarks in physical coordinates that can be used with 3D Slicer Fiducial module [4]. Figure 1 shows examples of successful individuation of corresponding features in the original (left) and synthetic (right) image of a phantom (RANDO phantom, The Phantom Laboratories, Salem, NY). The synthetic image is obtained by applying rigid and non-rigid transformations to the phantom.

3.6 Data Interchange

Plastimatch supports a wide variety of file input types for data interchange. Using ITK wrappers, most image formats are supported, including DICOM, Analyze, Metaimage, and NRRD. In addition, partial support exists for DICOM-RT, XiO, and RTOG formats. Plastimatch is capable of rasterizing DICOM-RT structure sets into images, as well as converting images back into DICOM-RT structure sets. In addition, a utility is provided for attaching existing DICOM-RT structure sets onto arbitrary DICOM series.

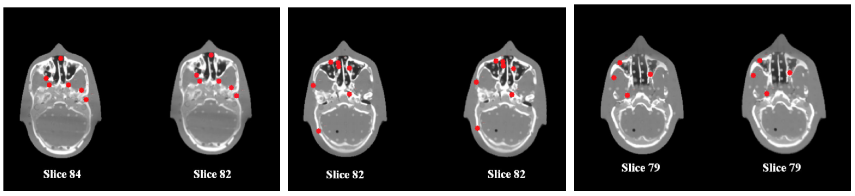

(a) Translation 6mm (b) Rotation 5 degrees (c) Non-rigid transform

Fig. 3: Successful examples of successful corresponding features detection (red codes) in the original (right) and synthetic (left) image of RANDO phantom. Rigid Transforms: (a) Translation [6 mm] in right-left, anterior-posterior, superior-inferior directions and (b) Rotation [5] in superior-inferior direction. Non-rigid transform: (c) maximum deformation of 15.42, 5.72, 4.16 mm in right-left, anterior-posterior, superior-inferior directions, respectively.

3.7 User Interface

While a native user interface is supported by Reg23, the plastimatch module offers a user interface only as a plugin for Aqualizer [21] and 3D Slicer [4]. Aqualizer is a specialized research software for four-dimensional treatment planning. Deformable image registration is used to map radiation dose from all breathing phases onto a reference phase, and accumulate the time-averaged dose. 3D Slicer is a general purpose research software for medical image computing. Plastimatch plugins are available for automatic registration, landmark-based registration, and DICOM-RT import.

4 Future Directions

4.1 Embedded Scripting

Plastimatch 1.6 features a new Lua-based embedded scripting engine that allows users to construct custom workflows quickly and easily with minimal programming experience. Images, transforms, and core plastimatch algorithms are exposed through the scripting interface as simple abstract objects, which the user can use to design an image processing pipeline specific to their particular application. Fig. 4 demonstrates the usage of image, registration, and transform objects to construct a 4D registration workflow in just 17 lines, excluding comments. For users who need more flexibility and dynamic control, the scripting engine can be ran in interactive mode. In this mode, the user is provided with a command driven interface similar to MATLAB where they may navigate the filesystem, use all available objects to operate on their data, run pre-written scripts, and preview resulting images using an integrated slice viewer before writing them to disk.

4.2 Viscous Fluid Registration

The viscous fluid model [12] for registration assumes that the deformation is governed by the Navier-Stokes equation of viscous fluid motion. This approach takes

```
-- load breathing phase 3 as the reference image for each pair-wise registration
reference_phase = Image.load ("data/phase_03.mha")
registration = Register.load ("data/stages.txt")
registration.fixed = reference_phase
-- define remaining phases in a phase array
phases = {
  { image = "data/phase_01.mha", warp = "output/warp_01.mha", xf = "output/xform_01.mha" },
  { image = "data/phase_02.mha", warp = "output/warp_02.mha", xf = "output/xform_02.mha" },
  { image = "data/phase_04.mha", warp = "output/warp_04.mha", xf = "output/xform_04.mha" },
  { image = "data/phase_05.mha", warp = "output/warp_05.mha", xf = "output/xform_05.mha" }
}

-- loop through every input/output pair "p" in our phases array
for _,p in pairs(phases) do
  -- load the phase and use as moving image for pair-wise registration
  destination_phase = Image.load (p.image);
  registration.moving = destination_phase
  -- perform the registration and save the transform
  xf = r:go()
  -- warp the destination phase and save outputs
  warp = destination_phase + xf
  warp:save (p.warp);
  xf:save (p.xf);
end
```

Fig. 4: The new scripting system uses a familiar object-oriented approach to provide users with direct access to core Plastimatch algorithms. This allows for rapid design of custom workflows, such as the 4D registration workflow shown here.

into account the physical model of tissue motion to regularize the deformation fields, thus able to handle larger deformation compared with optical flow [17] and elastic models [10]. A similarity measure is first established to quantify how close two image volumes are to each other according to some chosen metric. For multimodal registration, mutual information (MI) is a popular choice. Recently a new measure is proposed by Lou et al. [18], called Bhattacharyya distance (BD). It can avoid the instability issues that are present in MI. Next the deformation that maximizes this similarity is computed by solving a N-S equation, in which the force field that drives the deformation in an appropriate direction is parallel to the gradient of the chosen similarity measure. The optimal solution is iteratively updated by convolving the force field with a Gaussian filter as an approximation. Moreover a multi-resolution scheme is used to increase the speed and robustness. We implement the viscous fluid model with either MI or BD as the similarity measure on the GPU [19]. It takes 6 seconds to register two images of size 256x256x60 for 50 iterations using three multi-resolution levels.

4.3 Deformable Image Registration in CERR

While it is possible to use plastimatch with CERR via DICOM-RT file exchange, this method is somewhat time consuming and complicated for end-users. During 2012, we intend to supply an interface for using plastimatch directly from within CERR. The first stage of development will define a file-based method for exchanging images, doses, and structure sets; thereby enabling dose warping, dose accumulation, structure set warping, and automatic contouring. This interface will provide storage of the B-spline coefficients or dense vector fields

for further external processing. Second stage development will investigate batch processing methods and memory-based data exchange.

4.4 Multi Atlas-based Segmentation

Plastimatch will soon be adding support for multi-atlas-based segmentation, which aims to automatically delineate structure boundaries for an unlabeled target CT scan. Provided an atlas consisting of CT scans from other patients with the relevant structure labeled, each CT scan in the atlas is registered to the unlabeled target scan and the resulting transform is applied to each of the labeled atlas structures. This results in the labels from each of the atlas scans being mapped into the space of the target as shown in Fig. 5. To distill these multiple delineations into a single label for the target, a vote is conducted for each target scan voxel to determine if it is within the structure. With this label fusion, multi-atlas-based segmentation can delineate each relevant structure in the target CT.

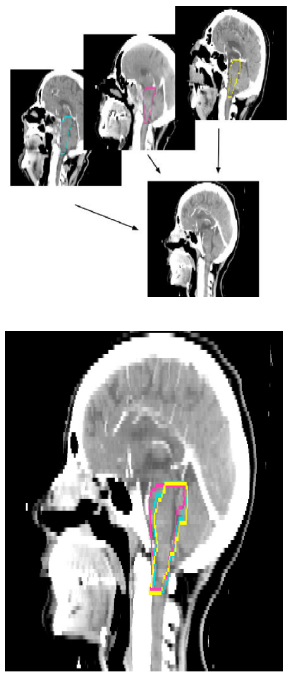

Fig. 5: Multi-atlas based segmentation uses voting to combine multiple registration results into a best contour for a structure.

5 Software Engineering

As of June 2012, plastimatch comprises 163,000 lines of cross-platform code, and makes heavy use of the external libraries: ITK, VTK, Qt, DCMTK, FFTW, CUDA, and SQLite. Platform specific build configurations are managed using CMake [20], which accepts a build description language and generates a sane build environment specific to the available external libraries and compiler features. The absence of a library results in reduced functionality; for example, if CUDA is not installed plastimatch will still build but CUDA-accelerated implementations will be unavailable. The plastimatch philosophy is that external libraries are optional.

Software version control and defect tracking are managed through a custom web-enabled install of GForge Advanced Server. Source code and documentation are disseminated though a subversion repository, which allows anonymous access. As a measure to maintain and improve software quality, the CTest system is used to perform automated software testing. Test cases are included with the software distribution and can be executed using the CMake generated build environment. Prior to committing changes, developers execute a battery of tests to ensure that functionality has not regressed. Additionally, automatic regression testing is performed nightly across various build configurations.

6 Licensing

The plastimatch software is licensed under a BSD license for Reg23, and a custom BSD-style license for plastimatch. These licenses specifically allows royalty-free non-exclusive license to use, modify, and redistribute our software. The primary restrictions on licensing are that (1) attribution and copyright notices be retained, (2) modified versions must be clearly marked, and (3) names, logos, and trademarks of our institutions are not used for promotion. Our software is provided AS IS, without warranty. The custom license clearly states that the software has been designed for research purposes only, and that clinical applications are neither recommended nor advised. A complete copy of the license is available on-line [1].

Acknowledgments

This work was supported in part by NSF ERC Innovation Award EEC-0946463, NIH/ NCI 6-PO1 CA 21239, the Federal share of program income earned by MGH on C06CA059267, an Ira J Spiro translational research grant, the Progetto Rocca Foundation, a collaboration between MIT and Politecnico di Milano. This project was supported by grants from the National Center for Research Resources (P41-RR-013218) and the National Institute of Biomedical Imaging and Bioengineering (P41-EB-015902) of the National Institutes of Health.M Peroni, C Paganelli, and M Riboldi would like to acknowledge AIRC, Italian Association for Cancer Research Foundation, for the support. This work is part of the National Alliance for Medical Image Computing (NAMIC), funded by the National Institutes of Health through the NIH Roadmap for Medical Research, Grant 2-U54-EB005149. Information on the National Centers for Biomedical Computing can be obtained from http://nihroadmap.nih.gov/bioinformatics.

References

1. Plastimatch. http://plastimatch.org
2. Conquest DICOM. http://www.xs4all.nl/~ingenium/dicom.html
3. ImageJ. http://rsb.info.nih.gov/ij
4. 3D Slicer. http://slicer.org
5. The Insight Segmentation and Registration Toolkit. http://itk.org
6. Arad, N., Dyn, N., Reisfeld, D., Yeshurun, Y.: Image warping by radial basis functions: Application to facial expressions. CVGIP: Graphical Model and Image Processing 56(2), 161–172 (1994)
7. Arad, N., Reisfeld, D.: Image warping using few anchor points and radial functions. In: Computer Graphics Forum. vol. 14, pp. 35–46. Wiley Online Library (1995)
8. Bookstein, F.: Principal warps: Thin-plate splines and the decomposition of deformations. Pattern Analysis and Machine Intelligence, IEEE Transactions on 11(6), 567–585 (1989)
9. Buck, I., Foley, T., Horn, D., Sugerman, J., Fatahalian, K., Houston, M., Hanrahan, P.: Brook for GPUs: stream computing on graphics hardware. In: ACM Transactions on Graphics (TOG). vol. 23, pp. 777–786. ACM (2004)

10. Chefd'Hotel, C., Hermosillo, G., Faugeras, O.: A variational approach to multi-modal image matching. In: Variational and Level Set Methods in Computer Vision, 2001. Proceedings. IEEE Workshop on. pp. 21–28. IEEE (2001)
11. Cheung, W., Hamarneh, G.: n-SIFT: n-Dimensional Scale Invariant Feature Transform. Image Processing, IEEE Transactions on 18(9), 2012–2021 (2009)
12. D'Agostino, E., Maes, F., Vandermeulen, D., Suetens, P.: A viscous fluid model for multimodal non-rigid image registration using mutual information. Medical image analysis 7(4), 565–575 (2003)
13. Deasy, J., Blanco, A., Clark, V.: CERR: a computational environment for radiotherapy research. Medical physics 30, 979 (2003), http://radium.wustl.edu/CERR
14. Feldkamp, L.A., Davis, L.C., Kress, J.W.: Practical cone-beam algorithm. J. Opt. Soc. Am. A 1(6), 612–619 (Jun 1984)
15. Fornefett, M., Rohr, K., Stiehl, H.: Radial basis functions with compact support for elastic registration of medical images. Image and Vision Computing 19(1), 87–96 (2001)
16. Frigo, M., Johnson, S.: The design and implementation of FFTW3. Proceedings of the IEEE 93(2), 216–231 (2005)
17. Horn, B., Schunck, B.: Determining optical flow. Artificial intelligence 17(1-3), 185–203 (1981)
18. Lou, Y., Irimia, A., Vela, P., Chambers, M.C., van Horn, J., Vespac, P.M., Tannenbaumd, A.: Multimodal Deformable Registration of Traumatic Brain Injury MR Volumes via the Bhattacharyya Distance. Medical Image Analysis (2012 Submitted)
19. Lou, Y., Jia, X., Gu, X., Tannenbaum, A.: A GPU-based Implementation of Multimodal Deformable Image Registration Based on Mutual Information or Bhattacharyya Distance. http://hdl.handle.net/10380/3268 (May 2011)
20. Martin, K., Hoffman, B.: Mastering CMake. Kitware, Inc (2010), http://cmake.org
21. Mori, S., Chen, G.: Quantification and visualization of charged particle range variations. International Journal of Radiation Oncology* Biology* Physics 72(1), 268–277 (2008)
22. Neuner, M., Steininger, P., Mittendorfer, C., Sedlmayer, F., Deutschmann, H.: Automatic mask generation for 2D/3D image registration with clinical images of the pelvis. International Journal of Computer Assisted Radiology and Surgery 6 (Supplement 1), S54–S55 (6 2011)
23. Seroul, P., Sarrut, D.: VV: a viewer for the evaluation of 4D image registration. MIDAS Journal (Medical Image Computing and Computer-Assisted Intervention MICCAI'2008, Workshop - Systems and Architectures for Computer Assisted Interventions), 1–8 (2008), http://vv.creatis.insa-lyon.fr/
24. Shackleford, J., Kandasamy, N., Sharp, G.: On developing B-spline registration algorithms for multi-core processors. Physics in Medicine and Biology 55, 6329 (2010)
25. Shusharina, N., Sharp, G.: Analytic regularization for landmark-based image registration. Physics in Medicine and Biology 57(6), 1477 (2012), http://stacks.iop.org/0031-9155/57/i=6/a=1477
26. Siddon, R.: Fast calculation of the exact radiological path for a three-dimensional CT array. Medical Physics 12, 252 (1985)
27. Steininger, P., Neuner, M., Birkfellner, W., Gendrin, C., Mooslechner, M., Bloch, C., Pawiro, S., Sedlmayer, F., Deutschmann, H.: An ITK-based Implementation of the Stochastic Rank Correlation (SRC) Metric. Insight Journal (11 2010)

28. Steininger, P., Neuner, M., Mittendorfer, C., Scherer, P., Sedlmayer, F., Deutschmann, H.: Clinical implementation of gpu-accelerated n-way 2d/3d image registration for inter-fractional patient positioning in radiotherapy. International Journal of Computer Assisted Radiology and Surgery 6 (Supplement 1), S56–S57 (6 2011)
29. Steininger, P., Neuner, M., Weichenberger, H., Sharp, G., Winey, B., Kametriser, G., Sedlmayer, F., Deutschmann, H.: Auto-masked 2d/3d image registration and its validation with clinical cone-beam computed tomography. Physics in Medicine and Biology 57(13), 4277 (2012)
30. Thirion, J.: Image matching as a diffusion process: an analogy with Maxwell's demons. Medical image analysis 2(3), 243–260 (1998)

Application of the SlicerRT toolkit for image-guided radiation therapy research

Csaba Pinter[1], Andras Lasso[1], An Wang[2], David Jaffray[2,3,4,5], and Gabor Fichtinger[1]

[1]Laboratory for Percutaneous Surgery, School of Computing, Queen's University, Kingston, ON, Canada

[2]Radiation Medicine Program, Princess Margaret Hospital, University Health Network, Toronto, ON, Canada

[3]Techna Institute for the Advancement of Technology for Health, University Health Network, Toronto, ON, Canada

[4]Radiation Oncology, Medical Biophysics & IBBME, University of Toronto

[5]Ontario Cancer Institute

Abstract. *Purpose:* Interest in adaptive radiation therapy research is constantly growing. The available software tools are usually tied to expensive proprietary applications. Although there are free open-source software applications and algorithms to solve particular problems of radiation therapy (RT) research, each of these standalone tools is limited to a specific purpose, development environment, and input/output data formats. To address these limitations, we propose SlicerRT, a customizable, free, open-source RT research toolkit.

Methods: SlicerRT is an open-source extension for the widely used 3D Slicer platform. SlicerRT provides functionality specifically designed for RT research, in addition to the powerful tools that 3D Slicer offers for visualization, registration, segmentation, and data management. The feature set of SlicerRT was defined through consensus discussions among a large pool of RT researchers, including both radiation oncologists and medical physicists. The development processes used were similar to those of 3D Slicer, which ensure traceability and professional quality of the resulting software and its distribution and user support mechanisms.

Results: Modules have been created for importing and loading DICOM-RT data, computing and displaying dose volume histograms for anatomical structures, creating accumulated dose volumes and isodose surfaces, and comparing dose volumes. Testing environment was set up to automatically test the modules for regression and against results of other applications.

Conclusions: An open-source software platform has been created and tested to support RT research. SlicerRT aspires to be an open-source toolkit for RT research, providing fast computations and convenient workflows for researchers. It is a medium into which RT researchers can integrate their methods and algorithms, and conduct comparative testing. SlicerRT also provides a general image-guided therapy infrastructure to assist clinical translation of experimental therapeutic approaches.

Keywords: Radiation therapy, treatment planning, 3D Slicer, DICOM-RT

User interface prototyping to understand radiology thinking

Edit Varga, Adinda Freudenthal

Delft University of Technology, Netherlands
{e.varga, a.freudenthal}@tudelft.nl

Abstract Recent technological solutions for image-guided therapies focus on replacing the cognitive processes of physicians. However, there is a lack of knowledge in the field of cognitive ergonomics regarding radiology image thinking, such as image interpretation and 3D navigation. This paper addresses the need of studying mental models in this context. The goal is to be able to design better user interfaces for advanced technological solutions which match the cognitive processes of physicians. The usefulness of employing a prototype in the early phases of development is shown through the example of oblique view interpretation. Recommendations are given how user interface prototyping can be used to study mental models.

1 Introduction

Radiotherapy and interventional radiology procedures require the physician, the physicist, or technician to read a set of 2D radiology images (e.g. Computed Tomography (CT) or Magnetic Resonance Imaging (MRI)) in order to plan, perform and evaluate a treatment. These 2D images represent the 3D anatomy of the patient, which has to be mentally reconstructed and manipulated in order to make decisions for certain steps of a treatment, such as planning the trajectory of an ablation needle or a radiation beam. 3D reconstructions may provide a general 3D understanding of the scanned body part, but these images do not provide detailed anatomical information for the planned treatment. Furthermore, interaction with 3D images is restricted to basic operations, such as rotation and zooming.

Many research and technological solutions focus on replacing the cognitive processes of the physician with computationally supported visualizations, simulations and decision making, for example, segmented tumors or vessels are shown to support spatial orientation and navigation, or images are registered to exploit the combined information coming from multiple sources (e.g. when one modality clearly visualizes the tumor and the other can be used for real-time navigation) [1].

The current research was conducted as a preparation for a larger project to develop a new interface for 3D ultrasound image guidance. Integration of registered CT or MRI was considered as possible future technology. To achieve smooth integration of new technologies in the interventional scene, technological developments are sup-

ported by designing novel user interface solutions, studying cognitive ergonomics, as well as workflow redesign.

However, there is actually little knowledge about cognitive ergonomics in this field, such as how physicians can interpret and interact with segmentation overlays on radiology images or how they can interpret and navigate based on new forms of images. The main undiscovered areas for example are mental models of anatomy, mental manipulations of anatomy, spatial orientation, and navigation using radiology images. In order to be able to develop efficient 3D navigation support, a better understanding of cognitive ergonomics related issues is necessary.

The investigation addresses the need for understanding mental models of physicians in order to develop user interfaces which fit their thinking processes. While it is a general problem regarding radiology image thinking, in this paper this need is presented through the example of interventional radiology. The form of mental models and their manipulations are hard to reveal, because they are not directly available to the outsider [2] and it is difficult for people to externalize and verbalize mental models and processes. This paper reports on experiences in using an interactive prototype to study cognitive processes of physicians in the early phases of development and for iterative improvement, as opposed to only using the prototype to test usability. The difference between these two approaches will be explained in subsequent sections. Finally, recommendations will be made on the properties of the prototype which are crucial in order to obtain the expected results.

2 Mental models and manipulations

In general, mental models are internal representations of external reality, such as objects, situations or working principles of a system [3]. In medical image usage it includes aspects such as anatomy, physiological processes (e.g., temperature changes because of blood flow), etc. In the current phase of our research, we restrict the usage of the term to represent spatial mental models of human anatomy as perceived, interpreted and mentally constructed based on 2D radiology images. As the physician scrolls through a series of radiology images and observes the anatomy from different viewpoints, (s)he constructs a 3D mental model in his mind.

Radiology images are usually taken from predefined viewpoints which are orthogonal to the human body. Anatomy drawings for training, as well as CT/MRI scans show orthogonal cross-sections of the human body. These are the reference images the physician can fully interpret, that is, (s)he is able to maintain spatial orientation, locate structures and identify structures based on their contours. They are also the images based on which a physician can construct a mental model of anatomy. Images taken in oblique orientations are generally difficult to interpret and are not trusted**.** Manipulation of the mental model is necessary during medical image usage [4].

In order to achieve successful 3D navigation, the physician needs to maintain spatial orientation, that is, to be able to correctly identify anatomical locations in the human body and to understand the spatial relationships of surrounding organs or tissues [5]. The navigational goal of the physician is to guide the needle or a beam through a trajectory that is safe for the patient by avoiding vital structures, and to end in the target position, e.g. in a tumor.

3 Methods and materials

3.1 Approach

Cognitive processes of physicians were studied. This means attaining insight into the (tacit) knowledge of physicians which is built up from natural human capacities, combined with trained skills and experience in practice. Furthermore, specific understanding of cognitive strategies of manipulating 3D models of the patient's anatomy in the mind. The aim was to come up with theoretical models of 3D navigation and mental manipulations and to use in the design of matching user interface solutions.

3.2 Methods

The following methods were used for studying mental models: ethnography, explorative studies with the prototype, comparing results to vision science (in-depth literature study) and proposing a theory, and validation of theory by interviewing doctors. These methods are presented through an example in Section 4.2.

3.3 Materials

The current version of the prototype includes a number of hardware and software elements. The elements were chosen to accommodate the cognitive ergonomics investigation, and also to support following development phases, such as usability testing.

- Visual Studio 2005 was used as programming environment and the code was written in C++.
- To visualize objects from different viewpoints Coin3D was used for 3D graphics (www.coin3d.org).This was needed to attain sufficient fidelity regarding response to motor control of tools, essential for understanding mental model coupling to hand motions.
- For rapid user interface development and to design flexible user interfaces Qt (http://qt.nokia.com/products) was used. This is a crucial property: user feedback should lead to quick and substantial changes in user interface, i.e., doable in one evening for next round testing with significantly changed interface.
- Coin3D and Qt was integrated using the SoQt libraries.
- For handling volumetric data SIMVoleon was applied. 3D data are needed in radiology prototyping as mental models and navigation are 3D in nature.

- For easy integration of the user interface Virtual Reality Peripheral Network (VRPN) (http://www.cs.unc.edu/Research/vrpn/) was used.
- Motion tracking was used to provide real-time visual feedback about the tracked instrument: Ascension's Flock of Birds device (http://www.ascension-tech.com/).
- To create a volume out of a series of axial CT slices that is usable by SIMVoleon a Matlab (http://www.mathworks.com/) script was employed.

4 Results

4.1 Prototype roles

According to our experiences, using an interactive prototype is useful for:

- *Explorative studies*: Novel interactions, as they may be imagined in the final design, can be explored. Putting the user in a real clinical situation, and by providing multiple solutions at the same time, the future user can explore which solutions are the most efficient.
- *Workflow studies*: When interacting with the prototype and explaining what users are doing and thinking, it is easier for the engineer to understand the clinical workflow. Users tend to recall previous cases which can further deepen this knowledge. Difficult situations and similarities to other procedures are also explained.
- *Mental model studies*: Observations combined with thinking aloud and interviews are general methods for mental model understanding. However, observations in themselves are useless for the observer without (deep) clinical knowledge to make assumptions about physical and cognitive actions of the physician, due to the minimally invasive nature of the procedures in which difficult imaging modalities and subtle hand movements are applied. Concentrating on the treatment, physicians are only able to provide a very limited amount of information during the procedure. Deep interviews may bring up knowledge about the treatment, but this knowledge is mainly procedural. The physician recalls the procedure and explains the experienced difficulties, but being disconnected from the real situation, this method is inefficient to study psychomotor actions. Having an interactive prototype which simulates the real situation provides a relaxed way for the physicians (without harming the patient) to express themselves and for the researcher to ask specific questions. Reactions often bring up issues about learning and experience.
- *Communication*: Inefficient communication and misunderstandings are highly limiting factors in multidisciplinary projects. Discussions over an interactive prototype are useful to communicate ideas to the future end user and to correct for wrong assumptions in early phases of design. Besides, communication of other team members, such as industrial designers, computer scientists and imaging specialists becomes easier as well.
- *Experiencing interaction*: By actually experiencing the interaction (e.g. planning a needle trajectory or adjusting the needle to the planned trajectory with real-time visual feedback), the user does not need to imagine how an interaction concept

would work in reality. Furthermore, also the non-medical researcher can experience the interaction, and can have a feel of the physician's work.
- *Co-design and idea generation*: Try-outs of the prototype naturally bring up improvement possibilities as well as new ideas.

4.2 Example: oblique slice interpretation

A prototype was designed to test some new user interaction concepts using CT datasets for two interventional radiology tasks: (1) evaluating needle trajectories and (2) following a planned trajectory. The following interactions were available:
- Traditional orthogonal views (axial, sagittal, coronal)
- Views related to the needle: slices that are orthogonal to the needle (needle-dot view: looking from the point of view of the needle), and slices which contain the entire needle line (needle-line view: rotation around the needle)
- A preoperatively planned needle trajectory in all views
- Real-time feedback about the current position of the needle (as a needle line)
- Arbitrary control of CT images while observing them from different viewpoints (selection of any oblique slice)
- A volumetric view containing the dataset (as a block form), the planned needle trajectory, as well as real-time feedback of the tracked needle and the clipping plane (which defines the oblique plane). This view was designed for spatial orientation, not for visualizing 3D organs.

Before the test, we had some *assumptions* regarding the two alternative ways of assessing critical tissues and trajectories:
- The needle-dot view is useful to check all oblique slices perpendicular to the needle in order to see where the needle intersects the body and to decide whether it is a good trajectory or not. The idea is to look from the point of view of the needle, from the skin to the tip of the needle inside the body (or the other way around), slice by slice, having a view on the needle trajectory and its close surroundings.
- The needle-line view clearly shows the route of the needle having the entire needle trajectory in view that can be inspected from different angles.

The *goal* was to know how the novel interactions are used by physicians and what kind of information they provide and add to the current situation.

The *reactions* of the physicians were ambiguous. Although the idea of having better ways to evaluate the needle trajectory was appreciated, the oblique views were not used or not trusted, because:
- It conflicts with the cognitive strategies of the radiologist: they learn to look at images which are orthogonal to the body. In general, the axial view is enough to build a 3D mental model, and other orthogonal views are used to better localize structures.
- In the oblique slices structures are distorted (as compared to orthogonal slices which are the reference images for physicians), and makes interpretation (identifying contours for organ localization, shape understanding and estimating distances) and spatial orientation difficult.

As a positive mental model related example, it can be mentioned that the use of the tracked needle was highly appreciated. It was used intuitively, and its movement was immediately understood in relation to the dataset (a foam phantom was used to represent the human body). Reportedly, this kind of navigation resembled needle navigation in the real clinical situation. It was also advised to use as a training tool to learn spatial orientation.
Interestingly, the needle-dot view was useful for adjusting the needle line to the planned trajectory. As it was said, it is similar to another procedure in which the X-ray beam is set orthogonal to the needle. This is an example when user-system interaction meets user experiences.
After the test, we wanted to know *what the reasons* are for the difficulty of interpreting oblique views.

- From physicians, we learned that they conflict with the mental model of radiologists.
- According to vision science literature [6], selecting an oblique slice is not an obvious task and cannot be imagined as a cutting operation. It is probably done through a set of mental rotations. Unfortunately, mental rotations have not been studied in this context.

Findings of vision science led to a *new assumption*: interpretation is easier when an orthogonal slice is rotated to an oblique slice. We also learned that radiologists work with spatial references (e.g. they always use previous needle insertion attempts for new trials (left, right, 1 cm further, etc.)). Another possible solution could be a well-designed spatial reference system or spatial reference links, which improve interpretation of oblique slices.
Our findings were *validated by physicians* through interviews who confirmed the difficulty of oblique slice interpretation and also confirmed the need of oblique slices by giving clinical examples. Actually, some doctors develop their own strategies to be able to work with oblique slices, while others use their old strategies.

5 Discussion

5.1 5.1 Prototype recommendations

Development started on an experimental low-cost research platform that facilitate requirements analysis, and exploration, communication and clarification of ideas by enabling fast changes in the software. Besides this, we recommend to take care of three important properties of the prototype: interactivity, flexibility, and fidelity.

Interactivity We experienced that prototypes facilitating the design process of navigational systems of radiology images have to be interactive due to the constantly changing environment that cannot be captured in, for example, a paper prototype. Interactive prototypes enable exploring both physical and cognitive aspects of human-computer interaction while providing a realistic situation [7]. An interactive prototype is necessary because of the complexity of interaction. This way, the practitioner does not need to image how the proposed system would work, which reduces misunder-

standings and allow the researcher to focus on the studied problems. Other investigations also revealed the necessity of working prototypes in this context [8].

Flexibility Flexibility was an important factor of the experimental prototype. It was beneficial that the number, size and layout of interface elements were easily changeable to represent certain functionalities, a specific part of the treatment or specific user groups.

Fidelity To gain initial insight into the cognitive processes of physicians in early phases of research, it was crucial to provide them with a high-fidelity prototype on certain dimensions [9]. Mental model navigation in the mind is coupled to motor movements of the hand and to image guidance feedback as well. These dimensions therefore had to be high-fidelity. Considering other criteria the prototype could remain low-fidelity, e.g., in the first test a foam phantom was used; that was good enough. Also functionality was intentionally kept on a low-level of fidelity; there was no focus on overall system usability. Functionalities are gradually built into the prototype as our knowledge grows.

5.2 Mental model studies vs. usability testing

Table 1 presents the difference between using the prototype for usability testing and mental model studies in terms of goals, fidelity and expected results.

1 Mental model studies vs. usability testing

Method	Goals	Fidelity	Results
Usability testing (prototype testing in clinic or lab)	• Performance (e.g. time) • Accuracy (e.g. number of mistakes) • Recall (e.g. remembering after a period of time) • Satisfaction (e.g. confidence, stress, enjoyment, visual appeal) • Cognitive limits (e.g. number of menu items)	Mixed-fidelity: fidelity requirements (as always) depend on the research target. E.g., if accuracy is measured, registration has to be perfect. In usability testing there are predefined targets defining which part should have high fidelity and which do not need it, or would even distract.	Errors and improvement possibilities; To some extent learning about user reasoning and behavior
Mental model studies (prototype explorations – combined with ethnography and vision literature study)	Understanding of cognitive processes (e.g. image interpretation)	Mixed-fidelity (for the same reasons). In the current study: • Low fidelity: functionality was restricted • High-fidelity: visualizations and interactions resembled the clinical situation	Models of radiology thinking: • models of radiology image interpretation • models of 3D radiology navigation

6 Conclusion and future work

We have proposed to study mental models of physicians to be able to design better user interfaces for novel technological solutions. Unfortunately, there is little knowledge about modeling of radiology thinking in literature. From our prototype studies it was learned that mental models of engineers may differ from mental models of physicians, which can lead to communication problems and to ineffective user interfaces of new products. Although an example was presented from the field of interventional radiology, the problem is also valid for other fields of radiology image interpretation and navigation, such as radiotherapy. Using low-cost, interactive and flexible prototypes from the very early phases of development is a useful method for studying mental models of physicians, as well as to resolve communication and design problems. Next steps in our research will be: next iteration mental model research, requirement analysis, idea finding usability testing and clinical evaluation.

Acknowledgements

We would like to thank radiologists of Erasmus Medical Center, Netherlands.

References

1. Wyawahare M.V., Patil P.M., Abhyankar H.K.: Image registration techniques: An overview. Int J of Signal Processing, Image Processing and Pattern Recognition 2(3):11-28 (2009)
2. Staggers N., Norcio A.F.: Mental models: Concepts for human-computer interaction research. Int J Man-Machine Studies 38(4):587-605 (1993)
3. Doyle J.K., Ford D.N.: Mental model concepts for system dynamics research. System Dynamics Review 14(1): 3-29 (1998)
4. Varga, E., Freudenthal, A., Pattynama P.M.T.: Manipulation of mental models of anatomy in interventional radiology and its consequences for design of human-computer interaction, Cognition, Technology & Work, DOI: 10.1007/s10111-012-0227-6 (2012)
5. Stüdeli T.: Surgical wayfinding and navigation processes in the human body. Cognitive Processing 10 (Supp. 2):316-318 (2009)
6. Palmer S.E.: Vision science: Photons to phenomenology, Chapter 12, The MIT Press (1999)
7. van den Hoven, E., Frens, A., Aliakseyeu, D., Martens, J.-B., Overbeeke, K., Peters, P.: Design research & tangible interaction, TEI'07: First International Conference on Tangible and Embedded Interaction, pp. 109-115 (2007)
8. Meijs F.J.M., Freudenthal A., van Walsum, T. Cognitive processing research as the starting point for designing image guidance in interventions. In: Cattin P. et al. (eds.), MICCAI Workshop on image guidance and computer assistance for soft-tissue interventions, pp. 46-55, New York: MICCAI, (2008)
9. Lim, Y.-K., Stolterman, E., Tenenberg, J.: The Anatomy of Prototypes: Prototypes as Filters, Prototypes as Manifestations of Design Ideas, ACM Transactions on Computer-Human Interaction 15(2):7 (2008)

Author Index